Title
Plasma Formation in Femtosecond Laser Breakdown of Dense Hydrogen Gas

Author
Latshaw, Alexandra

Publication Date
2019

Peer reviewed|Thesis/dissertation

UNIVERSITY OF CALIFORNIA
Los Angeles

Plasma Formation in Femtosecond Laser Breakdown of Dense Hydrogen Gas

A dissertation submitted in partial satisfaction
of the requirements for the degree
Doctor of Philosophy in Physics

by

Alexandra Lane Latshaw

2019

ABSTRACT OF THE DISSERTATION

Plasma Formation in Femtosecond Laser Breakdown of Dense Hydrogen Gas

by

Alexandra Lane Latshaw
Doctor of Philosophy in Physics
University of California, Los Angeles, 2019
Professor Seth J Putterman, Chair

As energy is injected into matter it eventually reaches the plasma state where electrons are separated from ions. The importance of electrostatic interaction in a plasma is determined by the plasma parameter Γ which is the ratio of electric potential energy to thermal energy. Space plasmas and plasmas created in Tokomaks are dilute and have $\Gamma << 1$. The transport properties of strongly coupled plasmas where $\Gamma > 1$ are not understood and are especially important for understanding instabilities in inertial confinement fusion experiments. Dense plasmas with $\Gamma > 1$ are accessible in table top experiments via sonoluminescence, sparks and laser breakdown of dense gases. In this thesis, plasma is generated in 1-10 bar hydrogen gas using a high power femtosecond laser between pulse widths of 130-320fs. By measuring the plasma via CCD images, spectral and bandpass emission, as well as transmitted laser spectra, a transition from tunneling ionized plasma at low pressure to cascade breakdown at high pressure is observed. Dense tunneling plasma is imaged directly for the first time and shown to have a uniform structure. This plasma is proposed as an ideal candidate for the study of dense plasma hydrodynamics.

The dissertation of Alexandra Lane Latshaw is approved.

Wesley C Campbell

Troy A Carter

Pietro Musumeci

Seth J Putterman, Committee Chair

University of California, Los Angeles

2019

To my mother and brother . . .

"I sat belonely down a tree,

humbled fat and small

A little lady sing to me

I couldn't see at all."

–John Lennon

Table of Contents

List of Figures

List of Tables

Acknowledgements

I would like to thank my mother Kathleen and my brother Russell for their support during the last ten years (and all the years)! It has been a long road. Thank you mom for always taking my call and being there when I was alone.

Thank you to my love Dimitrios Kosmopoulos. I can't wait for our next adventure! And to continue growing together as scientists and people.

Thank you to my friends who have supported and challenged me; Elizabeth Mills, Dr. Tom Neiser, Dr. Marika Csapo, Dana Faiez, Janaki Sheth, Dr. Evelyne Alvarez, Yan Liang, Dr. Emily Martin, Dr. Riju Dasgupta, Rebecca Jolitz, and Sarah Chase.

Thank you to my labmates (or flabmates?) for your insights and hard work; Seth Pree, Rhyan Ghosh, Dr. John Koulakis, Dr. Adam Collins, Alexander Thorton, and Dr. Brian Naranjo. I thank Dr. Alexander Bataller for passing the laser breakdown experiment to me to develop as my own.

I would like to thank Professor Stuart Brown for being a trusted mentor. Thank you also to Professor Smadar Naoz and Professor Dolores Bozovic.

Thank you to Professor Katrin Schenk for your vital support early in my career.

I would like to thank Robert Williams, former Executive Director of Associate Students UCLA (ASUCLA), for encouraging me in business. I would like to thank Dr. Michael Skiles, former President of the GSA, for allowing me to represent UCLA graduate students on the Board of ASUCLA. It was a true privilege.

Thank you to my old friends James Sainz, Hanna Lafranconi, and Barry Martin.

Thank you to Carol Hauck, Karin Savoie, Erin Berndt, Savhannah Rotert, Michelle Sulzbach, Cherise Feser, and Allen Hammerquist for the early years in snowy South Dakota.

Thank you to Professor Benjamin Schwartz and Dr. Erik Farr for assistance with the autocorrelator. This was critical for the experiment.

Thank you to my thesis committee; Professor Wesley Campbell, Professor Troy Carter,

and Professor Pietro Musumeci. Thank you to the UCLA Physics & Astronomy Department and Chair David Saltzberg. Thank you to Dr. Stephanie Krilov and Francoise Queval.

And thank you to my advisor Professor Seth Putterman. Thank you for the opportunity to work with world class equipment and to study a deep topic in physics. It has been the hardest thing I have done in my life! I am grateful for what I have learned from you and proud of what we have accomplished together.

This research was supported by the Air Force Office of Scientific Research (AFOSR).

Curriculum Vitae

2013	B.A. in Physics, University of California, Berkeley.
2013 – Present	Ph.D. student in Physics, University of California, Los Angeles (UCLA).
2013 – 2017	Eugene V. Cota-Robles Fellowship, Graduate Division, UCLA.
2015 – 2017	Local Organizing Committee, Conferences for Undergraduate Women in Physics, UCLA.
2016 – 2018	Board of Directors, Associated Students UCLA.

Publications

[1] Alexander Bataller, Alexandra Latshaw, John Koulakis, and Seth Putterman, "Dynamics of Strongly Coupled Two-Component Plasma via Ultrafast Spectroscopy," (2019), Optics Letters .

CHAPTER 1

Introduction

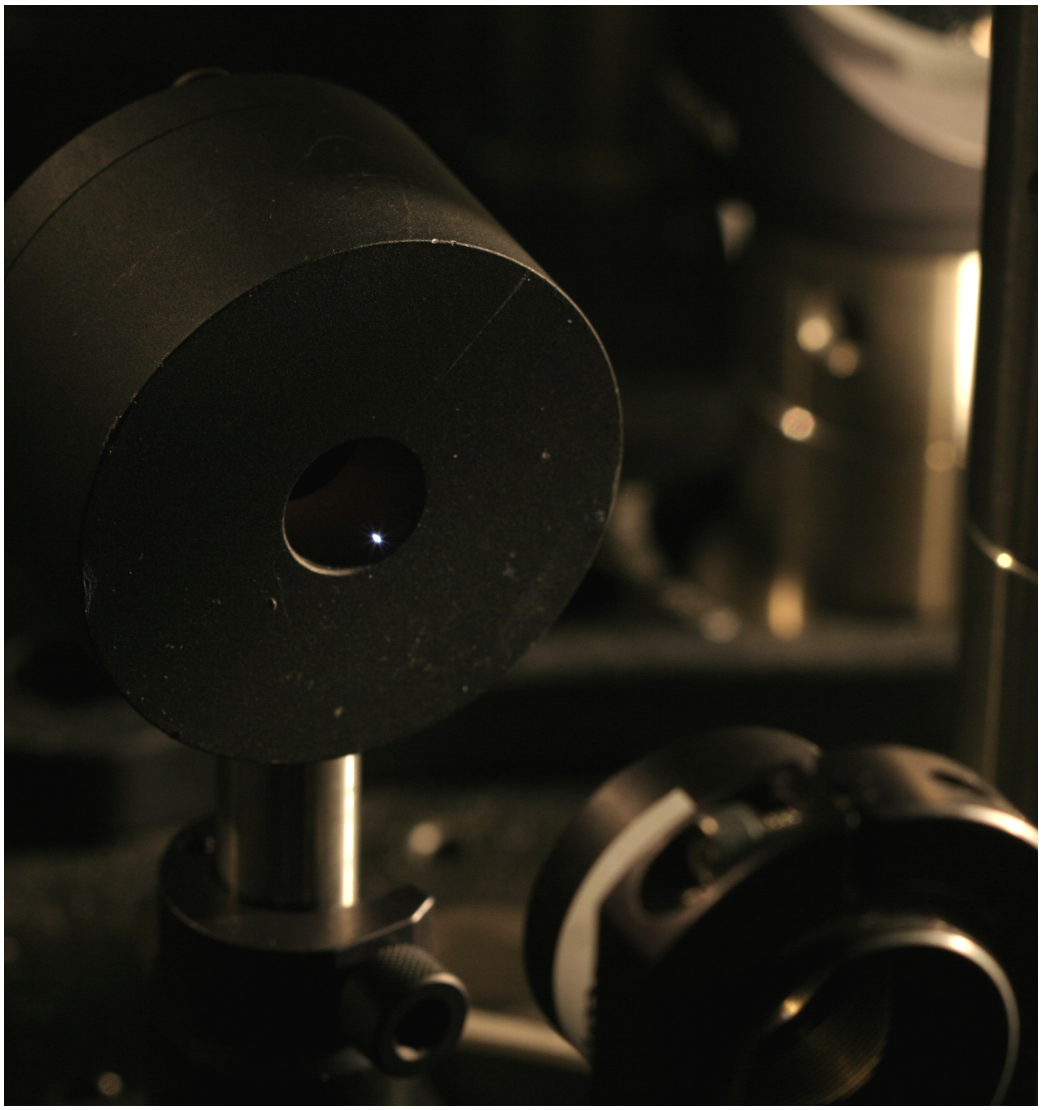

Figure 1.1: Breakdown of air generated by focused femtosecond laser. The lens is in the foreground and the beam block catching the laser is seen behind the plasma.

1.1 Motivation

An understudied but important phase of matter is strongly-coupled plasma (SCP). Such a plasma has formed when the coulomb interaction between charged particles is greater than kT, where k is the Boltzmann constant and T is the temperature of the plasma. The degree to which a plasma is correlated is determined quantitatively by the dimensionless parameter Γ, which is the ratio of coulomb energy to kT so that

$$\Gamma = \frac{(Ze)^2}{akT} \tag{1.1}$$

where the particle spacing is $a = (\frac{3}{4\pi n})^{1/3}$ and n is the charge density. SCPs can be found in the interior of astrophysical objects [1], dusty plasmas [2], ultracold atom and ion trapping [3], inertial confinement fusion (ICF) [4], sonoluminesce [5], and ultrafast laser breakdown [6, 7].

The study of SCPs presents theoretical challenges due to the difficulty of treating particle interactions and collective motion. In contrast to the Navier–Stokes equations, SCP hydrodynamics must be characterized by the nonlocal two-point density correlation $f_2(r_1, r_2)$ (or $g_2(r_1, r_2)$). This means that the probability of finding particle 1 located at r_1 is coupled to the probability of finding particle 2 at r_2. This is a result of the strong Coulomb interaction between them, which is not present in ideal plasmas like that in the earth's ionosphere where $\Gamma << 1$. The exact free-energy density functional for SCPs is not known [8, 9]. This is especially important for interpreting the evolution of fluid instabilities in ICF experiments [10].

One of the most interesting things to occur in SCPs is the appearance of short range order. In a classic paper by Edward Teller [11], the behavior of a "one-component" plasma is described. Teller's model is that ions are immersed in a neutralizing background and are confined to stay within a fixed-volume box. The behavior of the ions in such a one-component plasma is determined by the plasma parameter of the ions. Fig. 1.2 plots the ion-ion spatial correlation function g(x) for various values of Γ_{ions}. For $\Gamma_{ions} < 1$, the ions behave as an ideal gas and are not correlated. For $\Gamma_{ions} > 1$, their motion becomes corre-

lated, and as Γ_{ions} approaches 50 their correlation looks quantitatively like redistribution functions for ordinary fluids. At Γ ~100 the plasma exhibits a fluid-to-solid phase transition! Crystal-structured plasmas have been produced [12] and an example is shown in

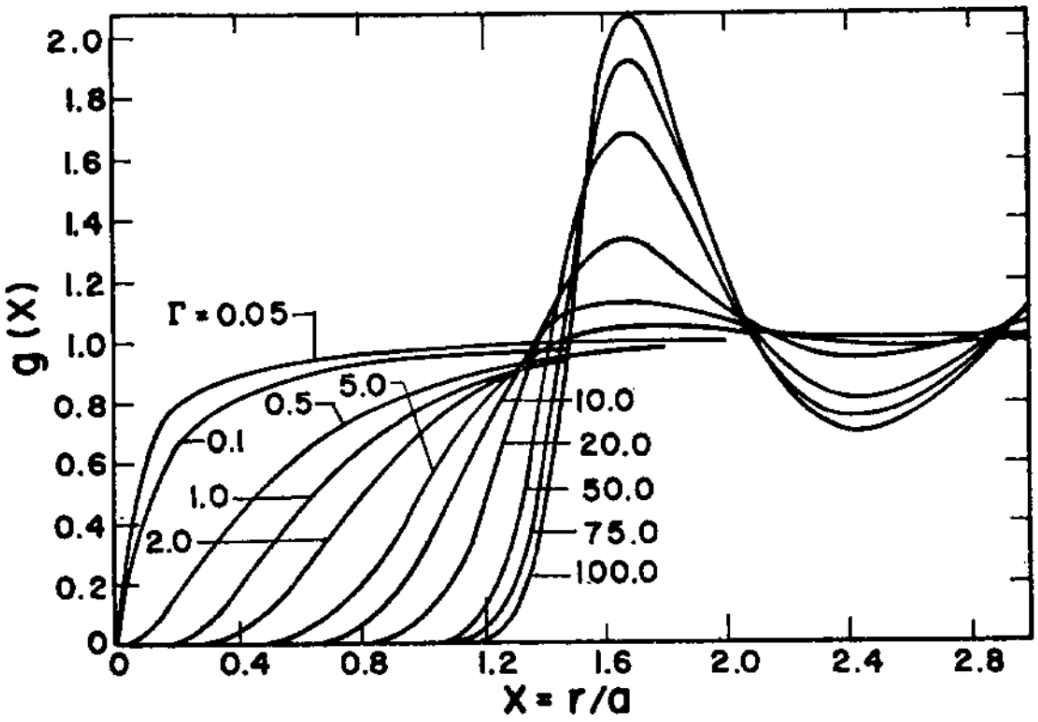

Figure 1.2: Radial distribution functions $g(x)$ for $0.05 \leq \Gamma \leq 100.0$ reproduced from [11]. r=1.6a is the bcc lattice spacing.

Fig. 1.3. However a plasma crystal has not been observed in a "hot" system, i.e., where the ionization potential $\mathcal{E}_{ion}$ is on the order of kT.

SCPs have been found to readily appear in energized dense gases. This includes a) collapsing gas bubbles surrounded by a fluid subjected to a resonant sound field [5], b) electrical discharges in a dense gas [13], and c) femtosecond laser-induced breakdown of a dense gas [7]. These systems generated in the Putterman lab at UCLA are shown in Fig. 1.4. SCPs produced in table top setups provide an opportunity to study coupled plasma dynamics without a large-scale facility. Important behavior to study is the off-equilibrium motion of the plasma to determine transport properties, relaxation processes, and elucidate the

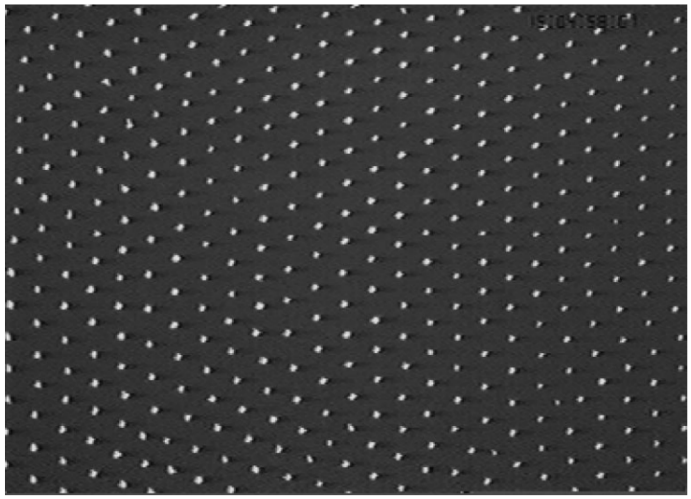

FIG. 8. The CCD image of a horizontal lattice plane of a plasma crystal (top view). The area shown is 6.1×4.2 mm^2 and contains 392 particles of 6.9 μm diam.

Figure 1.3: Plasma crystal observed for $7\mu m$ "dust" particles at room temperature reproduced from [12].

equation of state. However, measuring these dynamics in the lab is difficult because of the small size of the systems (microns) and fast timescales (0.1-30ns) involved.

1.2 Towards Dense Plasma Hydrodynamics

Experiments generating plasmas in dense gas by focusing intense ultrashort pulses in gas have been conducted [6, 7]. In [7] laser breakdown initiated with an ∼300fs laser pulse a neutral gas made of hydrogen at 10atm transforms into a dense plasma with an electron temperature of 30,000K (and an internal pressure >3000atm). This results in a plasma with a coupling parameter value of $\Gamma \sim 0.5$ for the electrons. Part of the goal of this experiment was to access a regime of strong coupling for the ions to observe plasma crystallization.

The Teller model is applicable in the limit that the electrons are very hot and approxi-

(a) (b) (c)

Figure 1.4: Dense, coupled plasmas are made using three different energy focusing mechanisms. a) A low-power acoustic drive generates the plasma inside of an imploding gas bubble in a liquid (sonoluminescence). b) Electric breakdown between needles inside of a high-pressure gas chamber. c) Femtosecond laser-induced breakdown in a high-pressure gas cell. Images were taken in the Seth Putterman laboratory at UCLA.

mate a uniform background. Physically this means that kT is large in comparison to the difference in attraction between the nearest and next-nearest ions; i.e., the electron motion is not perturbed by its nearest ion. This is exactly the situation in femtosecond laser-breakdown, because the incoming laser pulse couples only to electrons. The pulse length is much shorter than the time required for electrons to thermalize with ions, therefore the ions remain at ambient temperature for a short while. The key point is that for laser ionization, the ions are initially at ambient temperature T_{ions} =300K, and Γ_{ions} comes out to be around 70 for 10atm of hydrogen gas. However, the electron–ion equipartition time is only 10–20 ps for the hydrogen plasma and was beyond the temporal resolution of the experiment.

Attempting to access exotic plasma states via laser breakdown is still an ongoing goal. To do this the method of generating breakdown must be a well controlled process. If we wish to study SCPs over a range of coupling strengths the key variables dictating plasma density and temperature must be understood. To open up this field, this thesis examines the

formation process for plasma generated by femtosecond laser pulses in dense hydrogen gas.

1.3 Laser-Generated Plasma

Starting with giant pulse Q-switched lasers, a focused laser beam was found to have sufficient power to break down gases, liquids, and solids into plasma [14]. Laser-induced breakdown requires a threshold laser intensity [15] and a lot of literature surrounds the measurement of this value for given laser frequencies, pulse widths, focusing conditions, and materials. Fig. 1.5 shows one of the landmark measurements of the breakdown threshold from the 1960s. Knowing the threshold value has been important for designing energetic pulsed laser systems, since focusing the beam can generate a plasma which destroys spatial and temporal beam quality or optical components. In some systems breakdown is the desired result, such as in intraocular microsurgery or micromachining where controlled laser breakdown plasma is used as a blade or drill [16].

The threshold for breakdown is dictated by ionization growth mechanisms in the material, which are 1) collision-free photoionization via the laser's electric field (depending on the frequency of light, known as multiphoton ionization or tunneling ionization) and 2) collisional cascade (also known as avalanche or impact ionization) [17]. In cascade breakdown, a free electron in the material provided by impurities or photoionization starts to absorb the field through collisions with other particles (known as inverse Bremsstrahlung absorption). When the electron has sufficient momentum it frees a new electron via collision. The process is repeated resulting in a avalanche buildup of the free charge density.

While laser breakdown can be used as a tool, such as making subwavelength holes in material [18], it can also be used to generate off-equlibrium plasmas with large plasma parameter [6]. Experiments generating nonideal dense plasmas by focusing intense ultrashort pulses in gas have been conducted [6, 7], but the mechanism responsible for breakdown and how this impacts the resulting plasma state has not been explored. Previous experiments have used tightly focused (f/5) 100fs, 620nm pulses in dense gas [19, 20] and

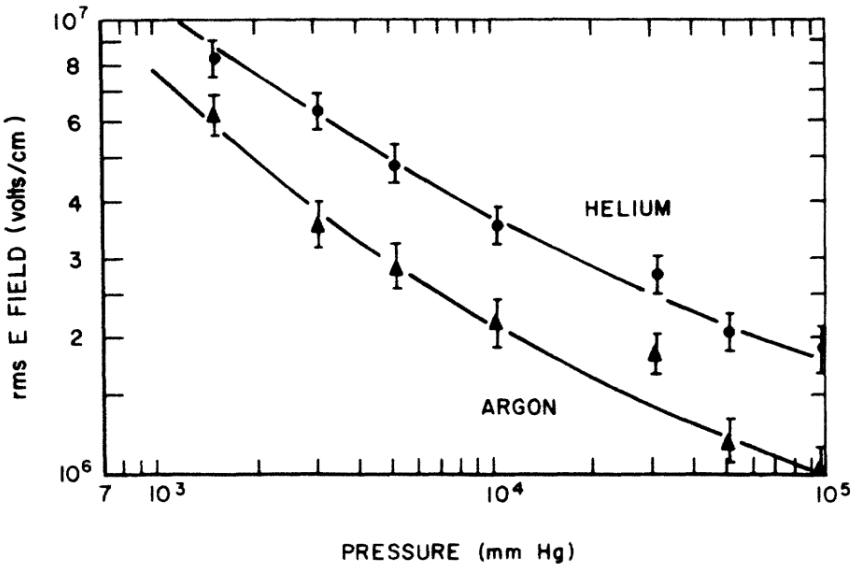

FIG. 2. Breakdown field strength as a function of pressure.

Figure 1.5: Reproduced from [14]. The seminal paper by Meyerand and Haught in 1963 measured the electric field threshold for gas breakdown with a ruby laser at 693nm. The amount of ionization could not be explained by classical microwave breakdown theory and the process of inverse Bremmsstrahlung is proposed.

have investigated the ionization mechanism. However, minimal pulse energies were used (<0.4mJ) and, although breakdown was observed, absorption of the laser pulse was less than 1%. Long filaments of plasma have also been generated in dense gas (i.e., air) by striking a balance between self-focusing and plasma-induced defocusing of the laser beam. In self focusing, the spatial variation in the intensity of the laser causes a higher index of refraction in the center of the beam than in the wings. This causes the beam to focus in on itself, increasing the effect. This can lead to electric fields above the breakdown threshold of the material and generate plasma. Due to the presence of electrons, the plasma has a lower index of refraction than the surrounding gas, which we will derive, and can act as a negative or diverging lens. Self-focusing can be made to balance the plasma defocusing effect, and this has generated filaments of plasma 20 meters long [21]! We will explore the

propagation of light in later chapters to understand these effects in detail. However, the filaments generated are low electron density [21, 22], only around 0.1% ionized. The mechanism responsible for dense gas breakdown and the impact of this on the initial conditions of the plasma, such as temperature and density, has not been explored. This could be very important for controlling the coupling parameter in gas laser-breakdown studies of dense plasma hydrodynamics. In laser ablation experiments cascade is found to be the dominant mechanism in the breakdown of glass down to pulse widths of 100fs [15]. No such experiments exist for dense gas.

Variation of the electron density ρ as a function of time can be expressed as [23]:

$$\frac{\partial \rho}{\partial t} = (\eta - g)\rho + (\frac{\partial \rho}{\partial t})_m \tag{1.2}$$

The first term on the right represents the cascade growth, where the cascade ionization rate η is the probability per unit time that a free electron will have an ionizing collision with a bound electron. The electron loss rate g represents free electron losses due to recombination, trapping and diffusion out of the focal volume of the beam. The second term on the right is the multiphoton ionization contribution to the electron density. To solve (1.2) it is assumed that

$$(\frac{\partial \rho}{\partial t})_m = \eta' \rho_b(t) \tag{1.3}$$

where $\rho_b(t)$ is the density of bound electrons at time t and η' is the multiphoton ionization rate. This is the transition of the electron into a free state accompanied by simultaneous absorption of several quanta [24].

There is a second photo-absorption mechanism which is called tunneling. This is a semi-classical effect where the electron tunnels through the barrier of the atomic potential well. The tunneling time is determined essentially by the mean free time of the electron passing through a barrier of width

$$l = \frac{\mathcal{E}_{ion}}{eE} \tag{1.4}$$

where $\mathcal{E}_{ion}$ is the ionization potential and E is the electric field. The average electron velocity is on the order of $\sqrt{\frac{\mathcal{E}_{ion}}{m_e}}$, where m_e is the electron mass. Up to frequencies on the

order of

$$\omega_t = \frac{eE}{\sqrt{2m_e\mathcal{E}_{ion}}} \tag{1.5}$$

the tunneling effect is determined simply by the instantaneous value of the electric field. At higher frequencies there appears a frequency dependence of the tunneling probability since the electron does not have time to jump through the barrier in one cycle. The tunneling regime corresponds to frequencies of light $\omega < \omega_t$ whereas the multiphoton regime corresponds to $\omega > \omega_t$ [24, 25].

1.4 Dense Laser-Generated Plasma

We seek to form a rate equation which can describe the electron density growth over the duration of a laser pulse on the order of several hundred femtoseconds. Equation (1.2) is used for threshold intensity calculations and diverges at long times. We propose the following model for the electron density $\rho_e(t)$ during laser ionization:

$$\frac{\partial \rho_e(t)}{\partial t} = \eta' \, \rho_n(t) + \eta \, \rho_e(t)(1 - \frac{\rho_e(t)}{\rho_{n_0}}) \tag{1.6}$$

$$\rho_n(t) = \rho_{n_0} - \rho_e(t) \tag{1.7}$$

This includes a contribution from both field-induced tunneling (first term on the right in (1.6)) and impact ionization (second term on the right in (1.6)). η' is the tunneling rate constant and η is the cascade rate constant. This is simply the Kennedy equation (1.2), with tunneling instead of multiphoton photoionization. Additionally, the impact term has been modified to a population-like growth (the logistic function) to limit the maximum electron density to the initial neutral density ρ_{n_0} (disassociated H_2 in this experiment). Losses are neglected. Diffusion of electrons from the focal volume will be a small effect on the femtosecond timescale, as will recombination.

Tunneling is concluded to be the photoionization mechanism in this system. The electric field strengths at the focus of the laser in this experiment are $\sim 10^8 V/cm$ and the frequency of the laser is $\omega \sim 2\times10^{15}\ rad/s$ (800nm light). Taking the electric field measured

in 1 bar breakdown (reported in Chapter 8), the tunneling frequency as defined by (1.5) is $\omega_t \sim 4\times10^{15}\ rad/s$. The relation $\omega < \omega_t$ holds but only by a factor of 2. The more fundamental way of defining the tunneling frequency is the frequency of the electron oscillation in the atom, given by $\frac{\mathcal{E}_{ion}}{\hbar}$. For hydrogen this is on the order $\sim 2 \times 10^{16}\ rad/s$. This puts us well into the tunneling regime. Moreover for 800nm light the energy per photon is only 1.6eV. The ionization of a hydrogen atom via multiphoton absorption would require the "simultaneous" absorption of around 9 photons. This is an unfavorable process. Multiphoton ionization tends to be discussed in the context of laser breakdown via UV lasers where the energy per photon is much greater (∼6eV) [26].

In this thesis plasma is generated in 1-10 bar hydrogen gas using a high power femtosecond laser between pulse widths of 130-320fs. By measuring the plasma through CCD images, spectral and bandpass emission, as well as the transmitted laser spectra, values for the tunneling and cascade rate are found. The rate equation is then solved numerically. The results show a transition from tunneling dominated plasma at low pressure and both pulse widths to cascade dominated plasma as the pressure is increased. The effect on plasma density and temperature is explored from the results of the electron density model. Dense tunneling plasma is imaged directly for the first time and observed to have a uniform structure. This plasma is proposed as an ideal candidate for the study of dense plasma hydrodynamics.

CHAPTER 2

Relevant Plasma Theory

2.1 Definition of the Dielectric Tensor

This derivation follows [27]. An electric field $\mathbf{E}(\mathbf{r}, t)$ varies in space and time. The field induces an electric current density $\mathbf{J}(\mathbf{r}, t)$ in the medium. If the strength of the field is sufficiently weak, then the current can be a response which is linear to the field. This is Ohm's law where

$$\mathbf{J}(\mathbf{r}, t) = \boldsymbol{\sigma}(\boldsymbol{r}, t) \cdot \mathbf{E}(\mathbf{r}, t) \tag{2.1}$$

The conductivity $\boldsymbol{\sigma}$ is a 2nd-rank tensor characteristic of the medium and measures the ratio between the induced current density and the electric field. If the material is isotropic then $\boldsymbol{\sigma} = \sigma\mathbf{I}$, where $\mathbf{I}$ is the 3x3 identity matrix. We analyze the linear response of the system via the macroscopic Maxwell equations:

$$\boldsymbol{\nabla} \times \mathbf{E} + \frac{1}{c}\frac{\partial \mathbf{B}}{\partial t} = 0 \tag{2.2}$$

$$\boldsymbol{\nabla} \times \mathbf{B} - \frac{1}{c}\frac{\partial \mathbf{E}}{\partial t} = \frac{4\pi}{c}(\mathbf{J} + \mathbf{J_{ext}}) \tag{2.3}$$

$$\boldsymbol{\nabla} \cdot \mathbf{E} = 4\pi(\rho + \rho_{ext}) \tag{2.4}$$

$$\boldsymbol{\nabla} \cdot \mathbf{B} = 0 \tag{2.5}$$

The charge density ρ is the induced space-charge field connected with $\mathbf{J}$ through the continuity equation:

$$\frac{\partial \rho}{\partial t} + \boldsymbol{\nabla} \cdot \mathbf{J} = 0 \tag{2.6}$$

$\mathbf{J_{ext}}$ and ρ_{ext} are the current and charge densities from external sources and satisfy a similar continuity equation. Assuming plane-wave states, we Fourier transform (2.3) for an

isotropic medium without external sources to obtain

$$\mathbf{k} \times \mathbf{B} + \frac{\omega}{c}\boldsymbol{\epsilon} \cdot \mathbf{E} = 0 \tag{2.7}$$

$$\boldsymbol{\epsilon}(\omega) = \mathbf{I} - \frac{4\pi}{i\omega}\boldsymbol{\sigma}(\mathbf{k}, \omega) \tag{2.8}$$

The tensor $\boldsymbol{\epsilon}$ is the dielectric tensor of the medium and characterizes the electromagnetic properties of the medium. At this stage we can introduce the electric displacement $\mathbf{D}$ and the magnetic field $\mathbf{H}$ and rewrite (2.7) as

$$\mathbf{k} \times \mathbf{H} + \frac{\omega}{c}\boldsymbol{\epsilon} \cdot \mathbf{D} = 0 \tag{2.9}$$

Comparison between (2.7) and (2.9) suggest $\mathbf{H} = \mathbf{B}$ and $\mathbf{D} = \boldsymbol{\epsilon}\cdot\mathbf{E}$, which is close. If we define a transverse projection tensor with respect to the wave vector k

$$\mathbf{I}_T - \frac{\mathbf{kk}}{k^2} \tag{2.10}$$

then

$$\mathbf{D} = [\mathbf{I} - \frac{4\pi}{i\omega}(\mathbf{I} - \lambda\mathbf{I}_T) \cdot \boldsymbol{\sigma}] \cdot \mathbf{E} \tag{2.11}$$

and

$$\mathbf{H} = \mathbf{B} + \lambda\frac{4\pi}{ick^2}(\mathbf{k} \times \boldsymbol{\sigma}) \cdot \mathbf{E} \tag{2.12}$$

Recalling that $\mathbf{B} = \frac{c}{\omega}\,\mathbf{k} \times \mathbf{E}$, we can see this is another form of the magnetic and electric susceptibility tensors $\boldsymbol{\chi}_m$ and $\boldsymbol{\chi}_e$, where

$$\mathbf{D} = [1 + 4\pi\boldsymbol{\chi}_e]\mathbf{E} \tag{2.13}$$

$$\mathbf{B} = [1 + 4\pi\boldsymbol{\chi}_m]\mathbf{H} \tag{2.14}$$

We will discuss these relations in a later chapter when dealing with the response of non-conducting media to intense electric fields.

2.2 Electromagnetic Waves in Dissipative Media

This derivation follows from [28]. For now let's look at Maxwell's equations written for conducting media (no free charges):

$$\boldsymbol{\nabla} \times \mathbf{E} + \frac{\partial \mathbf{B}}{\partial t} = 0 \tag{2.15}$$

$$\boldsymbol{\nabla} \times \mathbf{H} - \frac{\partial \mathbf{D}}{\partial t} = \mathbf{J} \tag{2.16}$$

$$\boldsymbol{\nabla} \cdot \mathbf{E} = 0 \tag{2.17}$$

$$\boldsymbol{\nabla} \cdot \mathbf{B} = 0 \tag{2.18}$$

For simplicity we assume we are in an isotropic medium, i.e. $\boldsymbol{\sigma} = \sigma \mathbf{I}$, (2.16) becomes:

$$\boldsymbol{\nabla} \times (\frac{\mathbf{B}}{\mu}) = \sigma \mathbf{E} + \epsilon \frac{\partial \mathbf{E}}{\partial t} \tag{2.19}$$

Using the fact that $\mathbf{H} = \frac{\mathbf{B}}{\mu}$ for isotropic magnetic susceptibility. Applying curl ($\boldsymbol{\nabla}\times$) to (2.15) we have

$$\nabla^2 \mathbf{E} = \frac{\partial (\boldsymbol{\nabla} \times \mathbf{B})}{\partial t} \tag{2.20}$$

Rearranging (2.19) and (2.20) we have

$$\nabla^2 \mathbf{E} - \mu\epsilon \frac{\partial^2 \mathbf{E}}{\partial t^2} - \mu\sigma \frac{\partial \mathbf{E}}{\partial t} = 0 \tag{2.21}$$

$$\nabla^2 \mathbf{B} - \mu\epsilon \frac{\partial^2 \mathbf{B}}{\partial t^2} - \mu\sigma \frac{\partial \mathbf{B}}{\partial t} = 0 \tag{2.22}$$

The solutions to (2.21) and (2.22) are

$$\mathbf{E} = \mathbf{E_0} e^{-i(\omega t - \mathbf{k}\cdot\mathbf{r})} \tag{2.23}$$

$$\mathbf{B} = \mathbf{B_0} e^{-i(\omega t - \mathbf{k}\cdot\mathbf{r})} \tag{2.24}$$

Substituting (2.23) and (2.24) into (2.21) and (2.22) yields

$$k^2 = \mu\epsilon\omega^2 + i\mu\sigma\omega \tag{2.25}$$

$$k = k_1 + ik_2 = \sqrt{\mu\epsilon\omega^2 + i\mu\sigma\omega} \tag{2.26}$$

Inserting (2.26) into (2.23)

$$\mathbf{E} = \mathbf{E}_0 e^{-k_2 z} e^{-i(\omega t - k_1 z)} \tag{2.27}$$

We see that the imaginary part of k is responsible for the attenuation of the wave. The skin depth is defined as the distance for the amplitude of the wave to be reduced by a factor of 1/e. The skin depth

$$\delta = \frac{1}{k_2} \tag{2.28}$$

is used as a measure of how far the wave penetrates into the conductor.

2.3 Plasma as a Dielectric

This derivation follows [28, 29]. Consider a bound electron in an external electric field $\mathbf{E}(\mathbf{r}, t)$ where

$$\mathbf{F}_{binding} = -k_{spring}\mathbf{x} = -m_e\omega_0^2\mathbf{x} \tag{2.29}$$

and

$$\mathbf{F}_{damping} = -m_e\gamma\frac{d\mathbf{x}}{dt} \tag{2.30}$$

The equation of motion is

$$m_e[\frac{d^2\mathbf{x}}{dt^2} + \gamma\frac{d\mathbf{x}}{dt} + \omega_0^2\mathbf{x}] = e\mathbf{E}(\mathbf{r}, t) \tag{2.31}$$

If the field varies harmonically in time with frequency ω as $e^{-i\omega t}$ the general solution is $\mathbf{x}(t) = \mathbf{x}_0 e^{-i\omega t}$. Substituting into (2.29) yield

$$\mathbf{x}_0 = -\frac{e/m_e}{\omega_0^2 - \omega^2 - i\omega\gamma} \tag{2.32}$$

The electron has a dipole moment of $\mathbf{p} = e\mathbf{x}(t)$. Now suppose there are n_0 molecules per unit volume, with f_j electrons per atom inside the molecule. Each electron has an oscillation frequency ω_j and damping of γ_j The polarization $\mathbf{P}$ is then

$$\mathbf{P} = \frac{n_0\, e^2}{m_e}\sum_j \frac{f_j}{\omega_0^2 - \omega_j^2 - i\omega\gamma_j} \tag{2.33}$$

and the complex dielectric constant is given by

$$\epsilon(\omega) = 1 + \frac{4\pi n_0\, e^2}{m_e}\sum_j \frac{f_j}{\omega_j^2 - \omega^2 - i\omega\gamma_j} \tag{2.34}$$

In the high frequency limit $\omega >> \omega_j$

$$\epsilon(\omega) = 1 + \frac{4\pi n_0\, e^2}{m_e}\frac{Z}{\omega^2} \tag{2.35}$$

$$\epsilon(\omega) = 1 + \frac{\omega_p^2}{\omega^2} \tag{2.36}$$

where now we have defined the plasma frequency ω_p

$$\omega_p = \sqrt{\frac{4\pi n_e e^2}{m_e}} \tag{2.37}$$

The plasma frequency is the timescale over which neutrality is restored in a plasma after perturbation. The wavenumber k is given by (2.25) without the conductivity term:

$$k^2 = \omega^2\epsilon\mu = \frac{\omega^2\epsilon}{c^2\epsilon_0} \tag{2.38}$$

assuming in the optical region $\mu \sim \mu_0$. This leads us to the important definition for the complex *index of refraction* of a material

$$\tilde{n} = \sqrt{\frac{\epsilon}{\epsilon_0}} \tag{2.39}$$

and so we have

$$k = \tilde{n}\frac{\omega}{c} = \frac{1}{c}\sqrt{\omega^2 - \omega_p^2} \tag{2.40}$$

For $\omega < \omega_p$, k is purely imaginary. There will be no propagation in the medium. As we saw in the previous system the wave will be attenuated by an imaginary wavenumber. The reflectivity is very high in plasmas for light with frequency below the plasma frequency. An example of this from our system is shown in Fig. 2.1.

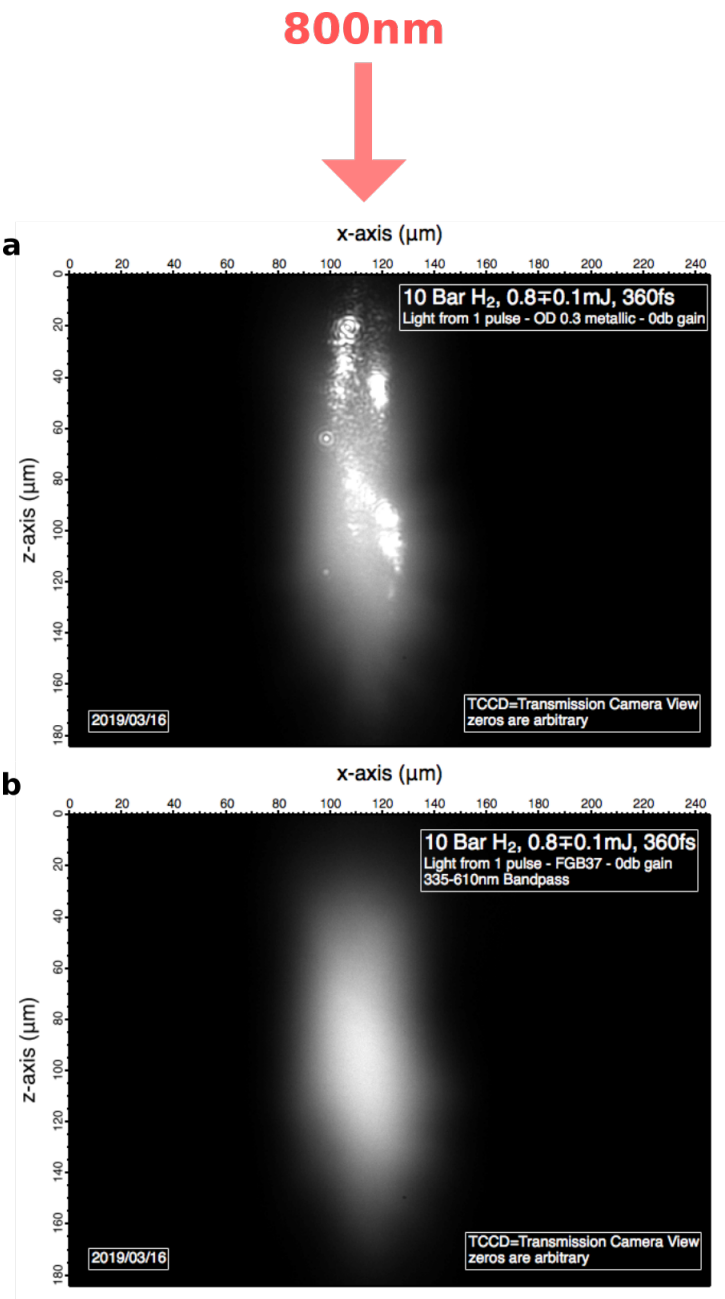

Figure 2.1: CCD image of femtosecond laser generated plasma in 10 bar hydrogen. The camera integrates the total light from 1 plasma viewed through a) an ND filter and b) a 335-610nm bandpass filter. The saturated spots on a) must be scattered light from the 800nm laser. If the plasma is fully ionized here at 10 bar then we are below the plasma frequency by a factor of 2. However, this is close enough to get reflections in a real system.

2.4 Light Emission from Plasma

These derivations follow [30].

2.4.1 Equation of Radiative Transfer

The propagation of light through plasma is affected by the absorption, emission, and scattering properties of that plasma. We describe the exponential attenuation of an electromagnetic wave in a plasma by the linear absorption coefficient a_ω. For a wave traveling in the z direction through a plasma, we may write

$$\frac{d\mathcal{J}_\omega}{dz} = -a_\omega \mathcal{J}_\omega \tag{2.41}$$

where $\mathcal{J}_\omega$ is the spectral intensity ($Wsr^{-1}Hz^{-1}$) of the wave. The absorption coefficient is related to the wave vector of the electromagnetic wave by

$$a_\omega = -2\mathbf{Im}(k) \tag{2.42}$$

Recall that the imaginary part of the wave vector can be related to the conductivity of a medium. If the conductivity is zero, there is no absorption. The fractional loss of intensity of the light on passing between z_1 and z_2 is known as the optical thickness or optical depth $\mathcal{D}_\omega$ and given by

$$\mathcal{D}_\omega = \int_{z_1}^{z_2} a_\omega dz \tag{2.43}$$

We now define the radiation power emitted per unit solid angle per unit frequency from a unit volume of plasma, as j_ω. We can define a source function $\mathcal{S}$

$$\mathcal{S}_\omega = \frac{1}{n^2}\frac{j_\omega}{a_\omega} \tag{2.44}$$

where n is the real part of the refractive index.

$$n = \frac{c}{\omega}\mathbf{Re}(k) \tag{2.45}$$

The change in intensity of light passing through an emitting and absorbing layer of plasma of thickness dz is therefore given by

$$n^2 d(\frac{\mathcal{J}_\omega}{n^2}) = (-\mathcal{J}_\omega a_\omega + j_\omega)dz \tag{2.46}$$

which can be written in terms of the source function and optical depth as

$$\frac{d}{d\mathcal{D}_\omega}(\frac{\mathcal{J}_\omega}{n^2}) = -\frac{\mathcal{J}_\omega}{n^2} + \mathcal{S}_\omega \tag{2.47}$$

This is the *equation of radiative transfer*. If we wish to obtain an expression for the brightness of a slab of plasma, we integrate this equation with the proper source term along the optical depth. A steady state solution may be written:

$$\mathcal{J}_\omega = \int_0^{\mathcal{D}} \mathcal{S}_\omega \, e^{-\mathcal{D}_\omega} d\mathcal{D}_\omega \tag{2.48}$$

2.4.2 Local Thermodynamic Equilibrium

If the plasma is in local thermodynamic equilibrium (LTE), (2.48) can be easily solved. In our case, LTE means that the electrons have a well defined thermal velocity distribution, but not are necessarily in equilibrium with the ions in massive particles (ions) in the system. Global thermodynamic equilibrium would require homogeneous intensive properties throughout the system, such as temperature and pressure. If the electrons have a Maxwellian distribution with temperature T_e, it can be shown that

$$a_\omega = \frac{j_\omega}{\mathcal{J}_{\omega B}} \tag{2.49}$$

where $\mathcal{J}_{\omega B}$ is the black body spectral intensity at temperature T_e. This is Kirchoff's Law. In this case the source function for the plasma is

$$\mathcal{S}_\omega = \frac{\mathcal{J}_{\omega B}}{n^2} \tag{2.50}$$

If the electron temperature is uniform, the source function is independent of the optical depth $\mathcal{D}_\omega$ and (2.48) becomes

$$\mathcal{J}_\omega = \mathcal{J}_{\omega B}[1 - e^{-\mathcal{D}_{\omega_{tot}}}] \tag{2.51}$$

where $\mathcal{D}_{\omega_{tot}}$ is the total optical depth of the plasma. We can see that if $\mathcal{D}_{\omega_{tot}} >> 1$ then the plasma emits like a black body at frequency ω! If $\mathcal{D}_{\omega_{tot}} << 1$ then $\mathcal{J}_\omega = \mathcal{J}_{\omega B}\mathcal{D}_{\omega_{tot}}$. For a plasma of length l which is homogeneous along the line of sight $\mathcal{D}_{\omega_{tot}} = a_\omega l$ and therefore $\mathcal{J}_\omega = j_\omega l$.

The plasma goes from radiating an optically thin spectrum to black body spectrum around ω_{trans} which is determined by the thickness of the plasma. Additionally as we saw from the dielectric response of the plasma, below the plasma frequency the plasma is a good reflector. The plasma also cannot radiate at frequencies lower than this – since the plasma frequency is the natural response of the particles to perturbations. The plasma emission can then be summarized as

1. $\omega < \omega_p$ – little to no transmission/emission
2. $\omega_p < \omega < \omega_{trans}$ – black body
3. $\omega_{trans} < \omega$ – optically thin continuous

Fig. 2.2 shows black body radiation from plasma formed via femtosecond laser in high pressure xenon gas.

2.4.3 Sources of Plasma Radiation

There are various sources of emission in a plasma. We need to determine the dominant sources of radiation in our system to calculate (2.51). To summarize a few main processes responsible for plasma radiation:

2.4.3.1 Bound-Bound Transitions

This is when an atom makes a transition from one bound state to one of lower energy. The energy of the emitted photon is well-defined by the difference of these two states and produces spectral line emission. The profile of the line emission will be Doppler shifted by the velocity of the emitting atom or ion, and can therefore be related to the velocity distribution of the particles and other processes such as collisions. Analysis of spectral lines due to bound-bound transitions is a big part of plasma spectroscopy. Fig. 2.3 shows the H-alpha Balmer line emission from our plasma, which is barely distinguishable from the continuum at early times, making this technique difficult to apply to our system.

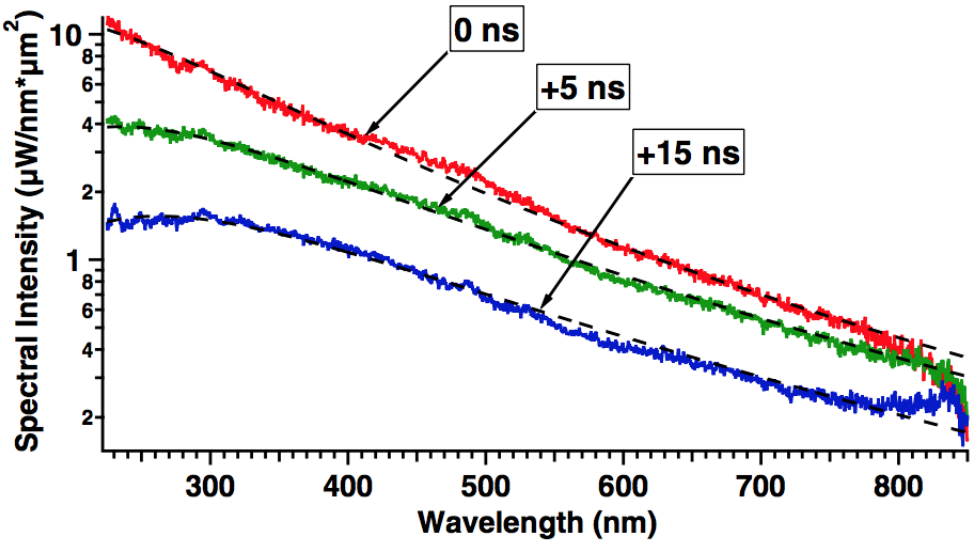

FIG. 3 (color online). Spectral intensity for 5 bar xenon breakdown at different times relative to the plasma formation. Blackbody fits (dashed curves) are plotted for each spectrum with values of $T = 16\,350$, $12\,350$, and $11\,050$ K for $t = 0$, $+5$, and $+15$ ns, respectively.

Figure 2.2: Reproduced from [6].

2.4.3.2 Free-Bound Transitions

This is when a free electron is captured by an ion and makes a transition to a bound state. The excess energy is emitted as a photon and is known as recombination radiation. The emission spectrum is continuous with a sharp low frequency cutoff at the minimum energy to ionize the atom from a bound state. The inverse process is photoionization. There is also three-body recombination which becomes more probable at high density. This is when two electrons collide with an ion: one electron is absorbed by the atom and the other absorbs the excess energy.

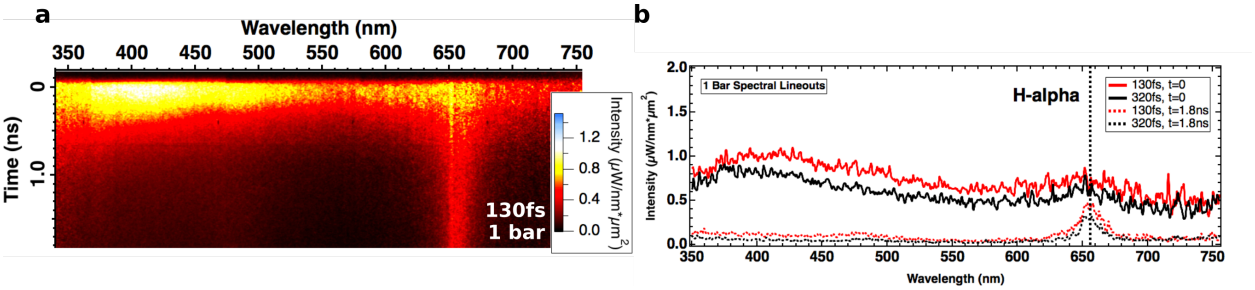

Figure 2.3: a) shows the streak spectrum from plasma generated in 1 bar hydrogen via 130fs laser pulse. b) shows the t=0 lineouts from the streak image in a) and additionally that from 320fs breakdown in 1 bar. The t=0 lineouts show the Balmer line slightly above the continuum. Because of this the line emission would be very difficult to analyze for information about the plasma such as temperature. The spectral line doesn't become well defined until much later, as shown in the t=1.8ns lineouts.

2.4.3.3 Free-Free Transitions

Free-free transitions are when a free electron collides with a particle and transitions to a lower energy free state by emitting a photon. This is the famous Bremsstrahlung emission. The spectrum is continuous and due mostly to electron-ion collisions. Electron-electron collisions do not radiate until they reach relativistic energies. For hydrogenic plasmas of electron temperature around 10eV electron-ion Bremsstrahlung is the dominant radiation mechanism [30], since the plasma is hot enough for most of the neutrals to be ionized. Interactions between electrons and neutral atoms also have much shorter range than the Coulomb interaction, so electron-neutral Bremsstrahlung will be a weak contributor to the emission. The reverse of this process is very important for laser heating of plasma, and fueling collisional avalanche breakdown, and is known as inverse-Bremsstrahlung. This is when a free electron absorbs a photon as it moves to a more energetic free state while in the field of a ion.

2.4.4 Electron-Ion Bremsstrahlung Radiation

Since previous measurements in our system [7] have placed the electron temperature on the order of a few eV with the gas nearly 50% ionized, we will look at electron-ion Bremsstrahlung emission and absorption for modeling plasma radiation. The spectral emission coefficient j_ω is given by

$$j_\omega(T_e) = \frac{4}{3\pi}(\frac{2\pi}{3})^{\frac{1}{2}}(\frac{e^2}{4\pi\epsilon_0 c})^3 \frac{n_e n_i Z^2}{m_e^{\frac{3}{2}}(k_B T_e)^{\frac{1}{2}}}\, n\, g_c(\omega, T_e)\, e^{-\frac{\hbar\omega}{k_B T_e}} \tag{2.52}$$

where $g_c(\omega, T_e)$ is the average Gaunt factor. This term depends upon the Coulomb logarithm and takes some thought to apply in the dense plasma regime [6]. The absorption coefficient a_ω is given by

$$a_\omega = \frac{n_e n_i Z^2 e^6 [1 - e^{-\frac{\hbar\omega}{k_B T_e}}]}{n 6\pi\epsilon_0^3 c\hbar\omega^3 m_e^2}(\frac{m_e}{2\pi k_B T_e})^{\frac{1}{2}}\frac{\pi}{\sqrt{3}} g_c \tag{2.53}$$

The frequency where the plasma of thickness l switches from optically thin Bremmstrahlung to black body radiation is where $a_\omega l \sim 1$. This can be found from (2.53) in the limit of low frequency and high temperature $\hbar\omega << k_B T_e$ where

$$a_\omega \approx \frac{n_e n_i Z^2 e^6}{n 6\pi\epsilon_0^3 c\omega^2}(\frac{1}{2\pi})^{\frac{1}{2}}(\frac{1}{m_e k_B T_e})^{\frac{3}{2}}\frac{\pi}{\sqrt{3}} g_c \tag{2.54}$$

We can directly solve for ω_{trans} by setting $a_\omega l = 1$. Numerically,

$$\frac{\omega_{trans}^2}{\omega_p^2} = 1.75 \times 10^{-16}\frac{n_e Z g_c\, l}{T_e^{\frac{3}{2}}} \tag{2.55}$$

CHAPTER 3

Anatomy of a Femtosecond Laser

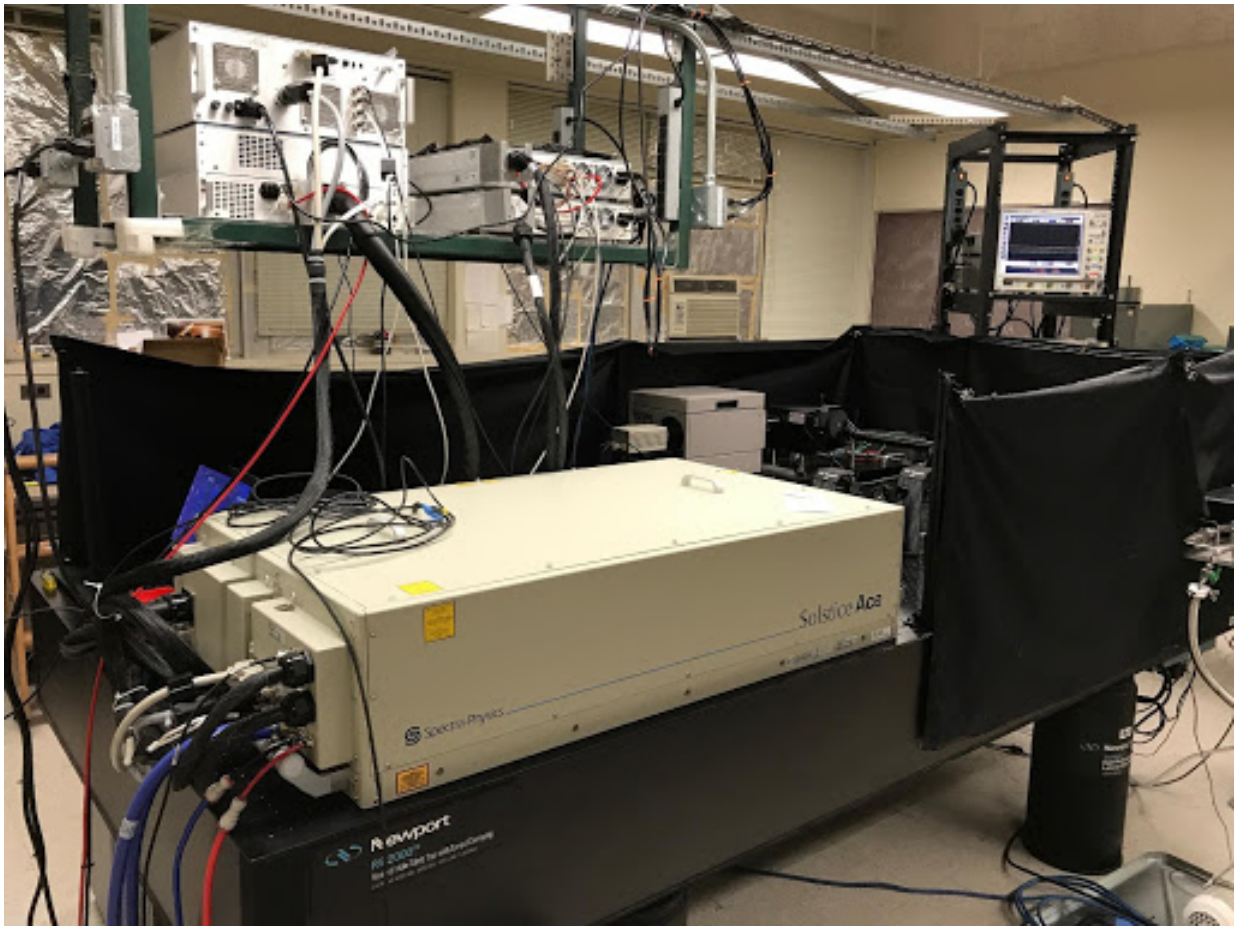

Figure 3.1: Solstice Ace femtosecond laser on the optical table in the lab at UCLA.

We are using a one-box femtosecond amplifier system by Spectra-Physics called the Solstice Ace. Fig. 3.1 is a picture of the laser setup in the lab at UCLA. The key principle of the laser is chirped pulse amplification (CPA), which allows a femtosecond seed pulse of nanojoule energy to be amplified by a factor of a million. Fig. 3.2 shows a layout of the

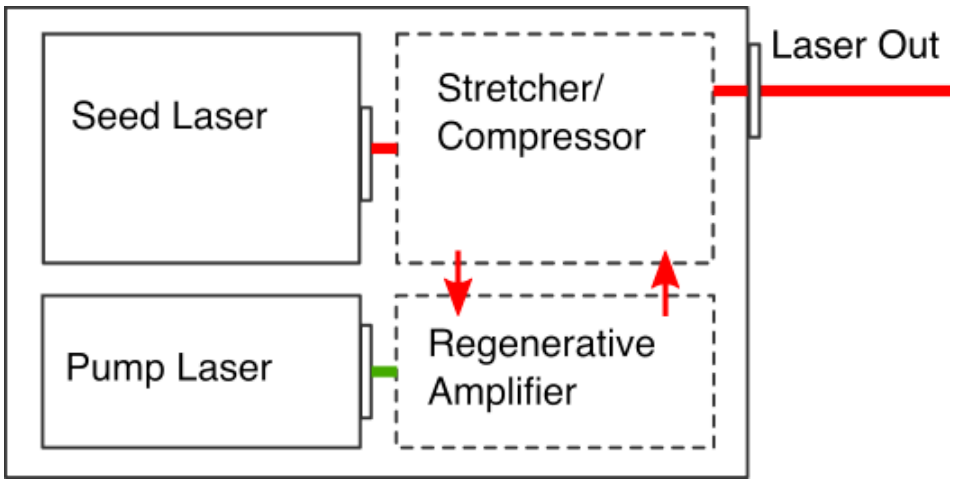

Figure 3.2: Block diagram of Solstice Ace laser.

laser components.

First, a Ti:Sapphire seed laser produces an 80MHz pulse train of 800nm femtosecond pulses via active mode-locking. The pulse is stretched in the time domain by factor of 10^4 by introducing group velocity dispersion (GVD), or "chirp." A seed is selected from the pulse train and sent through a multi-pass Ti:Sapphire amplifier, which is pumped by a 35W, 1kHz laser at 527nm– in the absorption spectrum of Ti:Sapphire. The pulse takes multiple round trips through the cavity until the energy is amplified to millijoule level.

If the seed pulse were to travel through the amplifier without being stretched its high intensity would cause it to self-focus in the crystal. This is due to the nonlinear index of refraction of the crystal. Self-focusing destroys the pulse spectrum and shape and can damage the crystal. After amplification the pulse is compressed back to ultrashort duration achieving nearly terawatt power. The output pulse of the Solstice Ace is ∼6.5mJ and has a duration of 35fs.

The general principle of CPA is illustrated in Fig. 3.3. The technique was developed by Strickland and Mourou in 1985 [31] and they received the Nobel Prize in Physics for their work in 2018. Amplification of short pulses was previously limited by the onset of self-focusing in solid state gain mediums to around 10GW/cm^2. This limitation constrained intense light-matter interaction experiments. CPA is now used to develop almost all of the

world's ultra high power lasers, reaching the pettawatt level! Below the concept of GVD is explained and the technique of CPA in the Solstice Ace is detailed.

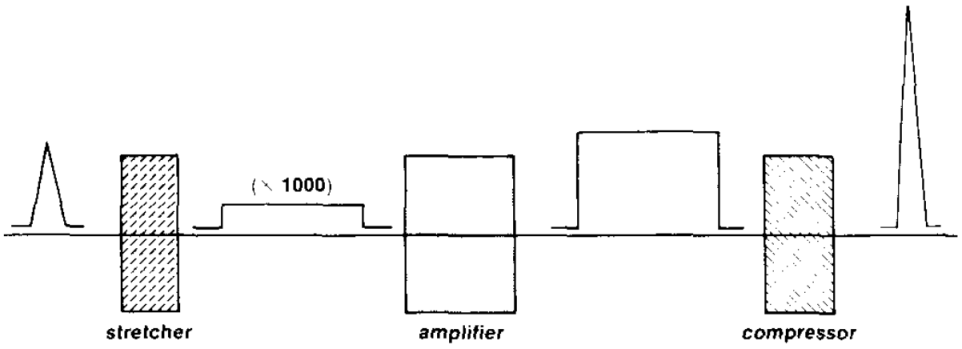

Figure 3.3: The principle of chirped pulse amplification reproduced from [32].

3.1 Group Velocity Dispersion

For this discussion we follow [32]. Consider a laser pulse of the form

$$E(t) = e^{-at^2}\, e^{i(\omega_o t + bt^2)} = e^{-\Gamma t^2}\, e^{i\omega_o t} \tag{3.1}$$

where ω_o is the carrier frequency and $\Gamma \equiv a - ib$ is a complex Gaussian parameter. The intensity $I(t)$ is the usual

$$I(t) = \left|E(t)\right|^2 = e^{-2at^2} \tag{3.2}$$

where the pulse width τ_p is defined as the FWHM

$$\tau_p = \sqrt{\frac{2ln(2)}{a}} \tag{3.3}$$

The total instantaneous phase of the pulse is

$$\phi(t) = \omega_o t + bt^2 \tag{3.4}$$

and the instantaneous frequency is found to be

$$\omega_i \equiv \frac{d\phi(t)}{dt} = \frac{d}{dt}(\omega_o t + bt^2) = \omega_o + 2bt \tag{3.5}$$

The pulse has a linear time varying instantaneous frequency. The relationship between the pulse width τ_p and its bandwidth Δf_p is now:

$$\Delta f_p \tau_p = (\frac{2\,ln(2)}{\pi}) \sqrt{1 + (\frac{b}{a})^2} \tag{3.6}$$

where the first term on the right is the familiar time-bandwidth product. The second term has to do with the time dependent frequency of the light. When a pulse is transform limited it means that each frequency arrives at the same time, and therefore $b = 0$. But you can delay or advance some frequencies with respect to others and this is known as GVD or "chirp." The spectrum of the laser is shown in Fig 3.4.

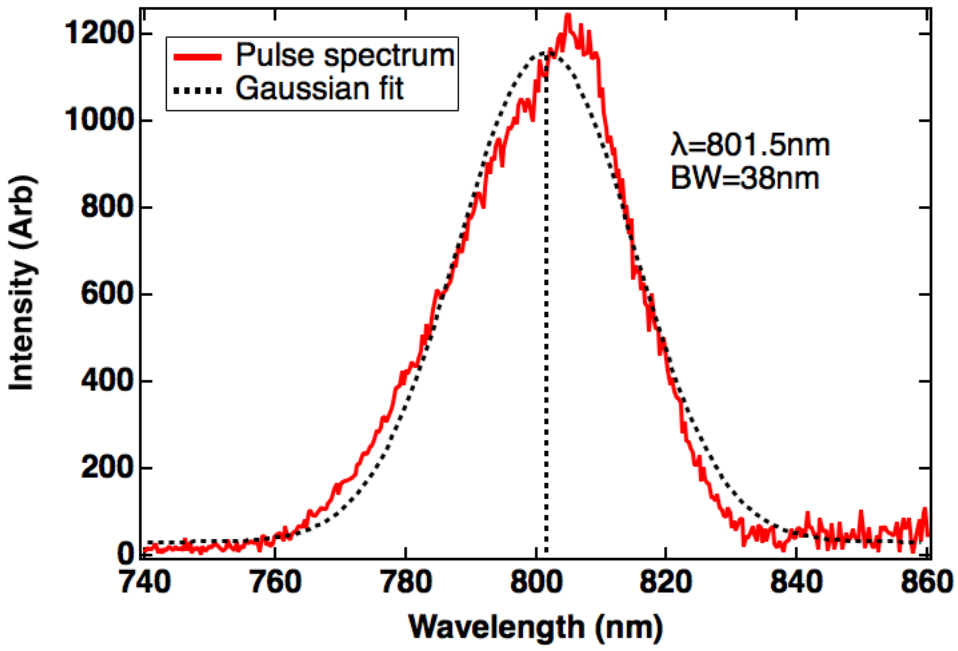

Figure 3.4: Spectrum at the output of the compressor.

GVD is defined by the term

$$\frac{d}{d\omega}(\frac{1}{v_g(\omega)})_{\omega=\omega_o} = -\frac{1}{v_g^2(\omega_o)}\frac{dv_g(\omega)}{d\omega} \tag{3.7}$$

This represents the variation of the group velocity v_g with frequency. The pulse envelope does not simply move at a single group velocity, such as for a narrowband pulse. Recall

$$v_g = (\frac{\partial\omega}{\partial k})_{\omega=\omega_o} \tag{3.8}$$

evaluated at the midband value of $\omega = \omega_o$. Now, different frequency components travel at different group velocities, distorting the pulse envelope and effectively lengthening or compressing the pulse width.

3.2 Nonlinear Optics & Self-Focusing

This discussion follows[33]. In the presence of an electric field, the charges bound in the molecules of a material will tend to line up with the applied field and execute perturbed motions. There is an induced electric polarization $\mathbf{P}$ in the material, or dipole moment per unit volume. If the medium is linear and isotropic we express $\mathbf{P}$ as

$$\mathbf{P} = \chi \epsilon_0 \mathbf{E} \tag{3.9}$$

where χ is called the electric susceptibility of the medium and ϵ_0 is the dielectric permeability of free space. The polarization is linear in the applied electric field $\mathbf{E}$.

The total charge density ρ in the dielectric material can be written:

$$\rho = \rho_b + \rho_f \tag{3.10}$$

The density ρ_b is the bound charge density resulting from the dipole polarization and the free charge density ρ_f is everything else present (an example: ions embedded in the material). Gauss's law now follows

$$\epsilon_0 \nabla \cdot \mathbf{E} = \rho = \rho_b + \rho_f = -\nabla \cdot \mathbf{P} + \rho_f \tag{3.11}$$

where $\mathbf{E}$ is now the total electric field, not just that generated by the polarization. The divergence terms are combined

$$\nabla \cdot (\epsilon_0 \mathbf{E} + \mathbf{P}) = \rho_f \tag{3.12}$$

to form what is called the electric displacement

$$\mathbf{D} \equiv \epsilon_0 \mathbf{E} + \mathbf{P} \tag{3.13}$$

and we can rewrite Gauss's law as

$$\nabla \cdot \mathbf{D} = \rho_f \tag{3.14}$$

The relationship between $\mathbf{D}$ and $\mathbf{E}$ in a *linear medium* is then written

$$\mathbf{D} = \epsilon_0[1 + \chi]\mathbf{E} \tag{3.15}$$

and the complex frequency dependent dielectric constant $\epsilon(\omega)$ is given

$$\epsilon(\omega) \equiv \epsilon_0(1 + \chi) \tag{3.16}$$

where the index of refraction n is related to the dielectric constant by

$$n = \sqrt{\frac{\epsilon}{\epsilon_0}} \tag{3.17}$$

The index determines how light propagates in the medium.

If the electric field is intense, such as in a short pulse laser, it can change the polarization response of the medium. It will no longer be linear in the applied field. We express the polarization as a series expansion in the applied field:

$$\mathbf{P} = \chi^{(1)}\epsilon_0\mathbf{E} + \chi^{(2)}\mathbf{E}^2 + \chi^{(3)}\mathbf{E}^3 \tag{3.18}$$

The electric displacement is then

$$\mathbf{D} = \epsilon_0[1 + \chi^{(1)}]\mathbf{E} + \chi^{(2)}\mathbf{E}^2 + \chi^{(3)}\mathbf{E}^3 \tag{3.19}$$

The second-order term $\chi^{(2)}\mathbf{E}^2$ is responsible for second-harmonic generation, which we will talk about in Chapter 4. Due to the symmetry of this term (the sign of the electric field does not change the polarization), this is only present in materials with non-centrosymmetric arrangement of atoms. These are the nonlinear optical crystals used for harmonic generators.

The third-order term $\chi^{(3)}\mathbf{E}^3$ is present in materials of any crystal structure, liquids and gases. This is the term responsible for self-focusing. If we look at the electric displacement in this case

$$\mathbf{D} = \epsilon_0[1 + \chi^{(1)}]\mathbf{E} + \chi^{(3)}\mathbf{E}^3 = \epsilon_0[1 + \chi^{(1)} + \epsilon_0^{-1}\chi^{(3)}\mathbf{E}^2]\mathbf{E} \tag{3.20}$$

The dielectric constant has become nonlinear in the applied field:

$$\epsilon = \epsilon_1 + \epsilon_2\mathbf{E}^2 \tag{3.21}$$

where ϵ_1 is the linear term (2.12). We can write the index of refraction

$$n \approx n_0 + n_2 \mathbf{E}^2 = n_0 + n_2 I \tag{3.22}$$

where $n_0 = \sqrt{\frac{\epsilon_1}{\epsilon_0}}$ and n_2 is the nonlinear variation which can be measured. We see that the refractive index is modified by the laser intensity I! This is sometimes called the optical Kerr effect with n_2 called the Kerr coefficient.

The consequence of this is that a laser beam, with a spatial profile that has higher intensity in the center than at the wings, creates a higher index in the center of the beam than at the wings. The wings of the beam will focus towards the higher index area. This increases the intensity at the center and the beam continues to focus more and more strongly in a runaway which can create dielectric breakdown (plasma!) in the material. Self-focusing occurs if the laser is sufficiently intense to excite the nonlinear term in the polarization, and this term is stronger than the diffraction spreading for the beam at the same size. It is the reason for chirping ultrashort pulses before amplification. The high intensity of the pulse will cause the beam to self-focus in the gain crystal as it is amplified, destroying the pulse and optics in the process. Fig. 3.5 shows the onset of self-focusing for a 200fs beam propagating in air.

3.3 Stretching & Compressing the Pulse

Chirping, or GVD, can be introduced by sending the laser pulse through dispersive materials, i.e., materials which have a frequency dependent index of refraction. The original generation of ultrahigh peak pulse by CPA used 1.3km of optical fiber [32] to achieve the necessary temporal broadening. The Solstice Ace system uses diffraction gratings. Fig. 3.6 shows a simplified version of this method. The wide bandwidth seed/input pulse is first spread by a diffraction grating. The bluer frequency light is sent on a longer path with the help of a second diffraction grating and routing mirror. The pulse is bounced back and spatially recombined, and sent out of the stretcher having been elongated in time.

The Solstice Ace uses gratings because they can cause much more GVD than other disper-

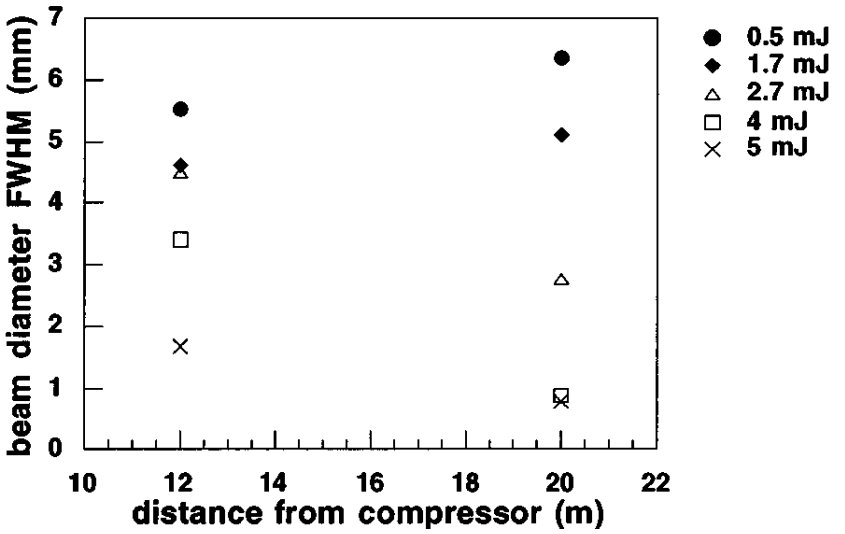

Figure 3.5: Whole beam self-focusing data for a 200fs pulse showing the onset of beam collapse at a power of 10GW, reproduced from [21].

sive optics. The system stretches the seed pulse by a factor of 10^4 in a very small space. The same technique is used in reverse to compress the pulse back to its ultrashort duration after it has been amplified.

3.4 Seed Selection & Regenerative Amplification

After stretching, the amplifier selects a seed pulse for amplification using electro-optical devices called Pockel cells. Pockel cells are made with non-centrosymmetric crystals which experience a change in their refractive index in the presence of a high electric field, due to the second term in (3.22). The electric displacement goes as

$$\mathbf{D} = \epsilon_0[1 + \chi^{(1)} + \epsilon_0^{-1}\chi^{(2)}\mathbf{E}]\,\mathbf{E} \tag{3.23}$$

and so the index change is linear in the applied electric field. For Pockel cells the electric field is applied externally with electrodes. For the Solstice Ace the voltage is 4kV. Pockel cells have two geometries: the field is applied either longitudinally, in the direction of propagation of the laser beam, or transversely, perpendicular to the propagation

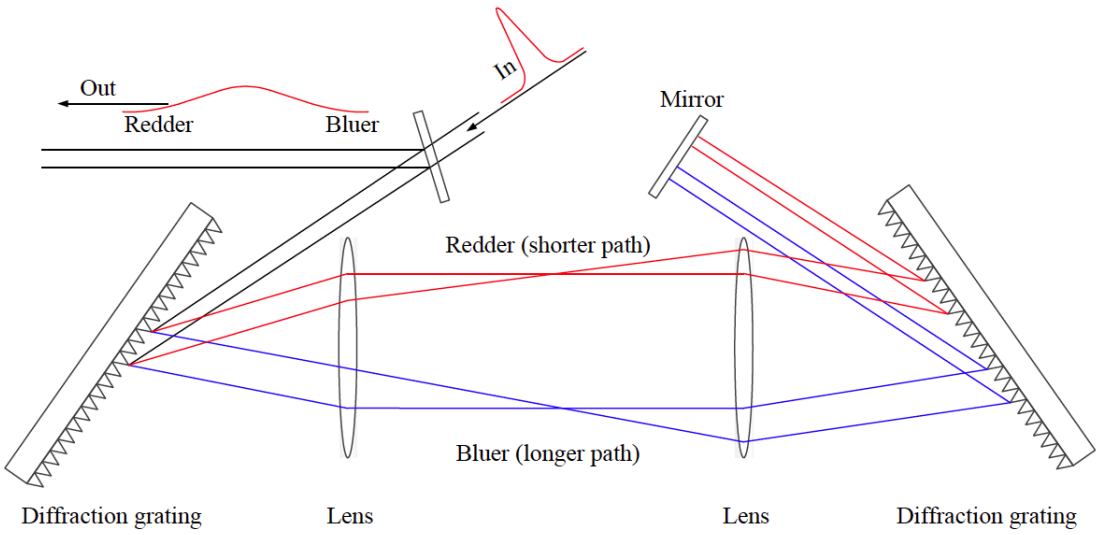

Figure 3.6: Principle of pulse stretching using diffraction gratings reproduced from [34].

of the beam. The index change in the crystal will then be along the axis of the applied electric field. A polarization dependent index of refraction, or birefringence, is experienced by a laser pulse propagating through the cell. Pockel cells are therefore used as voltage-controlled waveplates, which can be switched on and off.

The amplifier cavity of the Solstice Ace is designed so that only vertically polarized light can be trapped for multiple trips through the Ti:Sapphire crystal. The Pockel cells are tuned to act as quarter wave plates so that after two passes through them the laser polarization will be flipped from horizontal to vertical. A series of pockel cells are synchronized to flip the polarization of a seed pulse, first confining it to the cavity to be amplified, and then again flipping the polarization to eject the pulse from the amplifier. When the pockel cells are not energized they have no effect on the laser. Ultrafast pockel cells are used for this kind of pulse selection and have rise times between 3-5ns. This makes it possible to cut the 80MHz seed pulse train down to 1KHz for amplification.

The principle of regenerative amplification leaves the seed pulse in the cavity to extract the gain from the crystal over multiple passes. Fig. 3.7 shows a photodiode measurement from within the cavity. The red trace shows the pulse building up as it makes multiple passes through the crystal– the spikes are separated by the round trip time of the cavity

~9ns. At the proper time a final Pockel cell fires to eject the amplified pulse. The final compressed pulse at the ouput of the Solstice Ace is also seen in Fig. 3.8, measured with a second photodiode and shown in blue.

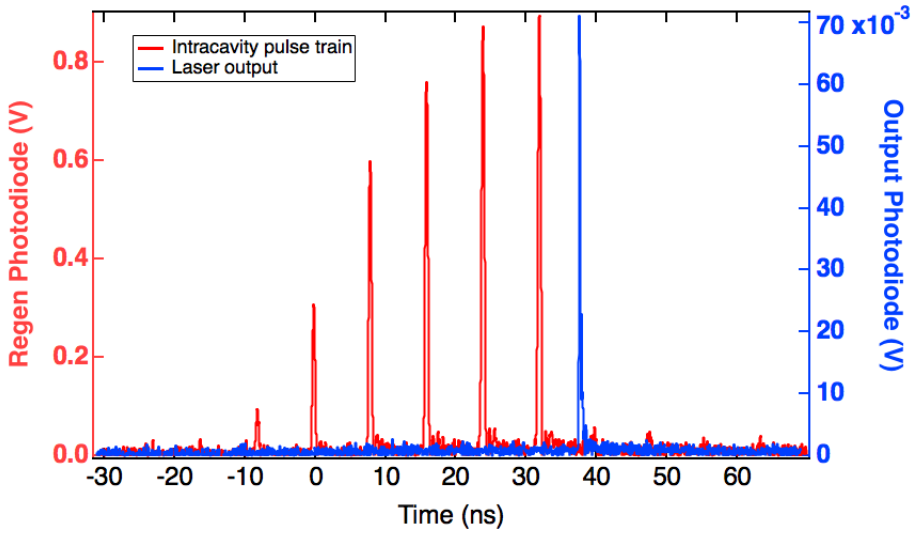

Figure 3.7: The red trace shows a photodiode measurement of the pulse building up in the regenerative amplifier. Note the spacing of $\sim$ 9ns which is the round trip time of the cavity. The final amplified pulse out of the laser is shown in blue. This is used to measure contrast ratio.

Interestingly, if the laser is too well aligned the back-reflection from the pulse can get back to the seed laser from the amplifier. Fig. 3.8 shows this in our system. Strong back-reflection in the seed oscillator causes the system to go unstable and pulse irregularly. The amplifier was then less well-aligned, from an output of >7mJ to 6.5mJ per pulse, for stable operation.

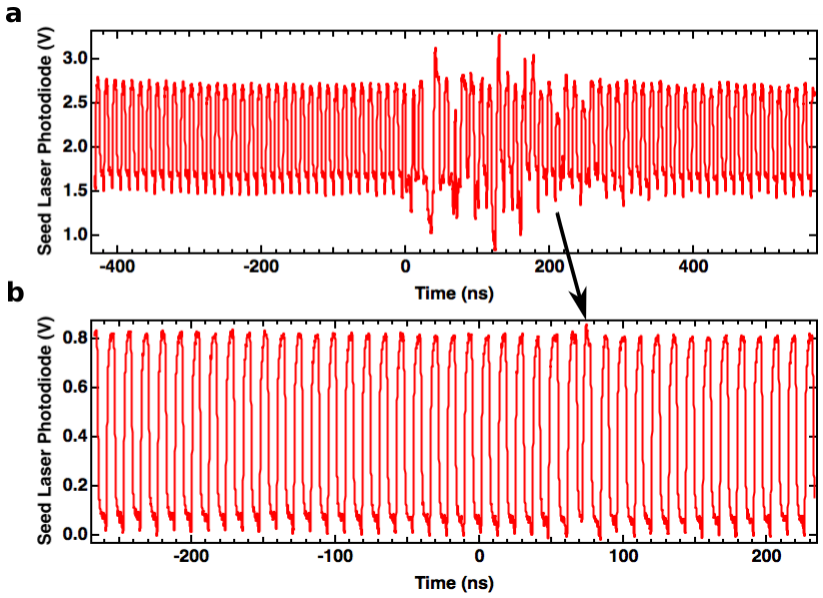

Figure 3.8: The graphs show the 80MHz pulse train of the seed laser. a) shows the pulse train if the Solstice Ace laser is aligned too well. The amplified pulse is reflected back to the oscillator. b) shows the pulse train when the system is slightly less well-aligned.

CHAPTER 4

Chirping the Pulse

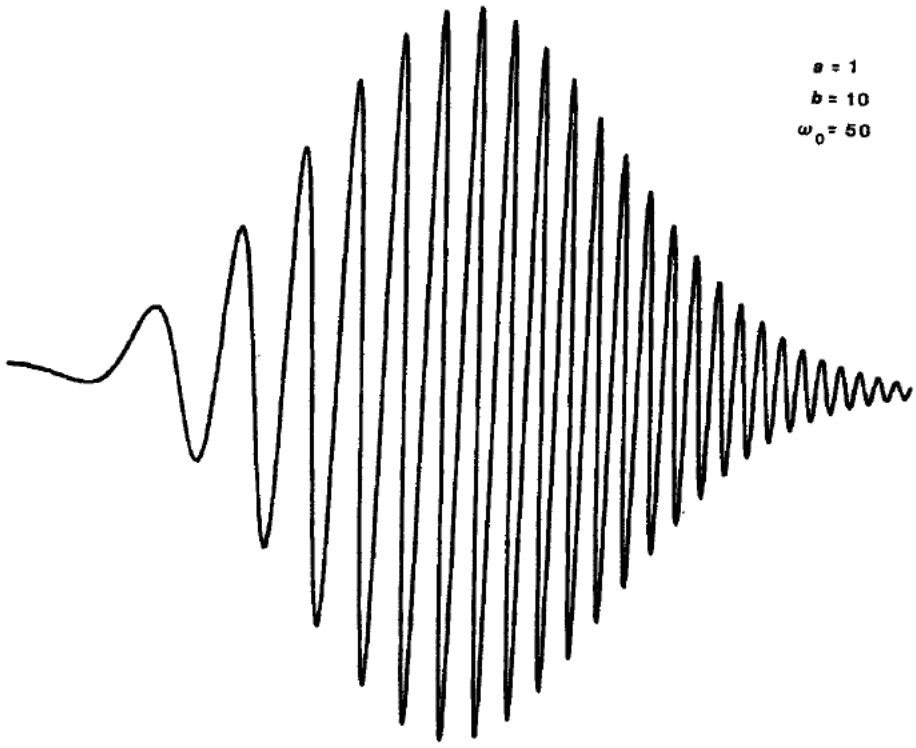

Figure 4.1: A chirped Gaussian pulse reproduced from [33].

The pulse width of the laser can be adjusted by chirping the pulse. Chirping can be accomplished a few ways, such as sending the pulse through a material with a dispersive index of refraction. The Solstice Ace laser uses the method of chirped pulse amplification to amplify femtosecond pulses. The means the pulse duration is increased before it goes into the amplifier, which is done by first spreading the light with a diffraction grating and then sending a portion of the pulse on a longer path. The pulse is then recompressed by

the same method after amplification. The compressor mirror inside the laser amplifier is already adjustable via a motorized stage for fine-tuning the amplifier to its "best compression," i.e., compressing the pulse to the shortest possible duration (∼35fs). The stage position is adjusted via the computer control panel of the laser. We will freely adjust the pulse width of the laser by calibrating this stage position.

We know the pulse width range we wish to work within for reasons which we will detail in later chapters. Our calibration is limited to this. We use a single shot autocorrelator by Positive Light/Spectra Physics designed for measuring femtosecond pulses of Ti:Sapphire wavelengths (∼800nm). The details of the measurement and results are below.

4.1 Measuring Laser Pulse Widths

In order to measure a femtosecond pulse you need something just as short, i.e, a femtosecond pulse. Instruments used to measure laser pulse widths such as streak cameras or photodiodes do not have the resolution for ultrashort pulses. Pulse widths in the femtosecond and picosecond range can be measured with intensity autocorrelation.

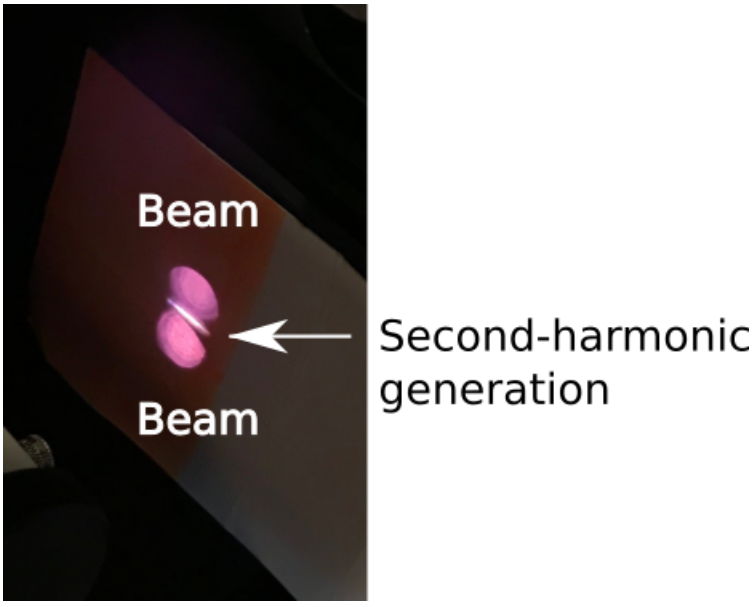

Figure 4.2: Fundamental beams generating SH signal in autocorrelation measurement.

This technique splits a single laser pulse into two equal pulses and then mixes them together at a small angle in a nonlinear crystal to frequency double the light. Fig. 4.2 shows this in our setup. The electric field of the second harmonic (SH) pulse is then the product of the two input pulses:

$$E(2\omega) \propto P^{(2)}(2\omega) = \chi^{(2)} E(\omega)^2 \tag{4.1}$$

where $\chi^{(2)}$ is the nonlinear susceptibility tensor of the crystal. This term arises due to the material's birefringence—in other words having an anisotropic index of refraction. The intensity of the SH generation therefore goes as $I_{2\omega}(t) = \left|E_{2\omega}(t)\right|^2 \propto I_\omega(t) I_\omega(t)$.

If we delay the arrival of one of the input pulses by the amount t_d, and measure the time-integrated intensity of the induced SH as a function of this delay, we have measured the intensity autocorrelation function:

$$A(t_d) = \int_{-\infty}^{+\infty} I_\omega(t) I_\omega(t - t_d) dt \tag{4.2}$$

For a Gaussian pulse the FWHM of $A(t_d)$ is readily found in terms of the FWHM pulse width of the laser:

$$\Delta\tau_A = \sqrt{2}\Delta\tau_p \tag{4.3}$$

The intensity autocorrelation function can be measured in a "multi-shot" configuration where sequential delays are introduced between the pulses and the time integrated SH intensity is recorded. For femtosecond and picosecond pulses however the autocorrelation function can be measured in a single shot. Below this measurement is described in detail.

4.2 Single Shot Autocorrelation

Fig. 4.3 shows the optical design of the single shot autocorrelator (SSA). The pulse enters into a waveplate/polarizer beam splitter which splits the pulse ∼50-50% down two paths, one of which has a delay stage which can change the optical path length of this "probe line." The pulses are mixed non-colinearly in the crystal to generate a SH pulse, which is measured by a CCD array in the forward direction and read out on an oscilloscope. An up

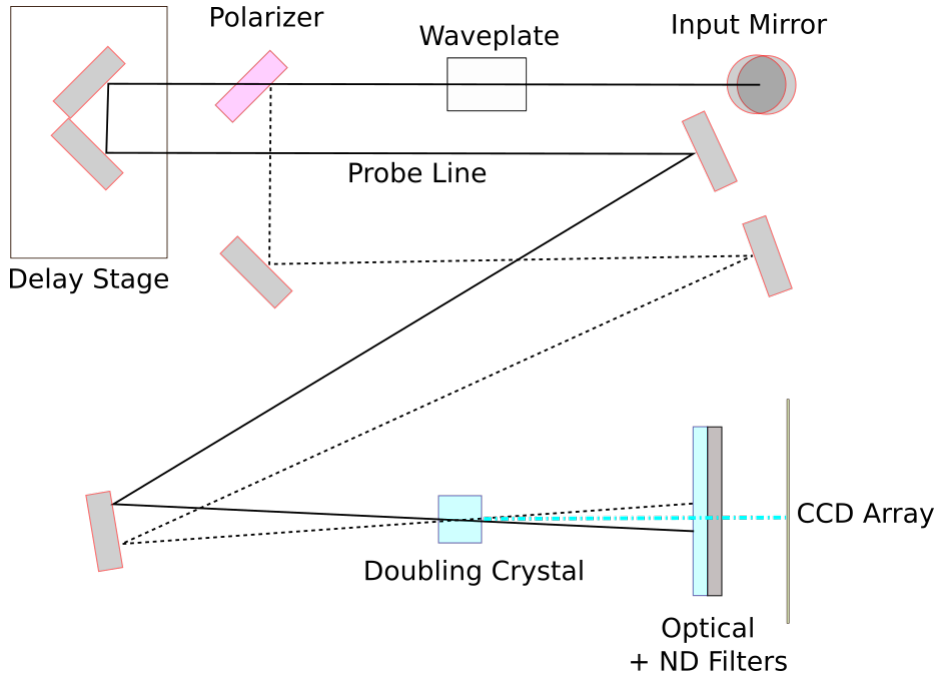

Figure 4.3: SSA optical layout.

close view of the pulse interaction is seen in Fig. 4.4. Here we see the split pulse overlapping in space and time in the crystal to generate the SH beam.

The split pulse can be fully temporally overlapped within the crystal because ultrashort pulses have a short spatial extents (ct_p) compared to their waist size. In contrast nanosecond pulses are a foot long! To probe the full extent of the pulse the delay time must be scanned.

An ultrashort pulse will probe every point of the pulse in a single shot. Each point of overlap generates SH light in the forward direction proportional to the product of the pulse intensities at that point. This generates the spatial extent of the SH beam, which was shown in Fig. 4.2. Because the pulses intersect at an angle the overlap occurs at different times. The spatial extent of the SH beam represents a time delay. The SH signal measured by the CCD is the intensity autocorrelation function which has been generated by a single pulse. We calibrate this measurement to obtain the FWHM of the laser pulse width.

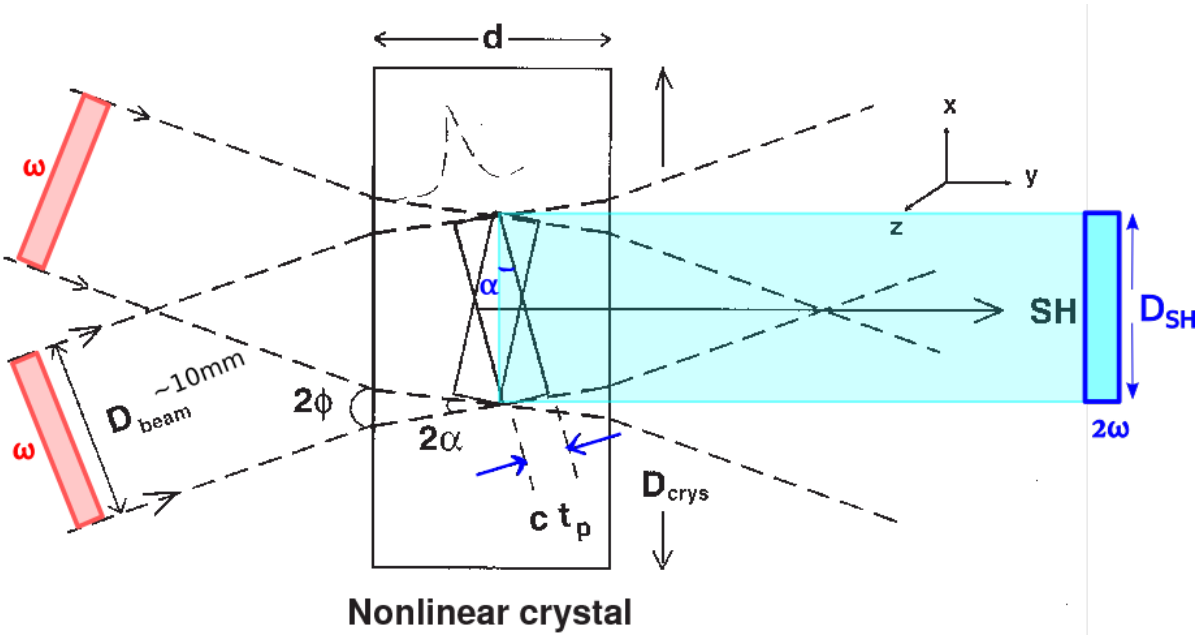

Figure 4.4: Second-harmonic beam produced in nonlinear crystal. Reproduced and modified from [35].

4.3 Pulse Width Calibration

It follows from the diagram in Fig. 4.4 that the FWHM of the SH spatial profile at peak pulse overlap, D_{SH}, is related to the FWHM pulse width τ_p of the input laser by

$$\tau_p = D_{SH}\, sin(\alpha)/c \tag{4.4}$$

where α is the angle at which the two pulses intersect in the crystal. We don't know the angle α. Instead we use the delay stage to increase the path length for probe line. You can show that this will shift the SH peak on CCD array by

$$\Delta z = \frac{c\,\Delta t}{2\, sin(\alpha)} \tag{4.5}$$

where Δt is the time we have delayed the probe pulse, or

$$\Delta t = 2\,(L_2 - L_1)/c \tag{4.6}$$

with L_1 and L_2 being the micrometer positions. We can combine (3.4)-(3.5) to obtain:

$$\tau_p = \frac{D_{SH}}{2}(\frac{\Delta t}{\Delta z}) \tag{4.7}$$

This result is correct for an input pulse of rectangular temporal and spatial distribution. For a Gaussian pulse the relation becomes:

$$\tau_p = \frac{D_{SH}}{\sqrt{2}}\left(\frac{\Delta t}{\Delta z}\right) \tag{4.8}$$

The term $\frac{\Delta t}{\Delta z} = \beta$ is then just a calibration constant between our scope measurement of D_{SH} (in μs) and the pulse duration (in fs). The pulse width relation becomes:

$$\tau_p = \frac{\beta\, D_{SH}}{\sqrt{2}} \tag{4.9}$$

which is just the intensity autocorrelation relation but spatially transformed.

For the best resolution measurement of β the probe pulse delay is scanned to either side of maximum pulse overlap until the SH signal is nearly gone. Fig. 4.5 shows a scan of the probe pulse on one side of peak coincidence. The Δz measurement is then the corresponding amount the peak of the SH signal has moved on the oscilloscope.

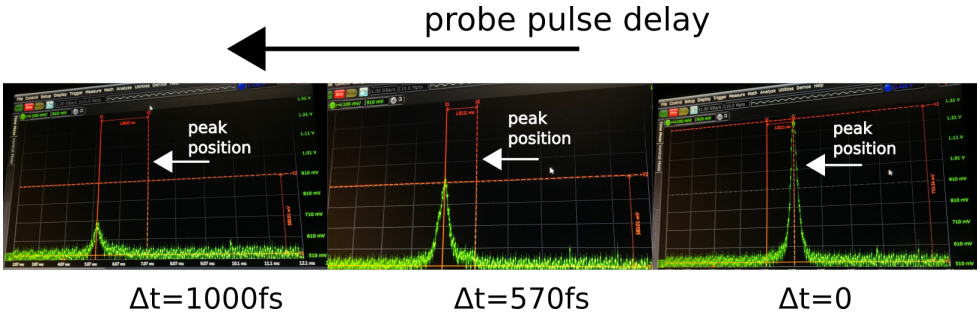

Figure 4.5: Autocorrelation traces show the SH signal moving across the CCD as the probe pulse is delayed from peak pulse overlap. The strength of the SH generation also diminishes.

It was found best to measure β with a minimally chirped pulse so that the peak of SH signal is precise. From several measurements reported in Table 4.1 the calibration constant is determined $\beta = (0.55 \pm 0.02)\frac{fs}{\mu s}$. The pulse widths for several compressor stage positions were then measured. Fig. 4.6 shows the autocorrelation traces for the peak pulse compression resulting in ~50fs pulse as well as longer pulse widths up to ~350fs. The error is determined from the error on the Gaussian fit and the error in the calibration constant. In

the cases of the highly chirped pulses, asymmetry is present in the autocorrelation traces. This is mostly likely due to the intensity distribution of the pulse no longer being smooth. The error on the pulse width is dominated by this asymmetry.

For the measurements, the laser pulse was picked off into the autocorrelator right before the steering mirrors that align into the focusing lens. This gives us a good idea of the pulse width we are using when creating breakdown in the gas, although the lens and glass of the chamber window will have some effect. Fig. 4.7 shows the calibration curve of our system.

Δt (fs)	Δz (μs)	β ($\frac{fs}{\mu s}$)
800	1500	0.533
1633	2900	0.563
1867	3500	0.533
1300	2420	0.537
567	1000	0.567
1000	1833	0.545
1233	2300	0.536
$\beta \pm \delta\beta$		0.55 ± 0.02

Table 4.1: Measurements of calibration constant β for single shot autocorrelation of femtosecond pulses. Δz is measured in microseconds because this is spatial extent of the SHG beam but read out from the CCD array by the oscilloscope (in μs).

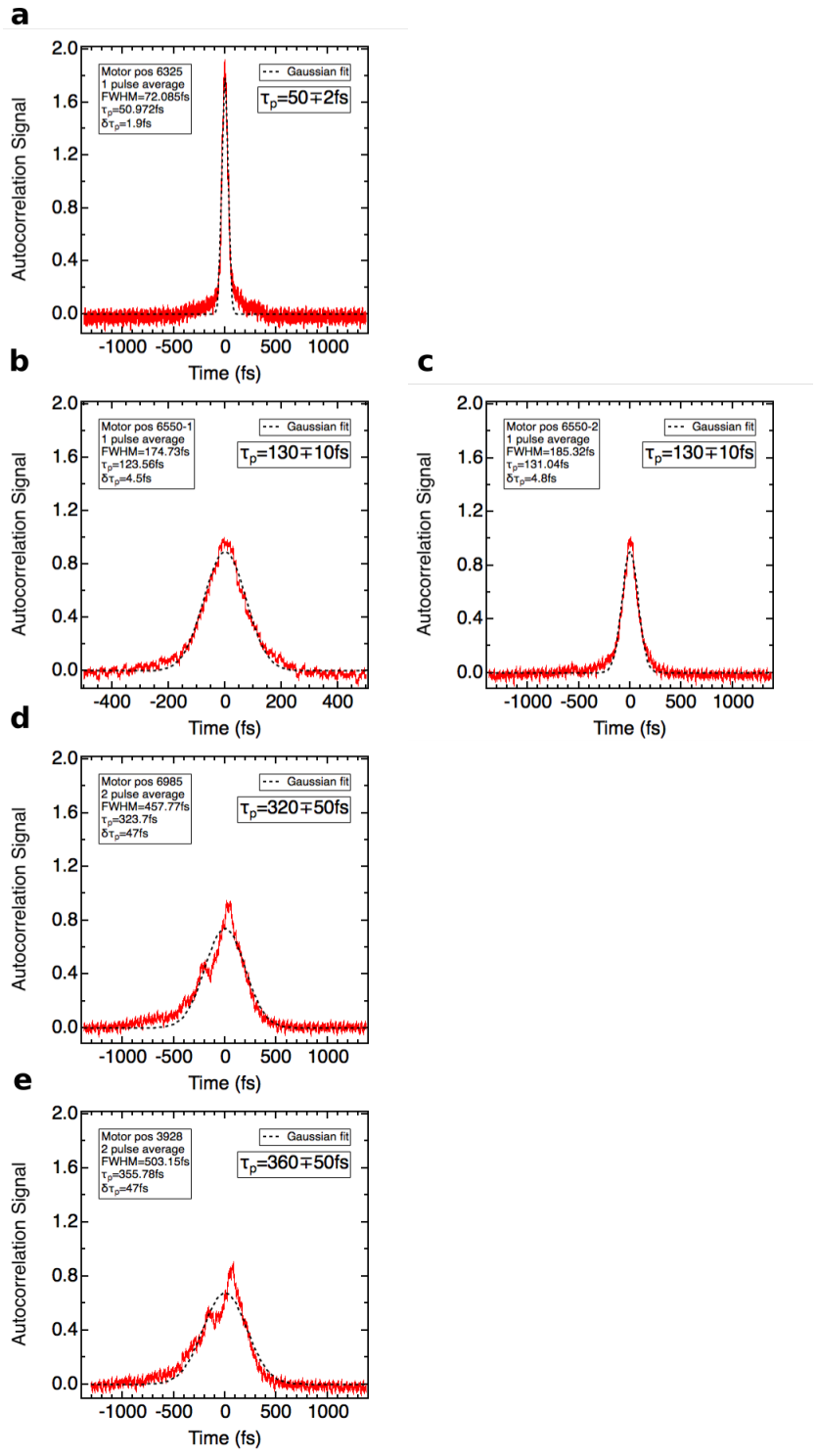

Figure 4.6: Examples of autocorrelation measurements. (a)-(c) show an autocorrelation from a single input pulse. (d)-(e) are the time averaged autocorrelation of 2 input pulses. The fit is computed with the Levenberg-Marquardt least-squares algorithm to minimize the value of Chi-square.

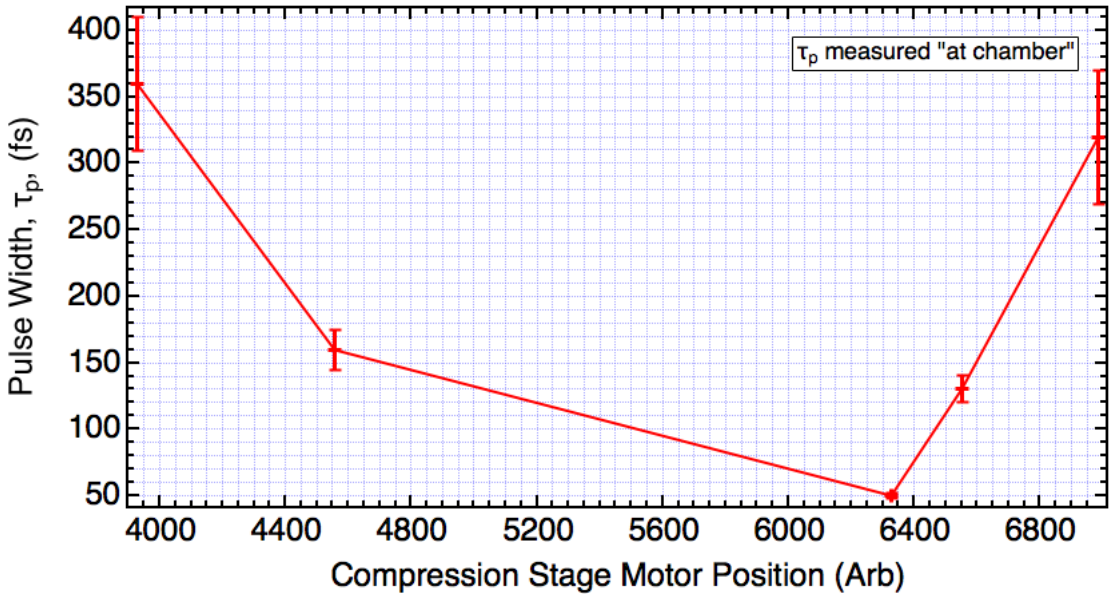

Figure 4.7: Pulse width calibration for our optical setup.

CHAPTER 5

Experimental Setup

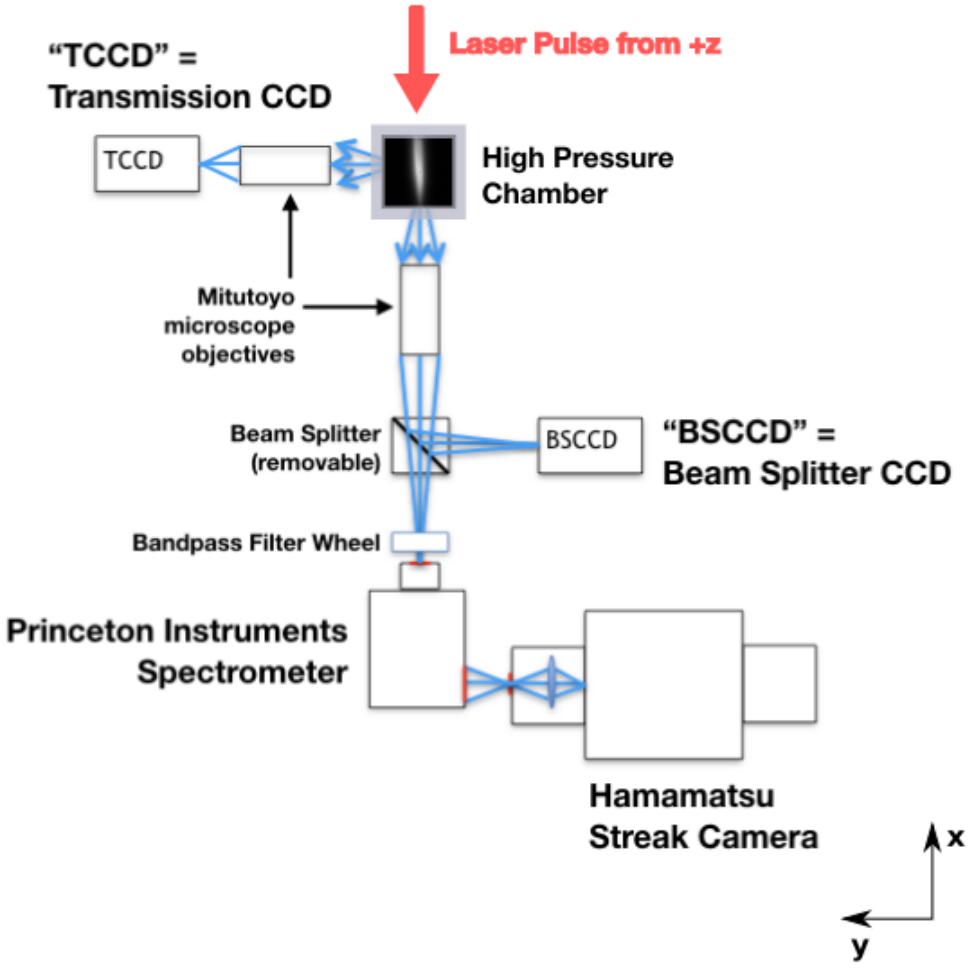

Figure 5.1: Ray diagram following light emission from the plasma through the imaging system.

5.1 Femtosecond Laser

5.1.1 Attenuating the Laser

We are using a Solstice Ace one-box femtosecond amplifier designed by Spectra Physics. The system uses regenerative chirped pulse amplification to amplify a Ti:Sapphire seed pulse and produces a 35fs, 6.5mJ. The pulse has a spectral bandwidth of 38nm around the central wavelength of 801.5nm. We operate at a pulse repetition of 100Hz. We choose to attenuate the laser to ∼1mJ pulse energy. This is where previous experiments have been conducted [7] and also limits spectral and temporal distortion of the pulse when transmitted through optics.

We attenuate the pulse in two stages. First, we pick off the reflection from a dielectric beam splitter (Newport 20Q40BS.2) at the output of the Solstice Ace, which attenuates the pulse to ∼1.2mJ. Using silver mirrors we direct the beam into an achromatic half wave plate (Thorlabs AHWP10M–980) and onto a thin film polarizer. The HWP is rotated to set the reflected power from the TFP, and this beam is directed to the high pressure chamber. The pulse energy is measured by a thermopile energy meter before being focused by the lens, which is about 0.9mJ for our experiments. Fig. 5.2 shows the effect of sending the full 6.5mJ pulse through the HWP with dielectric mirrors, and the corrected pulse that results from attenuating the power and using silver mirrors.

5.1.2 Laser Pulse Width

The pulse width of the laser is set by the compressor mirror position. The compressor follows the amplifier stage within the one-box Solstice Ace setup. It is responsible for re-compressing the pulse which has been temporally broadened before entering the amplifier. This is the principle of chirped pulse amplification which allows for high amplification of ultrashort pulse–above the damage threshold of solid state gain mediums. For this thesis, we adjust the compression mirror to set the pulse width to a minimum of 130fs. Shorter pulse widths result in spectral distortion of the pulse as it is focused through the glass of

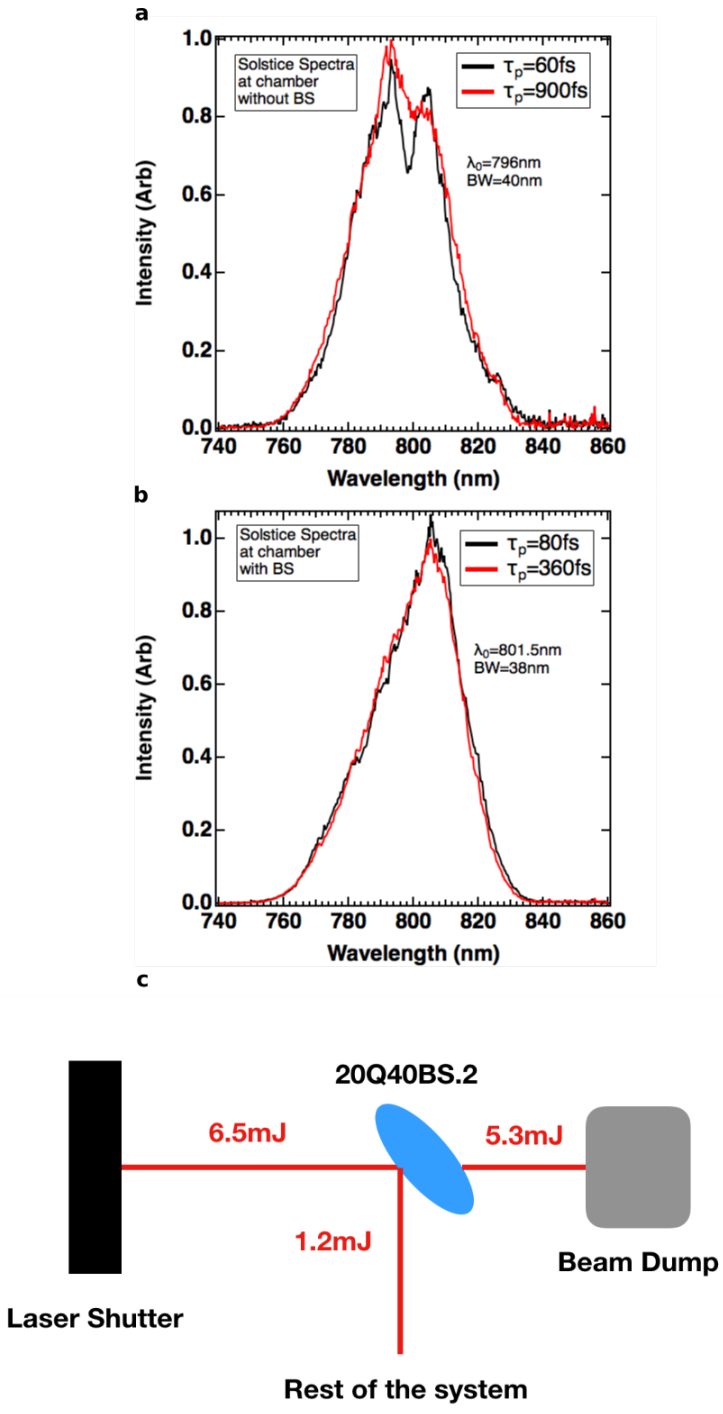

Figure 5.2: a) shows the distorted pulse spectra which resulted from sending the full 6.5mJ pulse through transmissive optics as well as using dielectric mirrors. b) shows the corrected spectra after the laser is attenuated. c) shows the attenuation scheme using a dielectric beam splitter.

the chamber window. We measure the pulse width using a Spectra Physics single shot amplifier and this data is shown in Chapter 4. At a pressure of 10 bar, we find that for long pulse widths, the plasma created with 0.9mJ begins to scatter laser light into our cameras. We therefore limit ourselves to this onset of laser scatter, which is about 320fs. Longer pulses also result in a more asymmetrical autocorrelation signal leading to unreliable pulse width measurement.

5.1.3 Focusing the Laser into High Pressure Chamber

The beam is spatially Gaussian with 10mm diameter and $M^2 < 1.25$. We focus the beam into the chamber using an 1" diameter plano-convex N-BK7 lens (Thorlabs LA1134-B). The f-number is f/6. The lens is mounted on a stage which is used to adjust the height of the breakdown within the chamber, with 10μm step size, to center the plasma in the image plane of the cameras. The chamber is filled with 1-10 bar hydrogen gas, after being purged twice. Its design is detailed elsewhere [7].

Since the laser intensity will be clamped by the breakdown threshold intensity [36], the gas breakdown actually occurs before the focus of the lens. The calibration of the focal point is discussed in Chapter 8. The laser exits the chamber through a second window and is re-collimated using 2" diameter asphere lens (f=50mm). The beam is scattered onto a piece of white paper and a fiber coupled Ocean Optics spectrometer (USB2000) then views the spot and measures the spectrum. The paper is removed and the beam is aligned onto a pyroelectric energy meter (Ophir PE25-C) to measure transmitted energy. The setup for focusing the beam and measuring its transmitted spectrum and energy is shown in Fig. 5.3.

5.2 Imaging the Plasma

Fig. 5.1 shows the plasma imaging system. The chamber has two Mitutoyo optics looking at the breakdown, situated at a right angle to view the plasma from either side, referred

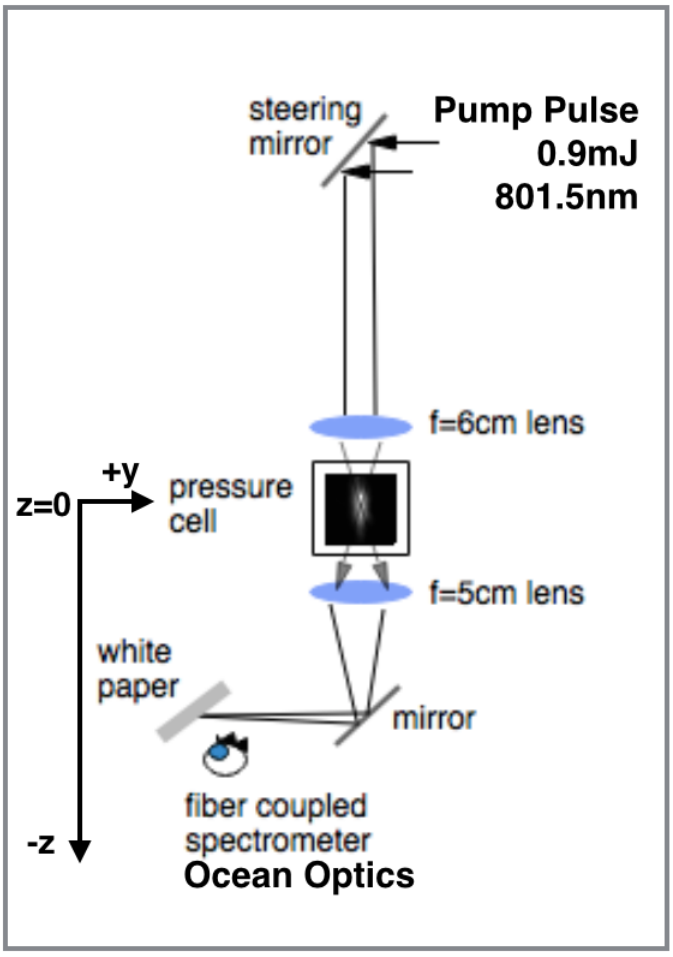

Figure 5.3: Setup for measuring the spectrum of the transmitted laser.

to as "TCCD" and "BSCCD." The microscopes magnify the plasma image 19.5× and ∼15.3×, respectively, onto two CCD cameras. The plasma/beam alignment is optimized by viewing the symmetry of the breakdown in these cameras. The beam splitter is then removed from the main imaging line and the light is passed through a filter wheel with 10nm bandpass filters, a Princeton Instruments spectrometer, and then into a Hamamatsu streak camera, which is made up of a streaking unit and CCD camera. The streak camera collects light from a 3μm wide section of plasma and converts them into electrons in gain channels. The electrons are streaked with an electric field across a phosphor screen which is then photographed by a CCD camera. The operating principle of a streak camera

is shown in Fig. 5.4.

Operating on the 0th order of the spectrometer grating with the slit fully open, the result is an image of the plasma's radius as it develops in time. The bandpass filters can then be rotated out, the spectrometer slit closed to 50μm, and the diffraction grating rotated to 1st order to image the full emission spectrum from a $(3 \times 3)\mu m^2$ slice of plasma. Images of the plasma with a streak camera allow us to see the early time development of the system with a temporal resolution of 32ps.

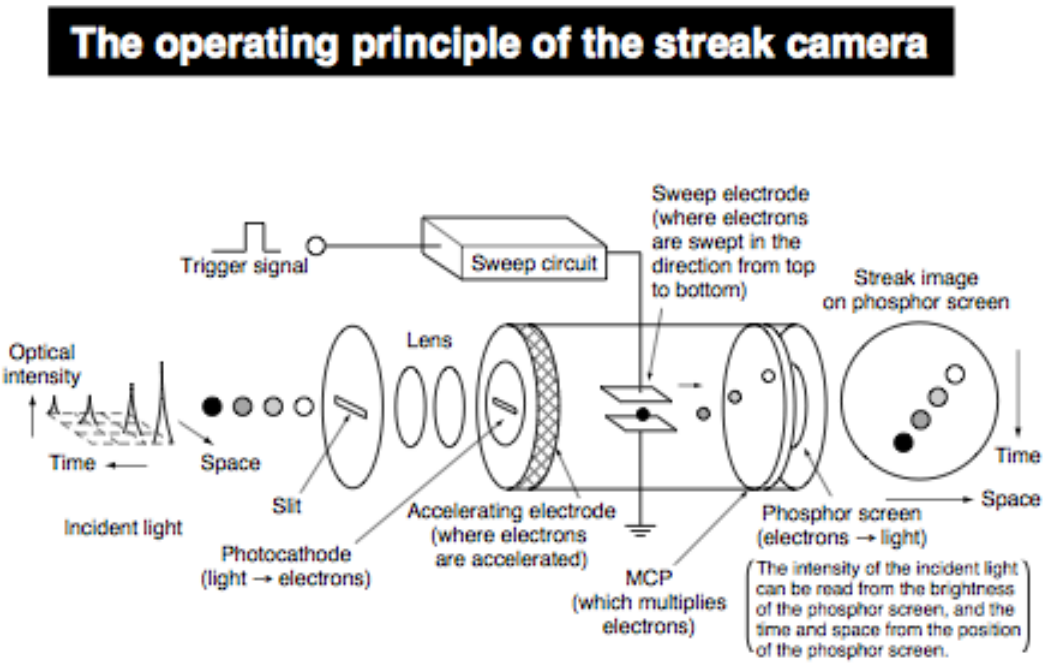

Figure 5.4: Diagram of streak camera operation from Hammamatsu.

5.3 Data Acquisition

Ideal laser beam alignment through the chamber is achieved by observing plasma at 10 bar for 130fs pulse duration, and optimizing the breakdown for 1) identical shape in both CCD cameras and 2) sharpness and brightness of the plasma diameter in the bandpass streak

images. When optimally aligned, the 10 bar, 130fs plasma displays a unique shape which is a helpful benchmark. The beam alignment is then held for the run of the experiment at 10, 3, and 1 bar, which goes as follows:

At the beginning of the run, first 1) the laser energies are measured: incident energy before the lens and then transmitted energy for the chamber under vacuum and at each pressure. The pulse to pulse energy is collected for 2 minutes to ensure stability. 2) Transmitted laser spectra is collected. Placement of the fiber coupled spectrometer is made so that the full laser spot is within the NA of the fiber. Transmitted spectrum is collected for vacuum and each pressure. 3) Plasma images are collected: CCD, and streak bandpass and spectra. At the conclusion of the run, 4) the laser pulse energies are collected to insure stable operation of the laser throughout the experiment.

The 130fs experiment was collected first, and the 320fs experiment on a later day. Laser operating parameters were measured and identical. Identical beam alignment through the chamber was confirmed by optimizing the 10 bar, 130fs plasma and confirming identical breakdown parameters (shape and position of brightest point on plasma). The compressor mirror was then translated slightly to chirp the pulse width to 320fs. This was not found to effect the alignment–i.e., the plasma was bright and symmetric at 320fs.

5.4 Pulse Energy

The difference between the pulse energy measured before the focusing lens and the transmitted energy through the chamber under vacuum is $\sim$0.2mJ. We therefore average the two to find the pulse energy incident on the gas, $i_g = 0.8 \pm 0.1$mJ. Fluctuations in pulse energy $< 1\%$.

CHAPTER 6

Instrument Calibrations

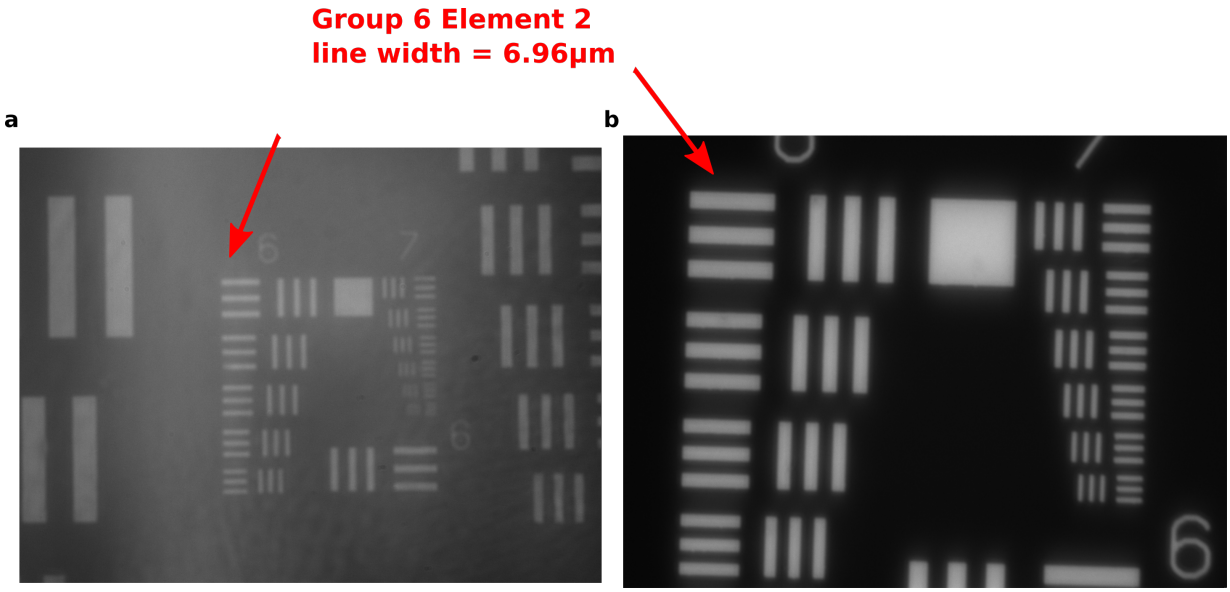

Figure 6.1: Images taken with a) BSCCD and b) TCCD cameras of USAF 1951 target backlit with a mercury lamp [37].

6.1 Magnification

The magnification of the imaging system was measured by A. Bataller for [7] and is recorded in Table 6.1. In the case of the TCCD and BSCCD cameras the spatial scaling was determined by taking a picture of calibrated USAF targets as shown in Fig. 6.1. In the case of the streak camera CCD the scaling was measured by imaging light through the streak camera slit. The size of the slit is adjustable and was set with a micrometer.

CCD Camera	Spatial Scaling ($\frac{\mu m}{pixel}$)	Magnification
TCCD	0.1921±0.1	19.52
BSCCD	0.3054±0.1	15.23
Streak CCD	0.2887±0.04	15.35

Table 6.1: Spatial scaling for CCD cameras.

6.2 Streak Spectral Images

The calibration of the spectral intensity (W/m^3) for the streak camera images taken with the Princeton Instruments spectrometer is shown in Fig. 6.2. Spectra is measured from 1st order image of 150l/mm diffraction grating.

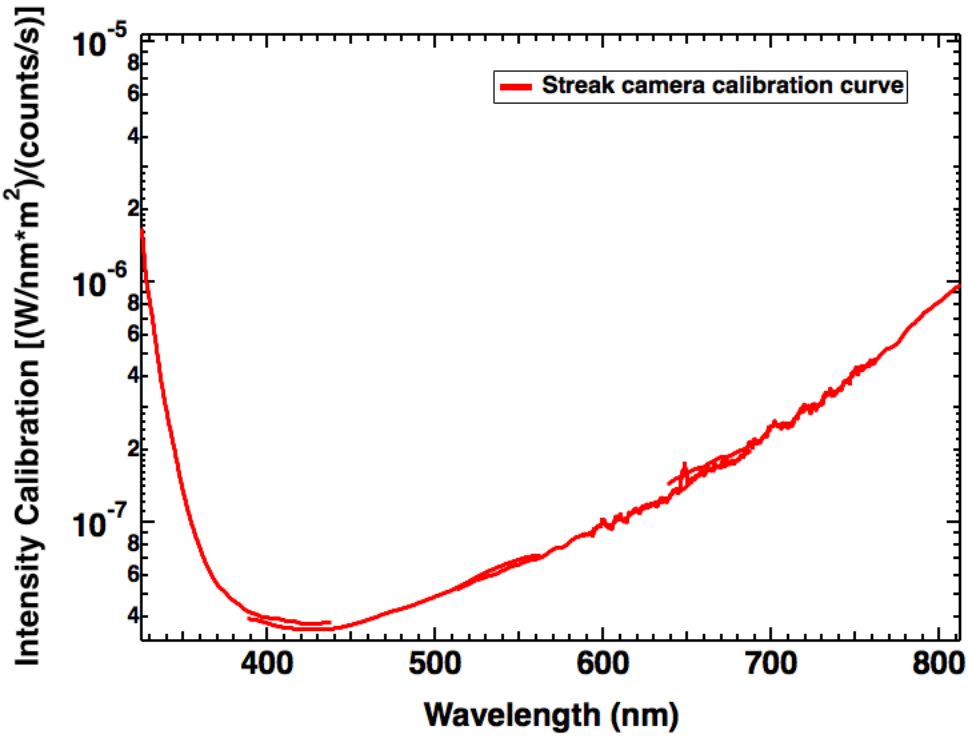

Figure 6.2: Calibration curve for streak camera spectral intensity [37].

The spectral scaling for the image was measured using a mercury lamp and the known emission lines to be $\Delta\lambda = 0.171 \pm 0.001(\frac{nm}{pixel})$. The overall spectral resolution was determined to be 2.8 ± 0.3nm. These calibrations were measured by A. Bataller for [7].

6.3 Streak Bandpass Images

The calibration of the spectral intensity (W/m^2) for streak images taken with bandpass filters is shown in Table 6.2. This calibration was measured by A. Bataller for [7].

Bandpass (nm)	Calibration Constant ($\frac{Wm^{-2}}{counts\ s^{-1}}$)
700	1.79073×10^{-8}
400	2.62149×10^{-8}

Table 6.2: Calibration for streak images taken through bandpass filters.

6.4 Method for Intensity Calibrations

Spectral intensity calibrations were performed by imaging the light from a tungsten halogen lamp of known spectral irradiance, called a standard. Fig. 6.3. shows a diagram of this type of measurement. The standard has a well calibrated spectral irradiance at 50cm. An aperture is placed at the irradiance plane and is imaged by the system. The numerical aperture (NA) of the setup tells us how much light the objective lens is collecting at a distance l from the aperture. The NA is defined

$$NA = n\ sin(\alpha) \approx \frac{D}{2l} \tag{6.1}$$

where the angle α is determined by the distance of the objective lens from the image plane. Since the aperture is radiating into 2π, the counts per second collected by the camera should be multiplied by the factor

$$F = \frac{2\pi l^2}{\pi(\frac{D}{2})^2} = 8\frac{l^2}{D^2} \approx \frac{2}{(NA)^2} \tag{6.2}$$

to correct for the lens capturing only $1/F$ of the sky. We then derive a calibration factor (or curve) between the counts/s measured by the CCD and W/m^3 emitted by the plasma, as reported in sections 6.2 and 6.3. When using the camera to measure an unknown source, another factor F proportional to the NA of the setup must be applied to

the counts. If nothing has changed between the setup when calibrating and when measuring, the factors cancel. For this thesis the factor $F = 41.16$ ($NA \sim 0.22$) is used with the calibration in Fig. 6.2 and Table 6.2 to obtain the spectral intensity of the plasma.

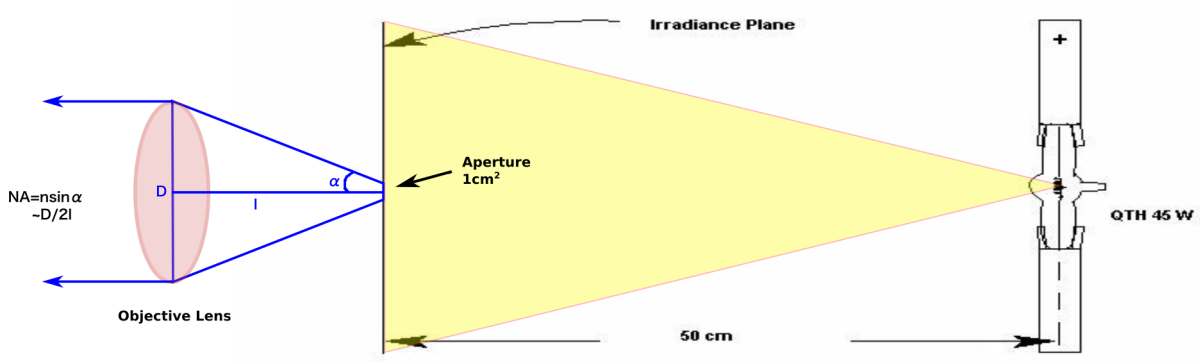

Figure 6.3: Quartz tungsten halogen (QTH) lamp with a well calibrated spectral irradiance at 50cm distance. The aperture on the irradiance plane is imaged by a camera to calibrate for spectral intensity, which will be needed when measuring unknown sources. Reproduced and modified from [38].

6.5 Temporal Scaling & Jitter

The temporal scaling of the streak images can be determined by scattering a femtosecond laser pulse into the camera (or creating breakdown) and then measuring the pixel response as a function of delay. This will show how well the streaking field spreads the electrons in time. This measurement was performed by A. Bataller for [7].

The delay is set by the delay generator box triggering the streak camera. The full trigger circuit is shown in Fig. 6.4. The trigger is set optically by the 80MHz pulse train from the seed laser, using a constant fraction discriminator (CFD) to reduce time walk. The trigger is vetoed until the CFD receives a signal from the laser indicating that a pulse has been selected for amplification (Sync Out). The temporal scaling for 2ns streaking was found $\Delta T = 0.0019561 \frac{ns}{pixel}$.

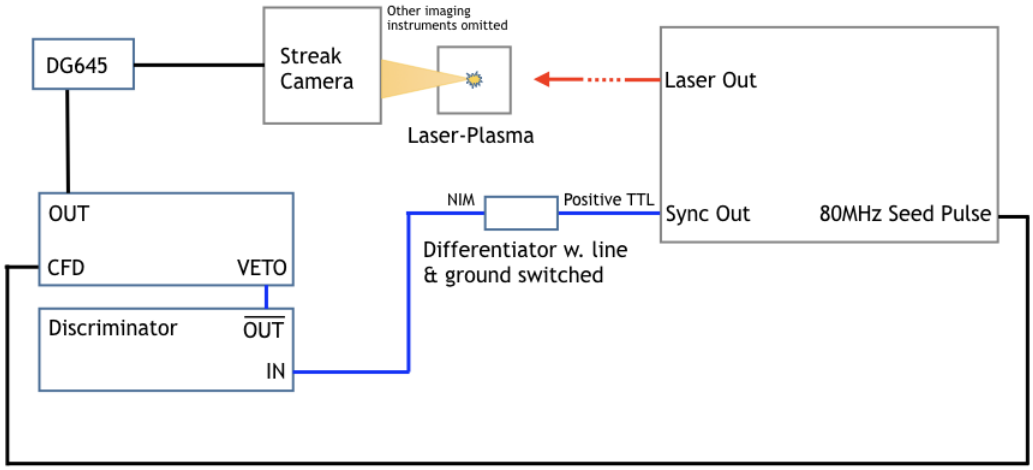

Figure 6.4: Triggering the streak camera with the seed laser photodiode signal and a constant fraction discriminator circuit. The discriminator sets a 10ns pulse width signal of correct polarity which disables the veto and allows a seed pulse to trigger the DG645 delay generator box.

The ultimate temporal resolution is limited by the trigger to trigger jitter of the streaking. The light emission from the plasma must be averaged on the order of 10^3 for a bright image. This averaging is done by taking long exposure images which overlay $\sim 10^3$ streaks. The Sync Out signal produced by the laser does not have sufficient stability to be used as the trigger pulse itself. Fig. 6.5 shows two streak camera images, one taken with the streak triggered off the Sync Out signal alone, and one triggered by the CFD circuit. The temporal jitter is improved at least by a factor of 2.

The trigger levels of the CFD circuit are tuned for best results. Fig. 6.6 shows the final temporal jitter for the streak images presented in this thesis. The jitter is obtained by spatially integrating the streak image and fitting the rise time with an error function given by

$$erf(x) = \frac{1}{\pi}\int_{-x}^{x} e^{-t^2} dt \tag{6.3}$$

The temporal jitter is defined as the HWHM of the gaussian function and found to be

$\delta T = 32$ps.

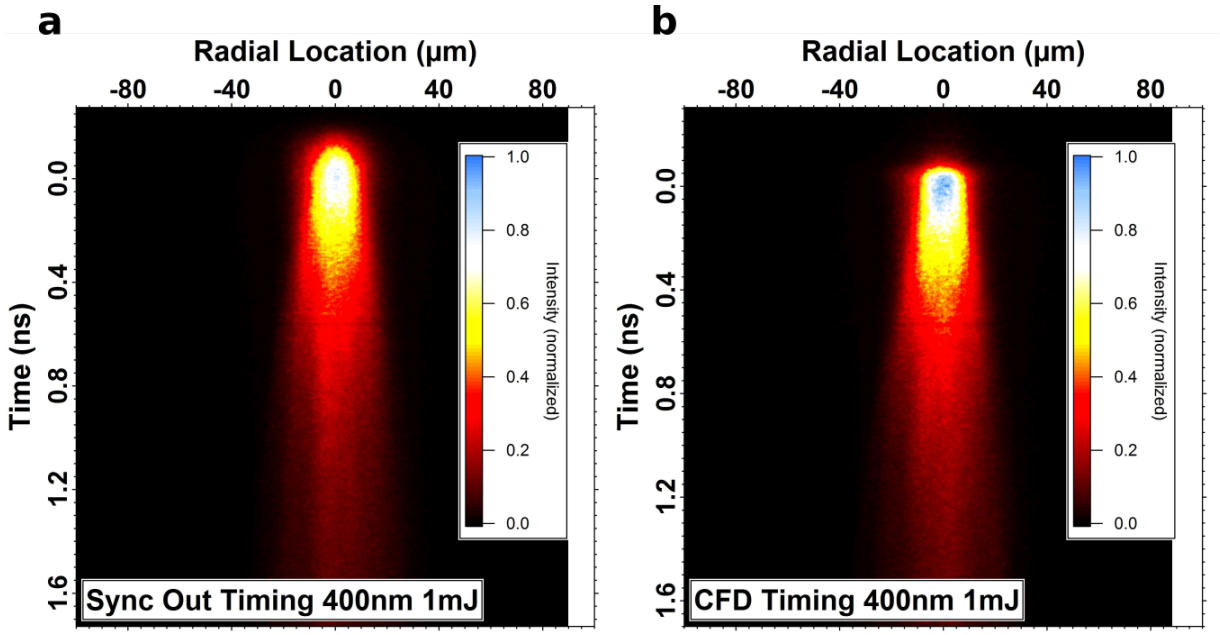

Figure 6.5: a) shows the streak image resulting from the camera being triggered by the Sync Out signal from the laser. b) shows the streak image produced by the CFD trigger circuit.

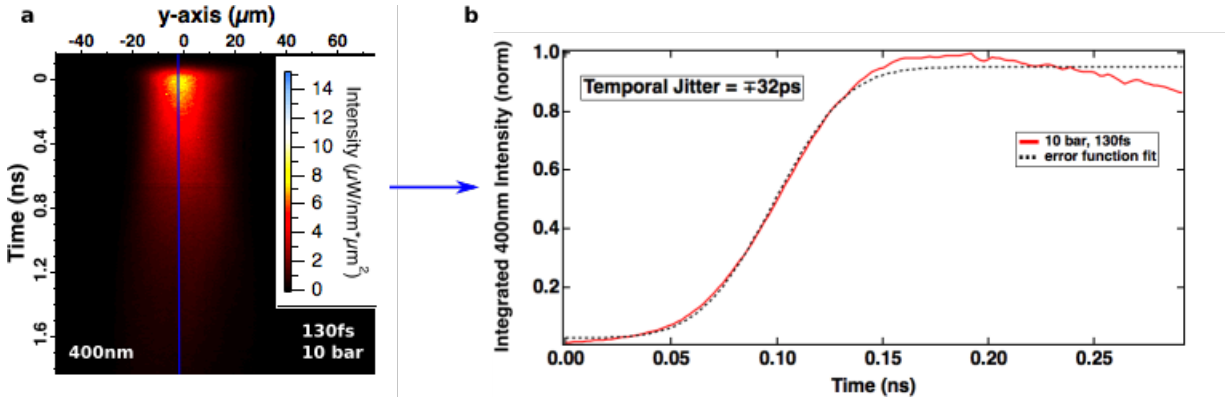

Figure 6.6: Error function fit to the rise time (spatially-integrated) of a streak image of plasma.

6.6 Transmitted Laser Spectra

The Ocean Optics spectrometer is not calibrated for absolute intensity. However the spectral sensitivity should be calibrated to produce a uniformly scaled spectrum of the laser transmission. This was done by using the spectrometer to measure the emission from the QTH standard lamp (made by Oriel). The comparison between the spectrometer response and the true spectral irradiance is shown in Fig. 6.7. The calibration curve is then shown in Fig. 6.8, which was generated by the ratio of the (normalized) spectral irradiance and (normalized) spectrometer response. The results are shown in Fig. 6.9.

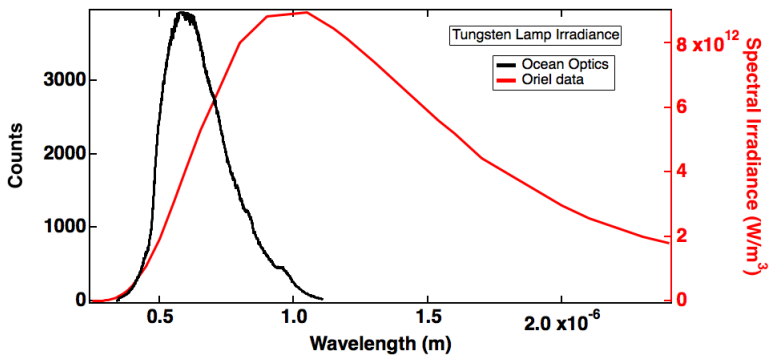

Figure 6.7: Spectral irradiance of tungsten lamp measured by Ocean Optics spectrometer vs. data provided by Oriel for the lamp.

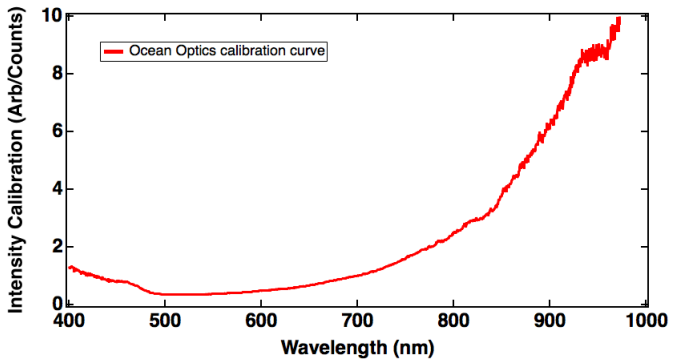

Figure 6.8: Calibration function determined by comparing spectral irradiance measured with Ocean Optics spectrometer and known intensity curve from Oriel.

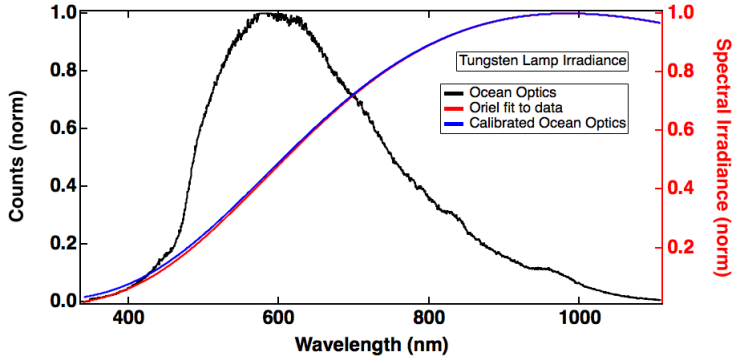

Figure 6.9: The calibration curve then corrects the spectrum.

CHAPTER 7

Experimental Results: Breakdown Properties

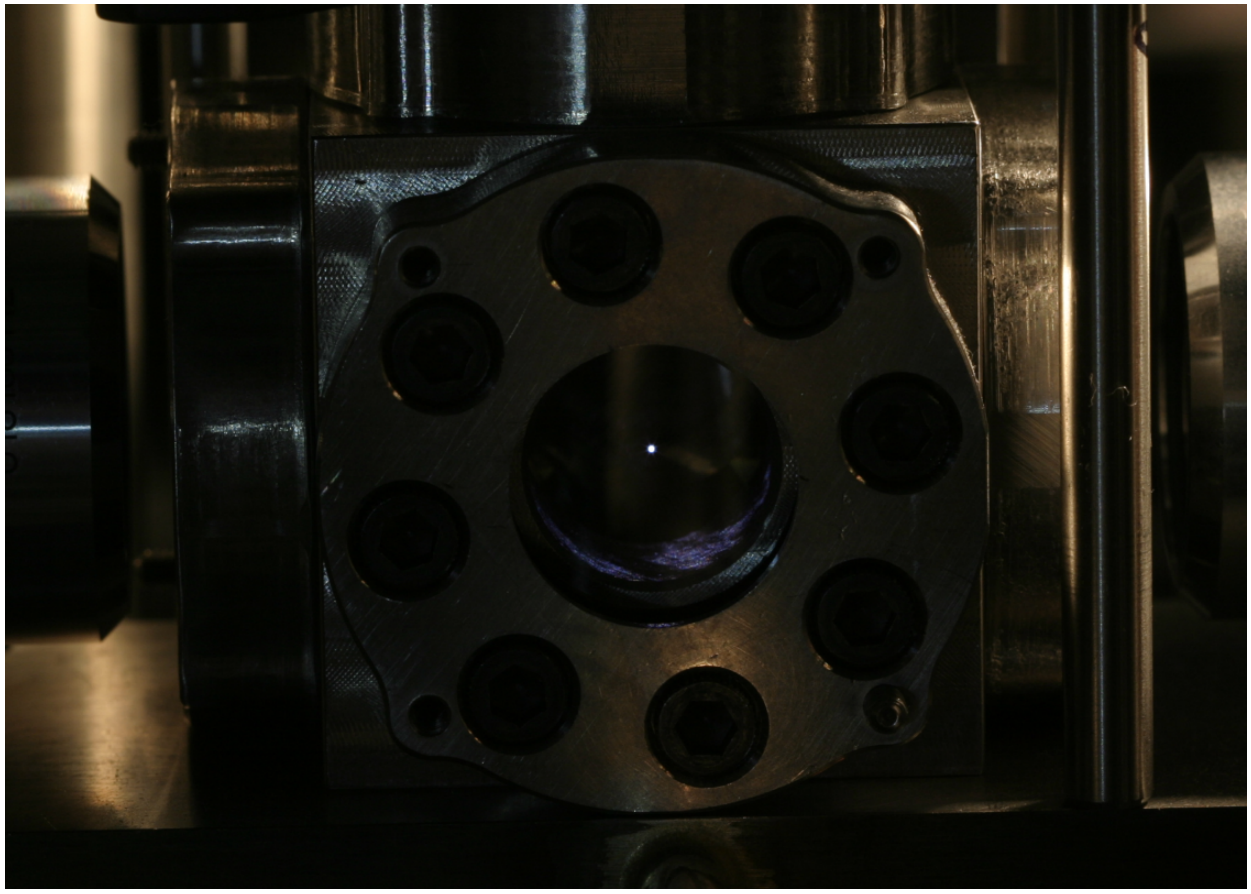

Figure 7.1: Long exposure image of femtosecond laser generated plasma in 10 bar hydrogen gas.

7.1 Breakdown Length

Fig. 7.2 shows time-integrated CCD images of laser breakdown plasma for pulse energy $i_g = 0.8 \pm 0.1$mJ. At low pressure, the 130fs generates a long plasma column $\sim 340 \mu m$. The plasma shrinks as the pressure is increased, but a long narrow tail persists at 10 bar. On the other hand the 320fs pulse generates nearly the same size plasma regardless of pressure. These images give the overall shape of the breakdown which, when coupled with the pulse energy transmitted through the gas and measurements of electron density, will estimate the energy per particle in the plasma. This is an important accounting of the system that can be used to check independent measures of temperature. Additionally the overall shape gives us a clue that nonlinear pulse propagation is possibly developing at 130fs. The long plasma column at 1 bar is a nod to plasma filamentation seen in low f-number focusing.

Plasma length is determined from FWHM fits of 5-pixel wide lineouts from the center of the CCD images, shown in Fig. 7.3. Although this is a somewhat arbitrary cutoff for the edge of the plasma, it provides a good relative measure of plasma length across the pulse widths for a single pressure. The nature of the edge of the plasma will be explored in a subsequent chapter. The lengths are plotted in Fig. 7.4.

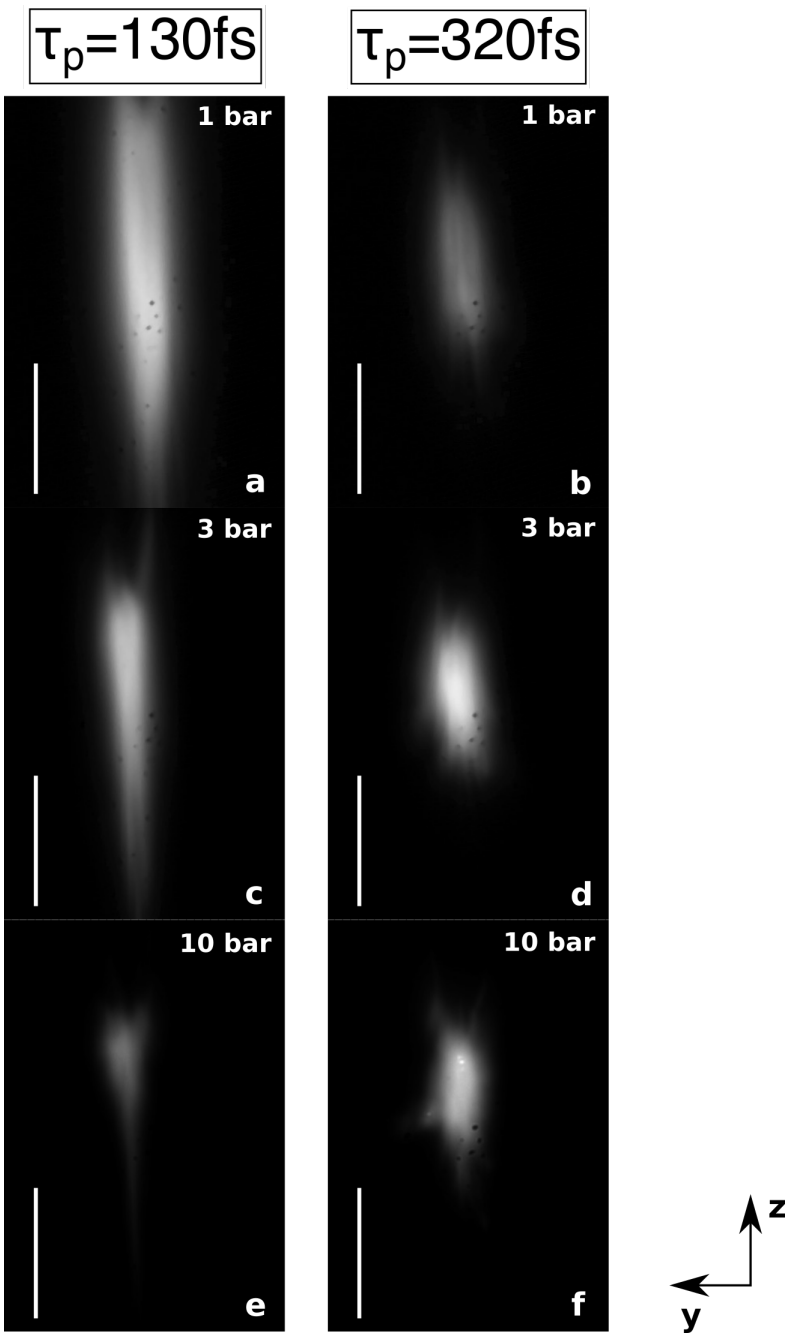

Figure 7.2: CCD images (from BSCCD) of breakdown via 130fs (left) and 320fs (right) pulses in a-b) 1 bar, c-d) 3 bar, and e-f) 10 bar hydrogen gas. The pulse energy is a constant $i_g = 0.8 \pm 0.1$mJ. Exposures capture total light output from 2 breakdowns. Camera gain is not calibrated but is the same for images at same pressure. White bar represents $100\mu m$.

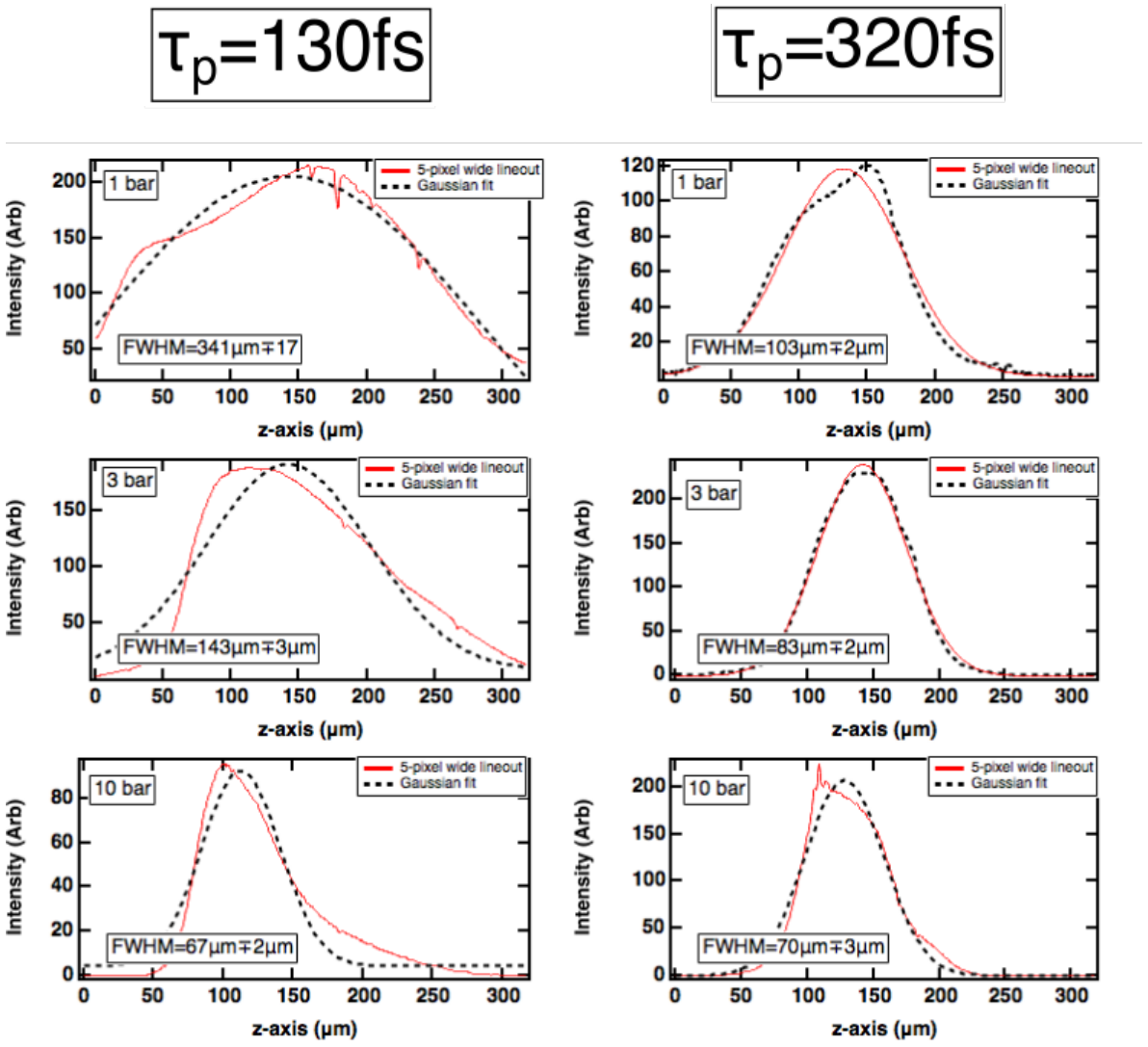

Figure 7.3: Plasma length is determined via FWHM fit of 5-pixel ($\sim 2\mu m$) wide lineout from the center of CCD images shown in Fig. 7.2. The fit is computed with the Levenberg-Marquardt least-squares algorithm to minimize the value of Chi-square.

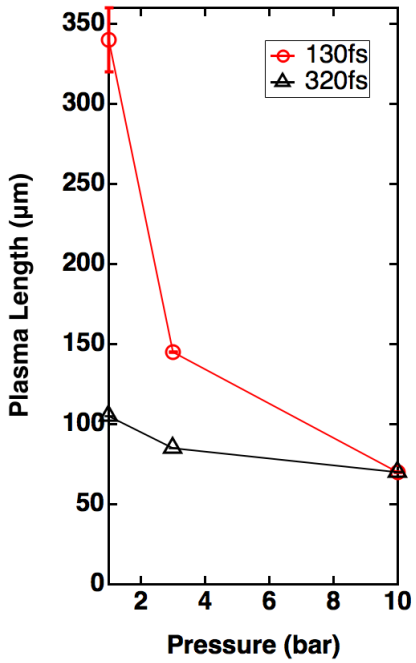

Figure 7.4: Results of the FWHM fit in Fig. 7.3. For every point except one, the error is on the order of the marker width.

7.2 Emission Intensity

Full time-resolved emission spectra from the plasmas is shown Fig. 7.5, which shows us light emission as a function of time for 2ns, with ∼30ps resolution. Brightness is nearly the same for breakdown from both pulse widths at 1 bar, with 320fs slightly brighter. As pressure is increased the long pulse width breakdown overtakes the short pulse and at 10 bar is nearly twice the spectrally integrated brightness at t=0. The spectra are continuous with the Balmer H-alpha line at 656nm emerging later in time as plasma cools. The relative strength of the Balmer line diminishes as the pressure is increased, and even at later times $\sim 1ns$ the spectrum at 10 bar is dominated by the continuum.

There is no striking structural difference between the spectra character at short and long pulse: i.e., one is dominated by line emission and the other is continuous. This indicates that the pressure is playing a key role in determining the plasma emission, not the pulse

width. However, as we reach 10 bar the 320fs breakdown overtakes the 130fs by a factor of 2. This is a significant change, and indicates that we have reached a point in parameter space where the pulse width has a huge effect on the resulting plasma. The spectra show us that the peak of plasma emission is around 400nm. This is useful when deciding to take streaked bandpass images– that is images which show the plasma diameter as a function of time, which we will look at next.

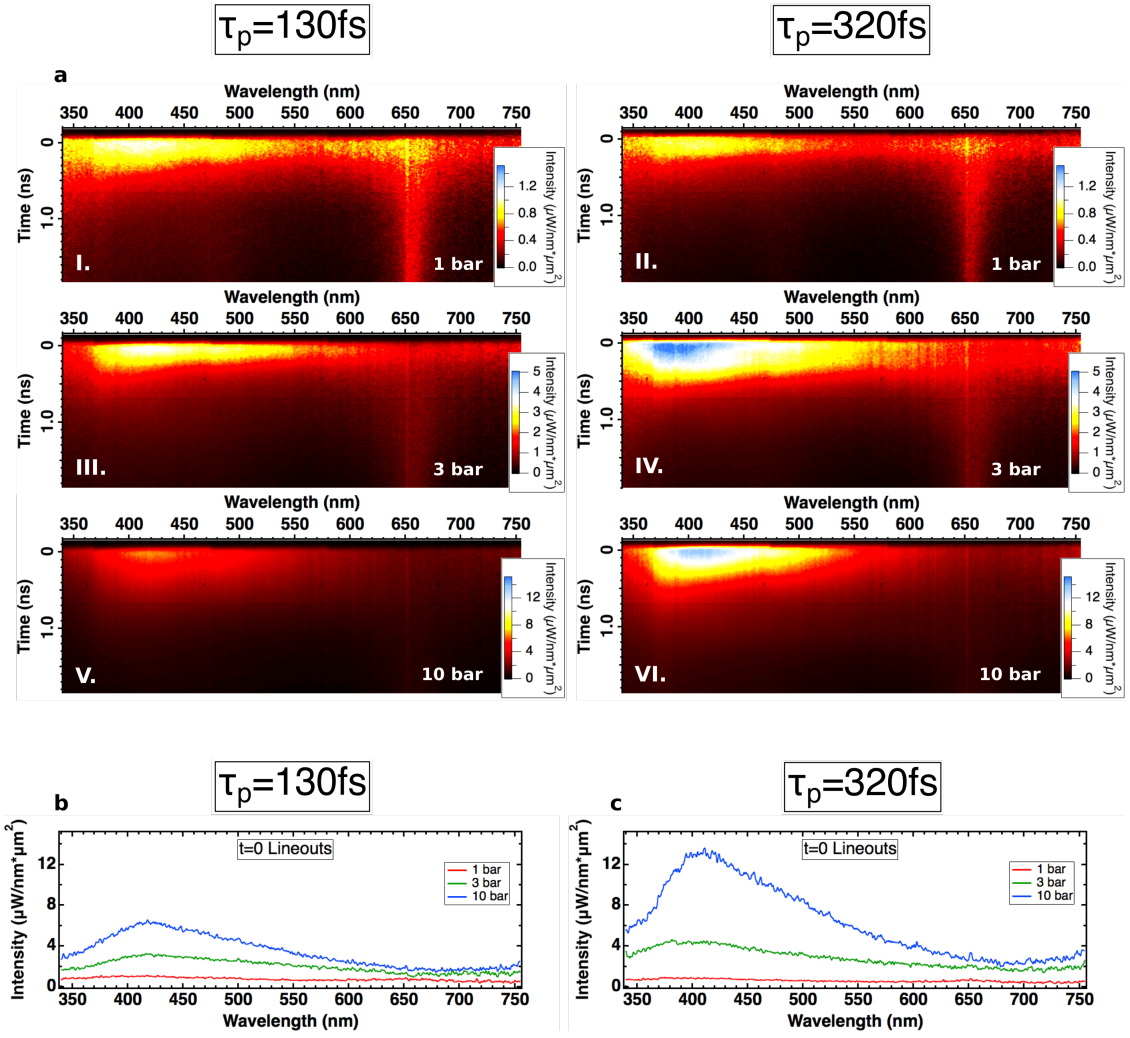

Figure 7.5: a) Time-resolved spectra from a $3\mu m^2$ patch of emission at the brightest point of the plasma for (left) 130fs and (right) 320fs breakdown in I-II. 1 bar, III-IV. 3 bar, and V-VI. 10 bar hydrogen. b-c) shows the t=0 lineouts from the spectra.

7.3 Breakdown Structure & Implications

Hints of the plasma structure can be seen in the CCD images in Fig. 7.2, where at close inspection the 1 and 3 bar plasma generated by the long pulse shows a raked-like emission, while the short pulse looks smooth and continuous. Fig. 7.6a shows intensity calibrated streak images of the brightest, widest point in the breakdowns from Fig. 7.2, viewed through a 400nm bandpass filter, which is near the peak of emission. The images show the projection of the cylindrical plasma emission onto the y-axis and would need to be Abel-inverted to give the emission as a function of the plasma radius. However, this already gives us good confirmation that the two pulse widths generate structurally different plasma. Lineouts at t=0 for the 400nm are shown in Fig. 7.6b. The intensity fluctuations for 320fs generated plasma is also present at long wavelength bandpass emission (Fig. 7.7 shows 700nm), indicating the plasma radiates in this way across the entire spectrum.

The author of this thesis suspects that as the pulse width is increased from 130fs to 320fs the laser energy is present in the breakdown region long enough to drive ionizing electron-neutral collisions. This process forms temperature/density fluctuations which result in corrugated light emission at long times (320fs). However, the peak plasma brightness between the two pulse widths is comparable at low pressures. As the pressure is increased, the collision time is monotonically decreased and collisional breakdown overwhelms the ionization process at 10 bar. This leads to the brightest plasma being generated at 10 bar with the 320fs pulse, where the fluctuations in intensity have been averaged out due to many collisions. This means that plasma generated with 130fs at 1 bar and possibly 3 bar are dense tunneling plasmas. In the next chapter we leverage the laser transmission spectra collected to learn more about the plasma and identify the ionization mechanisms present in breakdown.

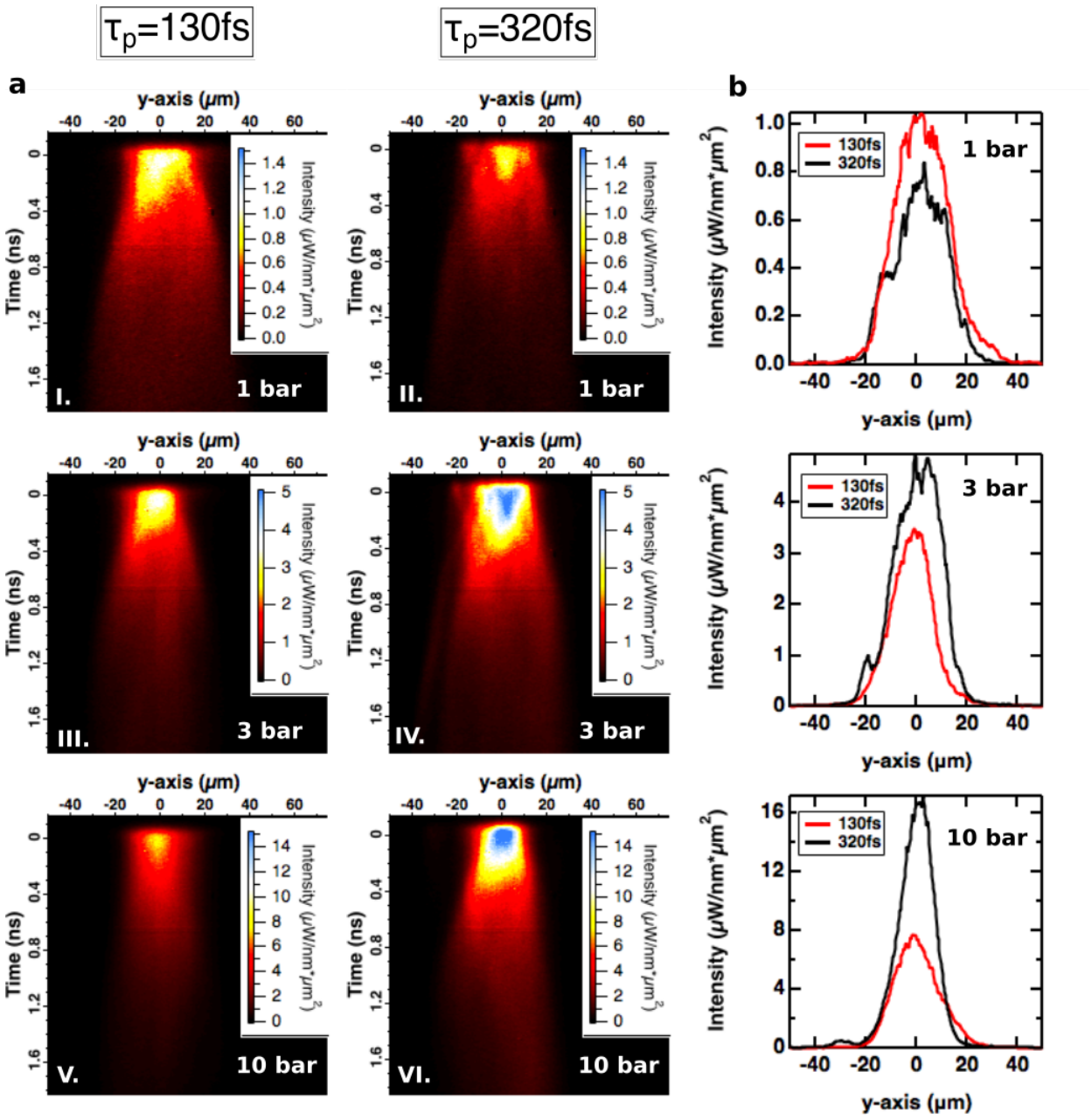

Figure 7.6: a) Streak images of plasma generated via (left) 130fs and (right) 320fs pulse breakdown viewed through 400nm bandpass filter (10nm wide) in I-II. 1 bar, III-IV. 3 bar, and V-VI. 10 bar hydrogen. b) shows the t=0 lineouts from the image.

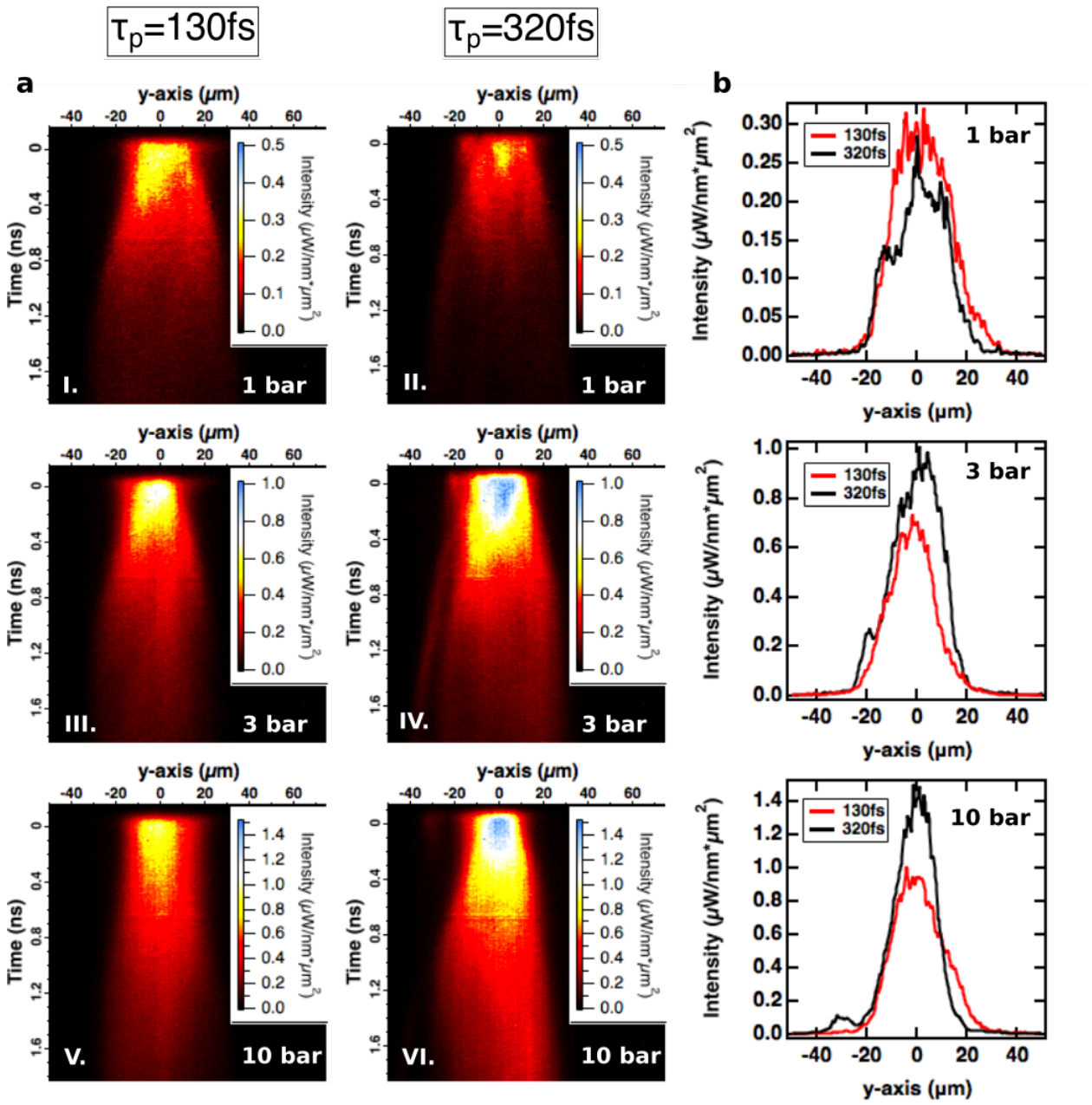

Figure 7.7: a) Streak images of plasma generated via (left) 130fs and (right) 320fs pulse breakdown viewed through 700nm bandpass filter (10nm wide) in I-II. 1 bar, III-IV. 3 bar, and V-VI. 10 bar hydrogen. b) shows the t=0 lineouts from the image.

CHAPTER 8

Supercontinuum Generation

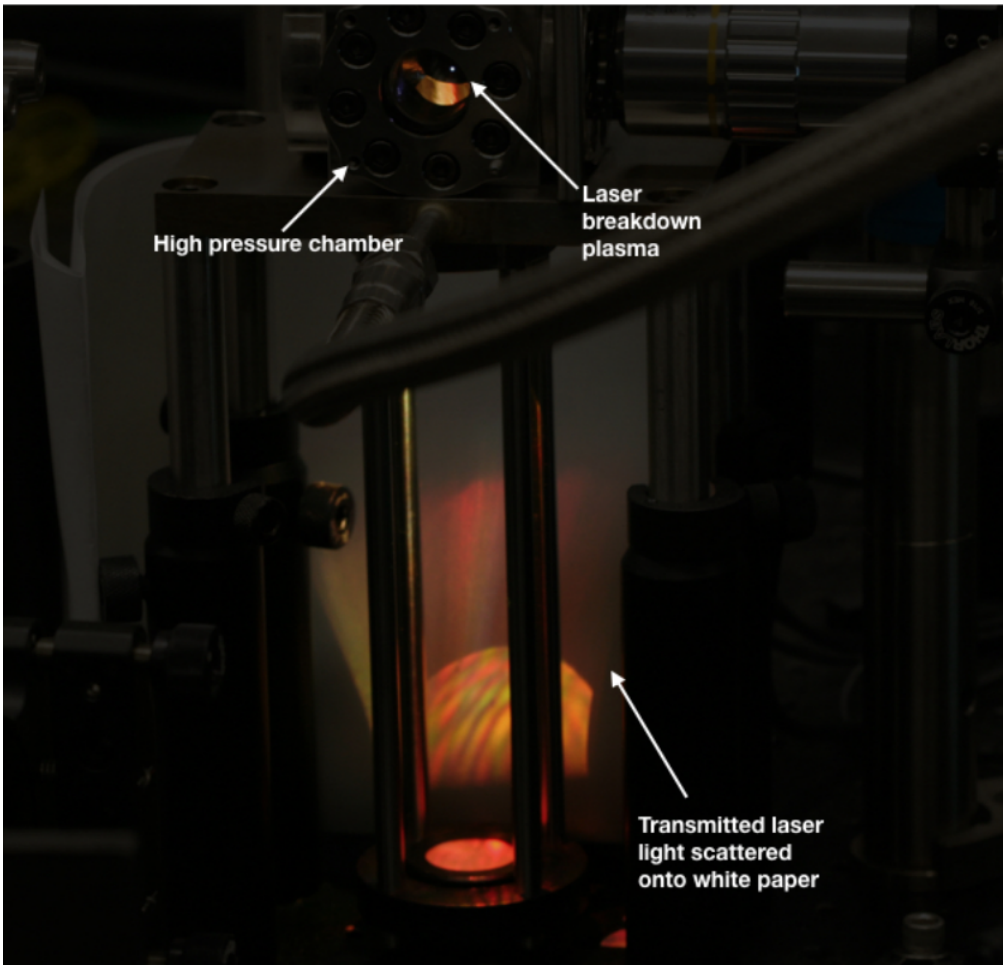

Figure 8.1: Long exposure image of supercontinuum light generated by a 1mJ, ∼45fs pulse focused into 10 bar hydrogen gas.

A stunning result of the gas breakdown process is the generation of supercontinuum light from the ∼800nm laser. Fig. 8.1 shows bright visible light scattered on the optical table.

This is the infrared laser now blue-shifted exiting the chamber after being focused to create breakdown. The laser frequency shifts because of an instantaneous change in the index of refraction, due to the intense light-matter interaction of the laser and hydrogen gas.

To understand this effect we take the laser to be a plane wave propagating in z direction in a nonlinear medium. The electric field is given by:

$$\mathbf{E}(t,z) = \mathbf{E_0} e^{i\phi(t)} \tag{8.1}$$

Where $\mathbf{E_0}$ is the amplitude and $\phi(t)$ is the phase, given by:

$$\phi(t) = \omega_0 t - kz \tag{8.2}$$

ω_0 is the initial frequency and the wavenumber $k = \frac{\omega_0}{c} n(t,z)$, where $n(t,z)$ is the time dependent index of refraction. The instantaneous frequency of the laser in then:

$$\omega(t) = \frac{\partial}{\partial t}\phi(t) = \omega_0 - \frac{\omega_0}{c}\frac{\partial n(t,z)}{\partial t} z \tag{8.3}$$

And the total change in the frequency, or self-phase modulation (SPM) of the laser is:

$$\frac{\Delta\omega}{\omega_0} = -\frac{1}{c}\int_0^L \frac{\partial n(t,z)}{\partial t} dz \tag{8.4}$$

The total shift is the change of the index integrated along the length of the medium L. Many white laser sources have been generated by a shallow-focused laser propagating in gas. The change in the index arises from the nonlinear term n_2 excited in the gas by the intensity of the laser as we saw in Chapter 3. However this term is small and thus requires many meters of propagation to shift the laser to visible frequencies. To model the spectral shifts observed in laser-plasma generation, the index is taken to be that of the plasma derived in Chapter 2 (2.40)

$$n = \sqrt{1 - \frac{\omega_p^2}{\omega^2}} \tag{8.5}$$

The index can be rewritten in terms of the electron density $\rho_e(t,z)$ as

$$n(t,z) = \sqrt{1 - \frac{\rho_e(t,z)}{\rho_{cr}}} \tag{8.6}$$

where $\rho_{cr} = \frac{\omega_0^2 m_e}{4\pi e^2}$ is the critical density where the frequency of the laser ω_0 is equal to the plasma frequency ω_p. For $\rho_e << \rho_{cr}$ the index goes to

$$n \approx 1 - \frac{1}{2}\frac{\rho_e}{\rho_{cr}} \tag{8.7}$$

The critical density for 800nm light is $1.7\times10^{21} cm^{-3}$ which is approximately 20 bar H_2 gas fully ionized. At most we are 50% ionized at 10 bar. Furthermore the application of this model is most important for 1 bar breakdown. We therefore find the expression for the spectral shift of the laser due to breakdown

$$\frac{\Delta\omega}{\omega_0} = +\frac{1}{c}\frac{4\pi e^2}{2\omega_0^2 m_e}\int_0^{L_p}\frac{\partial\rho_e(t,z)}{\partial t}dz \tag{8.8}$$

where L_p is the length of the plasma. We see that the expression has a negative sign indicating a blue-shift of the laser frequency ω_0 due to plasma generation.

8.1 Spectral Blue-Shifting of the Laser

Fig. 8.2 and 8.3 show the transmitted laser spectrum for a 130fs and 320fs pulse focused into 0-10 bar hydrogen gas.

The shift for 130fs is hundreds of nanometers! While the shift for 320fs is between 50 and 100nm. Woods et. al. [20, 19] report small spectral shifts on the order of 10nm for an 800nm laser focused in dense gas (5 bar Xe, Ar, He, Ne). They too are tightly focused (f/5) and note observing breakdown (bright dot). However they only report $\sim 1\%$ absorption of the laser energy by the gas using 0.4mJ pulses. The transmitted energy measured concurrently with the transmitted spectrum for this experiment is shown in Table 8.1. A significant fraction of the pulse energy looks to be absorbed by the gas indicating that we are generating a dense, hot plasma.

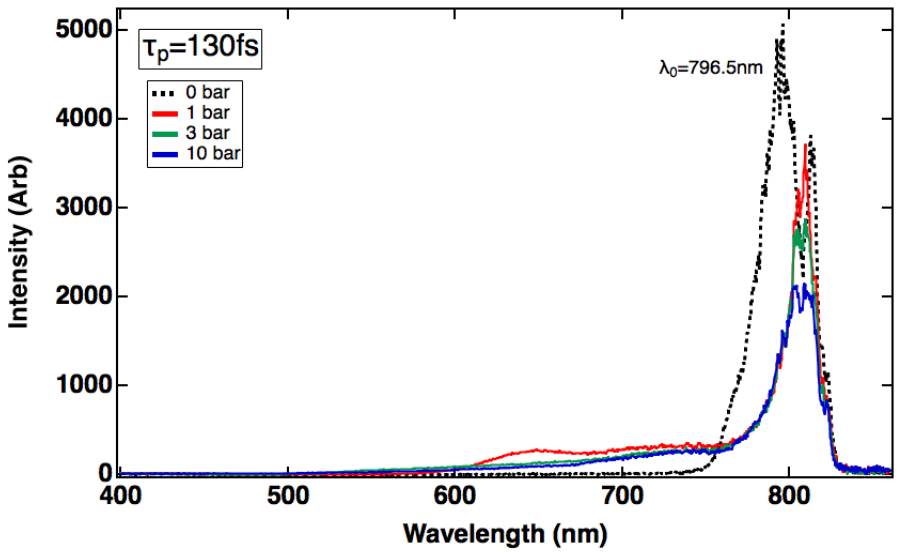

Figure 8.2: Transmitted spectra for 130fs laser focused into 0-10 bar hydrogen gas. Spectra is the time-integrated emission for a single pulse. The 0 bar transmission provides a baseline that shows the effect of our experimental setup (such as lens, chamber windows) on the pulse spectrum.

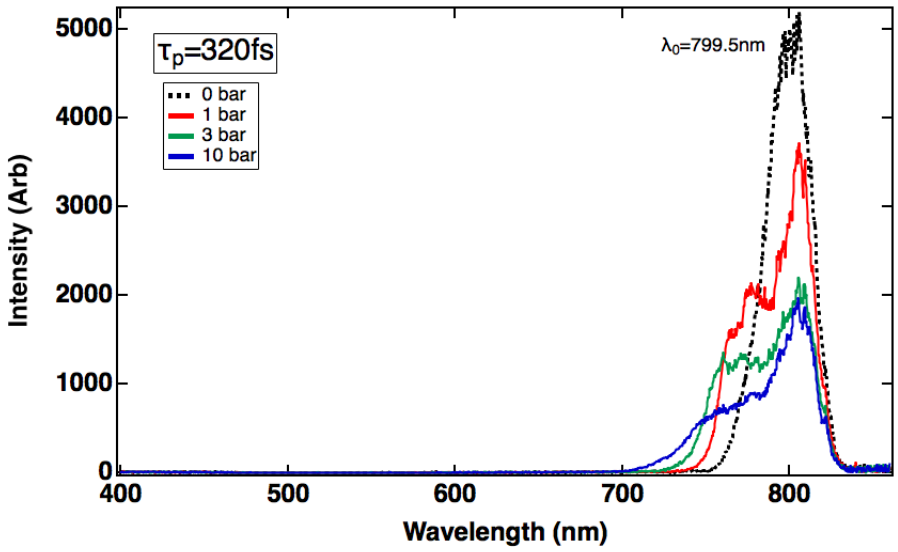

Figure 8.3: Transmitted spectra for 320fs laser focused into 0-10 bar hydrogen gas. Spectra is the time-integrated emission for a single pulse. The 0 bar transmission provides a baseline that shows the effect of our experimental setup (such as lens, chamber windows) on the pulse spectrum.

Pressure (bar)	τ_p (fs)	i_T (μJ)	i_a (μJ)	$\frac{i_a}{i_{T_0}}$
1.0±0.1	130±10	552±3	124±4	0.18±0.1
	320±50	591±1	96±2	0.140±0.002
3.0±0.1	130±10	483±3	193±4	0.29±0.01
	320±50	440±10	250±10	0.36±0.02
10.0±0.1	130±10	411±3	265±4	0.40±0.01
	320±50	360±20	327±20	0.48±0.03
0.0±0.1	130±10	676±2	∼	∼
	320±50	687±2	∼	∼

Table 8.1: The pulse energy absorbed by the gas can be estimated as the difference between i_{T_0}, the transmitted energy at 0 bar, and i_T. This is a good assumption if we do not expect a large amount of energy to be reflected. Laser scatter only becomes evident in the cameras imaging the plasma at a pressure of 10 bar, so this is where we may expect some discrepancy. Additionally the 10 bar plasma will defocus the laser the most, making our collection of the pulse from the exit chamber window the least reliable.

8.2 Homogeneous Plasma Model

(8.8) predicts a single frequency shift of the laser due to plasma creation, whereas we observe a continuous shift. To stretch this model we can interpret the maximum frequency shift as relating the maximum rate of ionization. Additionally we can assume that the rate of ionization is uniform over the plasma length. The maximum blue shift in the transmitted laser spectra can then be expressed as

$$\frac{\Delta\omega_{max}}{\omega_0} = +\frac{1}{c}\frac{4\pi e^2}{2\omega_0^2 m_e}(\frac{d\rho_e}{dt})_{max}L_p \tag{8.9}$$

or

$$\frac{\Delta\lambda_{max}}{\lambda_0} = -\frac{1}{c^3}\frac{\lambda_0^2 e^2}{2\pi m_e}(\frac{d\rho_e}{dt})_{max}L_p \tag{8.10}$$

The maximum spectral shift is found in the next section and (8.10) is applied.

8.3 Maximum Spectral Shift

Fig. 8.4 and 8.5 show the transmitted laser spectra zoomed in to find the maximum shift. The same threshold intensity is used to find λ_{max}. The results are shown in Table 8.2.

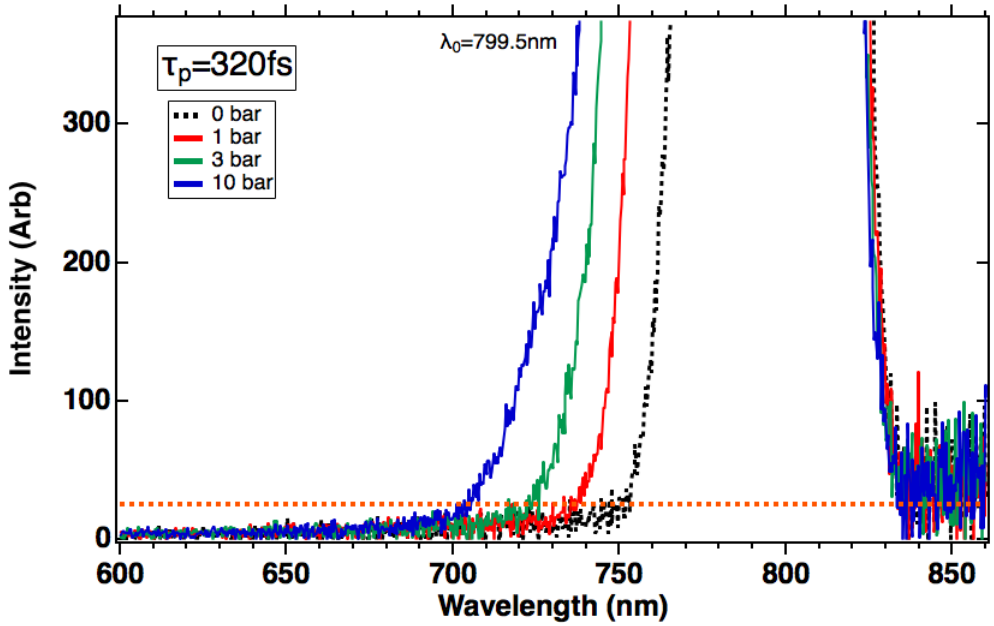

Figure 8.4: Transmitted laser spectra from 8.3 is shown zoomed in to find the maximum spectral shift.

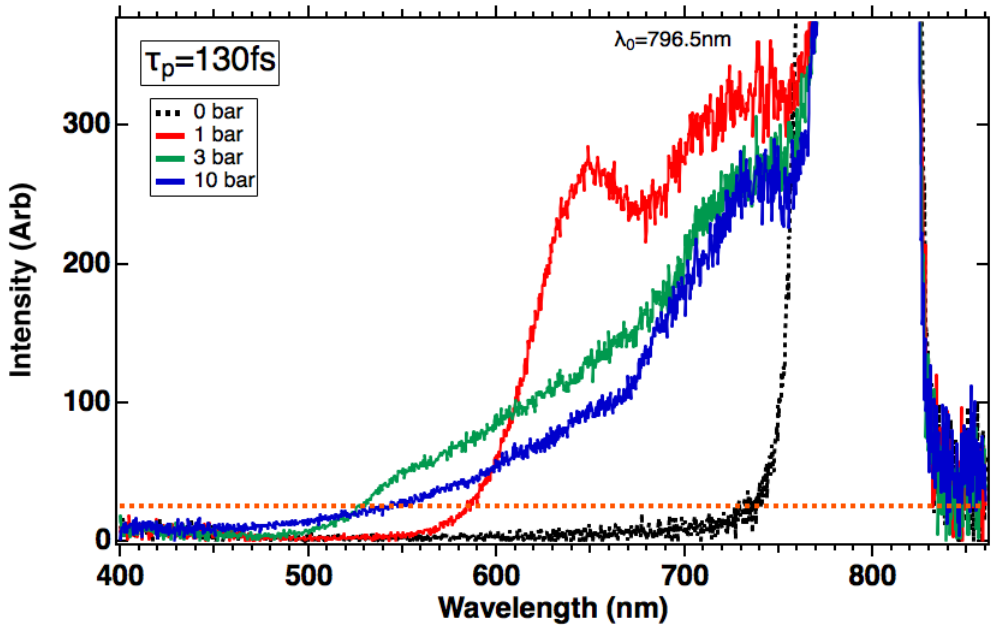

Figure 8.5: Transmitted laser spectra from 8.2 is shown zoomed in to find the maximum spectral shift.

Pressure (bar)	τ_p (fs)	λ_{max} (nm)	$\Delta\lambda_{max}$ (nm)	λ_0 (nm)	$\frac{\Delta\lambda_{max}}{\lambda_o}$
1.0±0.1	130±10	586±2	211±2	797±22	0.265±0.007
	320±50	735±2	65±2	800±19	0.081±0.003
3.0±0.1	130±10	527±2	270±2	797±22	0.34 ±0.01
	320±50	725 ±2	75±2	800±19	0.094±0.003
10.0±0.1	130±10	543 ±5	254±5	797±22	0.32±0.01
	320±50	705±3	95±3	800±19	0.120±0.005

Table 8.2: Maximum spectra shift is measured as a function of pressure and laser pulse width.

You can see from Table 8.2 that λ_0 reported is not the 801.5nm of the Solstice Ace laser. This is because our optics have an effect on the laser spectrum. This is shown in Fig. 8.6. Fig. 8.6a shows the laser pulse spectrum for short and long pulse widths (though not exactly the same as those used in the experiment) right before the laser is focused into the

chamber by the lens. This accounts for any effects that our optics have had on the pulse leading up to focusing. For the most part this looks the same as Fig. 3.4. Fig. 8.6b and 8.6c show the pulse spectra for the pulses used in this experiment *after* they have been focused into the chamber (under vacuum) and recollimated on the other side. This shows the effect of our lenses and chamber windows on the spectrum. You can see the central wavelength has been shifted in both cases– 5nm for the short pulse. The short pulse also has significant spectral distortion. This is why 130fs was choosen as the shortest pulse width for this experiment. Shorter pulses resulted in what the author of this thesis deemed to be too much spectral distortion.

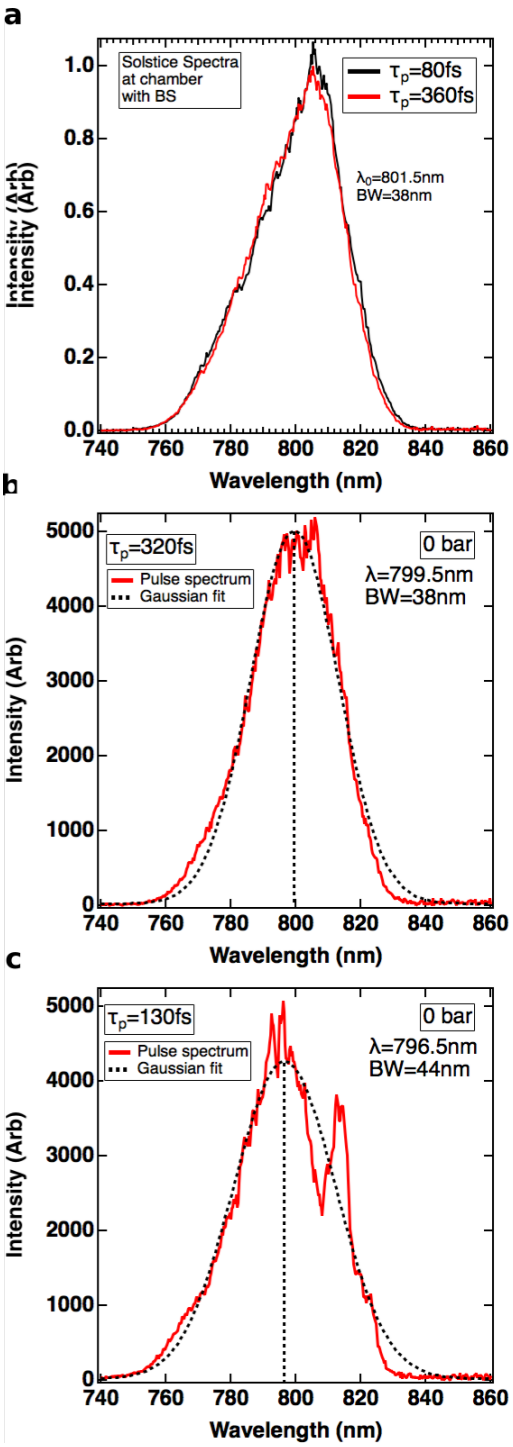

Figure 8.6: a) shows the spectrum of the laser before the focusing lens. b-c) show pulse spectra after the laser has been focused into the chamber under vacuum and recollimated on the other end. b) shows the 320fs pulse and c) shows the 130fs pulse.

8.4 Maximum Ionization Rate

From the spectral shift in Table 8.2 we can use (8.10) to calculate the ionization rates. The results are shown in Table 8.3. This yields a very nice result. For a pressure of 1 bar

Pressure (bar)	τ_p (fs)	Plasma length (μm)	$\frac{\Delta\lambda_{max}}{\lambda_o}$	$(\frac{d\rho_e}{dt})_{max}$ ($10^{17}\text{cm}^{-3}\text{fs}^{-1}$)
1.0±0.1	130±10	340±20	0.265±0.007	2.9±0.2
	320±50	103±2	0.081±0.003	2.9±0.1
3.0±0.1	130±10	143±3	0.34 ±0.01	8.8±0.3
	320±50	83 ± 2	0.094±0.003	4.1±0.2
10.0±0.1	130±10	67±2	0.32±0.01	17±1
	320±50	70 ± 3	0.120±0.005	6.2±0.4

Table 8.3: Maximum ionization rate determined from the spectral shift, plasma length and (8.10).

the maximum spectral shift is different by a factor of 3 for the different pulse widths. At first glance this indicates very different ionization rates and one might conclude different ionization processes generating the two plasmas. However, the measurement of the plasma length perfectly accounts for this. The combined measurement of the plasma length and spectral shift yields nearly identical ionization rates for 1 bar breakdown! At higher pressures the rates are seen to diverge.

Here we make the assumption that for the ionization rate to be identical between the two breakdowns, the ionization process must be the same. Additionally for the ionization rate to be identical across pulse widths of 100-300fs the dominant process must be tunneling. Cascade ionization is an exponential growth effect that would benefit from the longer pulse width, resulting in a different maximum ionization rate. Furthermore, the estimated collision time for this process (electron-neutral atom collisions) at temperatures on the order of $1eV$ is $>$ 100fs. For 1 bar, the rate equation from Chapter 1 becomes

$$\frac{d\rho_e(t)}{dt} = \eta'(\rho_{n_0} - \rho_e(t)) \tag{8.11}$$

which yields the solution

$$\rho_e(t) = \rho_{n_0}(1 - e^{-\eta' t}) \tag{8.12}$$

and the ionization rate

$$\frac{d\rho_e(t)}{dt} = \eta' \rho_{n_0} e^{-\eta' t} \tag{8.13}$$

The tunneling rate η' is proportional to the electric field. If we assume the field turns on in the gas as a step function, the maximum rate of ionization occurs at t=0:

$$(\frac{d\rho_e}{dt})_{max} = \frac{d\rho_e(t=0)}{dt} = \eta' \rho_{n_0} \tag{8.14}$$

Using (8.14) and the ionization rate calculated from (8.10) we can solve for the tunneling rate constant η'. The auto-tunneling rate derived by Oppenheimer [39] and later Keldysh [24] gives an analytic expression for η' as a function of the electric field:

$$\eta' = \sqrt{\frac{6\pi}{4}} \frac{\mathcal{E}_{ion}}{\hbar} (\frac{eE\hbar}{m_e^{\frac{1}{2}} \mathcal{E}_{ion}^{\frac{3}{2}}})^{\frac{1}{2}} \times exp[-\frac{4}{3} \frac{\sqrt{2m_e} \mathcal{E}_{ion}^{\frac{3}{2}}}{e\hbar E}] \tag{8.15}$$

where E is the electric field and $\mathcal{E}_{ion}$ is the ionization potential. Dividing the ionization rate from Table 8.3 by the neutral density, one can obtain the tunneling rate at t=0. Using (8.15) the electric field is then calculated. This is done for both pulse widths at 1 bar, obtaining two electric fields which are averaged to yield the effective breakdown field:

$$E_{BD} = (4.77 \pm 0.04) \times 10^8 V/cm \tag{8.16}$$

or an intensity of

$$I_{BD} = (6.3 \pm 0.1) \times 10^{14} W/cm^2 \tag{8.17}$$

8.5 Breakdown Fields

The plasma is formed at different locations along the focusing path of the laser. The relative position is measured by the location of the $10\mu m$-resolution motorized stage on which the focusing lens is mounted. The location (not scaled) of the brightest, widest point of the breakdown as a function of pulse width and gas pressure is given in Table 8.4.

From the knowledge of the breakdown intensity for 1 bar (8.17) along with the measured laser pulse widths, we can calibrate the focus of the laser using Gaussian optics. With the focal point and Table 8.4, we may then calculate the breakdown electric fields for the remaining gas pressures.

First, the focal point is calculated from the intensity:

$$I_{BD} = \frac{2\, i_g}{\tau_p\, \pi\, w(z_{BD})^2} \tag{8.18}$$

where $w(z_{BD})$ is the spot radius at the location of breakdown, which is given by the expansion of a Gaussian beam:

$$w(z) = w_0 \sqrt{1 + \frac{z^2}{z_r^2}} \tag{8.19}$$

where w_0 is the spot radius at the focus of the laser

$$w_0 = \frac{2\lambda_0 f}{\pi D} \tag{8.20}$$

f is the focal length of the lens (6cm) and D is the diameter of the beam before focusing (10mm). For this experiment $w_0 \sim 4\mu m$. The term z_r is the Rayleigh length given by

$$z_r = \frac{\pi w_0^2}{\lambda_0} \tag{8.21}$$

The results for the focal point are given at the end of Table 8.4. Once the focal point was calibrated (8.18), (8.19) and the plasma locations z_{BD} were used to determine the breakdown intensities as a function of pressure and pulse width. The results are shown in Fig. 8.7.

8.6 Ionization Rate Constants

We can use the laser intensities from Fig. 8.7 to determine the tunneling and cascade rate constants for the electron density rate equation developed in Chapter 1. The tunneling rate η' is determined from plugging the breakdown electric field back into (8.15). We assume that the ionization threshold is clamping the maximum intensity the laser can reach

Pressure (bar)	τ_p (fs)	Breakdown Location z_{BD} (mm)
1.0±0.1	130±10	4.23±0.02
	320±50	4.44±0.02
3.0±0.1	130±10	4.11±0.02
	320±50	4.39±0.02
10.0±0.1	130±10	4.02±0.02
	320±50	4.34 ± 0.02
f_0	130±10	4.59±0.05
	320±50	4.67 ± 0.03

Table 8.4: Relative breakdown locations of the gas as a function of pulse width and pressure. The calibrated focal point f_0 is shown at the bottom of the table. The z_{BD} locations with respect to the geometry of the experiment are depicted in Fig. 8.7.

in the gas and that the intensities in 8.7 are the same for the same pressure. We therefore take the values determined for 130fs breakdown. These are the same within error as the 320fs values, but more precise since the error on the pulse width is much less at 130fs. The values for η' can only be determined by a factor of 2 due to the exponential dependence on the electric field. The results are shown in Table 8.5.

Pressure (bar)	Breakdown Electric Field (10^8V/cm)	η (at t=0) (s^{-1})	η' (s^{-1})
1.0±0.1	4.77±0.04	(6.5±0.5)×10^{12}	(6.0±0.4)×10^{12}
3.0±0.1	3.8±0.5	(2.3±0.4)×10^{13}	(12±10) × 10^{11}
10.0±0.1	3.0±0.3	(8±1)×10^{13}	(9±8) × 10^{10}

Table 8.5: Rate constants calculated for the plasma as a function of pressure.

The cascade constant η is determined by the simple relation

$$\eta(t) = \rho_n(t)\, v_e \sigma_m \tag{8.22}$$

where $\rho_n(t)$ is the neutral density, which changes as a function of time as the gas is ionized

($\rho_n(t=0) \equiv \rho_{n_0}$), v_e is the electron quiver velocity in the electric field, and σ_m is the cross section for momentum transfer. The average quiver energy reaches $20eV$ for 800nm light at the field strengths reported in Table 8.5, which is well above the ionization potential of hydrogen. The quiver energy is the energy an electron absorbs from the electric field E during a collision [40, 23]. Omitting collisional losses this is given by

$$\frac{d\epsilon}{dt} = \frac{e^2 E^2 \tau_c}{m_e(\omega^2\tau_c^2 + 1)} \approx \frac{\mathcal{E}_p}{\tau_c} \tag{8.23}$$

where $\mathcal{E}_p$ is the pondermotive or quiver energy and τ_c is the momentum transfer collision time. One can assumed that any electron that reaches the ionization energy $\mathcal{E}_{ion}$ will soon produce a new free electron. Dividing (8.23) by $\mathcal{E}_{ion}$ thus yields the cascade ionization rate:

$$\eta = \frac{e^2 E^2 \tau_c}{m_e(\omega^2\tau_c^2 + 1)\mathcal{E}_{ion}} \tag{8.24}$$

However for this experiment the quiver energy is equal to or greater than the ionization energy and we thus limit

$$\eta = \frac{1}{\tau_c} \tag{8.25}$$

which is (8.22). The cross sections were obtained from [41] and are between $4{\times}10^{-16}cm^{-2}$ and $8{\times}10^{-16}cm^{-2}$. The quiver velocity [42] is given by

$$v_e = \frac{eE}{m_e\omega} \tag{8.26}$$

and is on the order of $10^8 cm/s$, or 1% the speed of light, for the electric fields measured in this experiment. The results for η at t=0 (so the neutral density is given by the gas pressure) are reported in Table 8.5. Note the collision time $\tau_c = \frac{1}{\eta}$ for 1 bar is about 150fs.

8.7 Solution to the Modified Rate Equation

We can now solve our model for the electron density as a function of time, equation (1.6):

$$\frac{\partial \rho_e(t)}{\partial t} = \eta' \, \rho_n(t) + \eta(t) \, \rho_e(t)(1 - \frac{\rho_e(t)}{\rho_{n_0}}) \tag{8.27}$$

$$\frac{\partial \rho_e(t)}{\partial t} = \eta' \, \rho_n(t) + (\rho_n(t) \, v_e \sigma_m) \, \rho_e(t)(1 - \frac{\rho_e(t)}{\rho_{n_0}}) \tag{8.28}$$

$$\rho_n(t) = \rho_{n_0} - \rho_e(t) \tag{8.29}$$

This is solved numerically in Mathematica using a boxcar electric field (of the amplitude reported in Table 8.5) from t =0 to t =350fs. The electron density equation for tunneling ionization alone (no term due to collisions, which is the second term on the right in (8.27)) is also solved. The results are plotted in Fig. 8.8-8.10.

We see at low pressure (Fig. 8.8) there is almost no difference between the two curves. This is not surprising: for a collision time of ∼150fs we should not expect collisions to play a significant role at 1 bar. At 3 bar (Fig. 8.9) the curves have started to separate. There is a large spread in error due to the fact that we could not solve for the electric field directly as we did at 1 bar by assuming a single ionization process. The collision time $\tau_c = \frac{1}{\eta}$ for 3 bar is ∼45fs. Here collisions may start to make a difference in the degree of ionization at longer pulse widths.

Fig. 8.9 shows the results for 10 bar. Now collisions clearly play a key role in the ionization of the gas. The model predicts that the plasma is almost fully ionized around 130fs due to collisions, and that the electron density then slowly grows to the neutral gas pressure within 320fs. This indicates that the factor of ∼2 difference in brightness (Fig. 7.5) observed in the breakdown of 10 bar is primarily due to collisional heating of the electrons (recall equation 2.52 for Bremsstrahlung radiation). The collision time $\tau_c = \frac{1}{\eta}$ for 10 bar is ∼12fs.

The corrugated intensity profiles shown in the bandpass streak images for 320fs breakdown at 1 and 3 bar, shown in Fig. 7.6 and 7.7, could be due to the role of collisions on this timescale. It looks like pockets of either more dense or more hot plasma have formed in the breakdown. For 1 bar, there is essentially no difference predicted for electron density due to collisions. However, the plasma generated at 320fs is not as bright as the 130fs. They should be equal brightness. Recall that 1 bar breakdown produced a nearly 400μm plasma at 130fs. There could be some self-focusing of the laser balanced with plasma-

induced defocusing to create a mini-filament. If that is the case, the electric field at 130fs, 1 bar could be more than we have estimated and result in a slightly brighter plasma. We discuss the role of self-focusing in detail in the Conclusions. The structure observed in the plasma at 320fs, 1 bar then could be due to the 1 or 2 collision times which have elapsed by the end of the pulse.

At 3 bar, the two curves (collisions and no collisions) start to separate. At times greater than 130fs, it is likely that collisions are playing a role in the ionization of the gas. The plasma at 3 bar, 320fs overtakes in brightness the 130fs breakdown at this pressure. The intensity fluctuations observed in the streak bandpass images could be a combination of increased density and temperature. These fluctuations are then mostly washed out for the 10 bar plasma presumably due to many collisions, although some gross structure remains. These results indicate that we have observed a transition from tunneling dominated plasma at low pressure to cascade plasma at high pressure in hydrogen gas. The cascade process nearly saturates the electron density within the first $\sim$100fs at 10 bar, and longer pulse widths appear to heat the electrons.

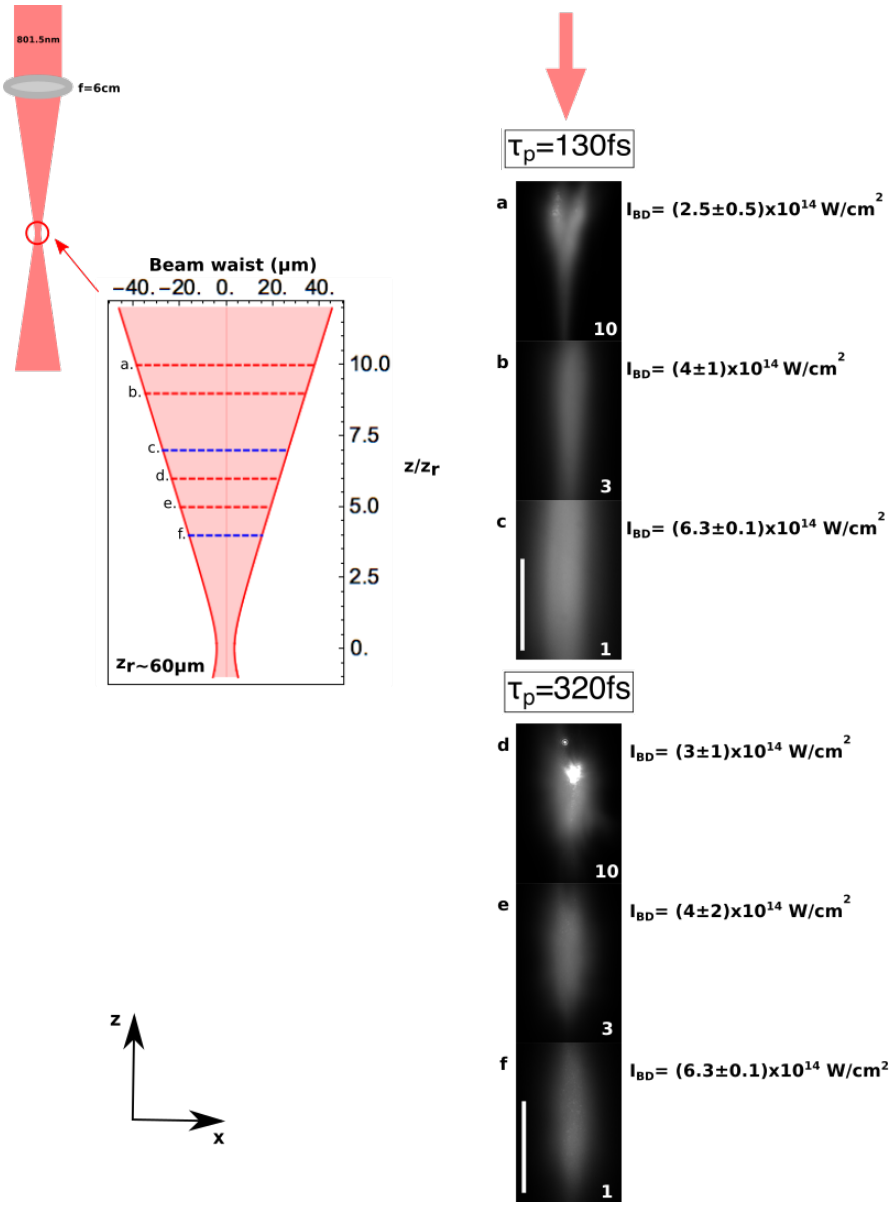

Figure 8.7: The peak intensity of the laser (W/cm^2) is determined at the location of the gas breakdown, I_{BD}, for breakdown generated in 1, 3 and 10 bar hydrogen. a)-c) shows TCCD images of breakdown generated via 130fs pulses and d)-f) shows TCCD images of breakdown via 320fs pulses. The images show the total light from a single breakdown. I_{BD} is reported to the right of each plasma. The white bar represents $100\mu m$. The red arrow indicates the direction of the laser with respect to the CCD images. The location of the breakdown within the focal path of the laser is shown in the diagram on the left. c) and f) are the 1 bar breakdowns used to calibrate the focal point.

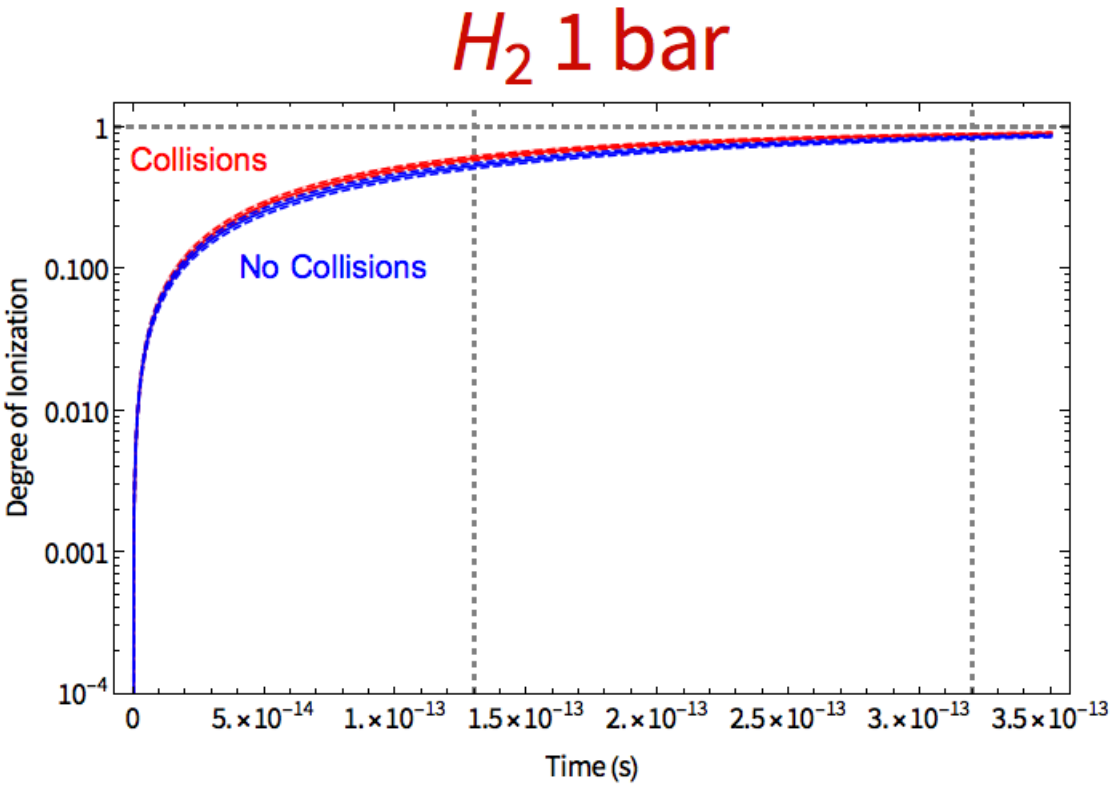

Figure 8.8: Degree of ionization vs time with and without collisions for 1 bar laser-breakdown experiment. Gridlines at 130fs and 320fs indicate the two pulse widths.

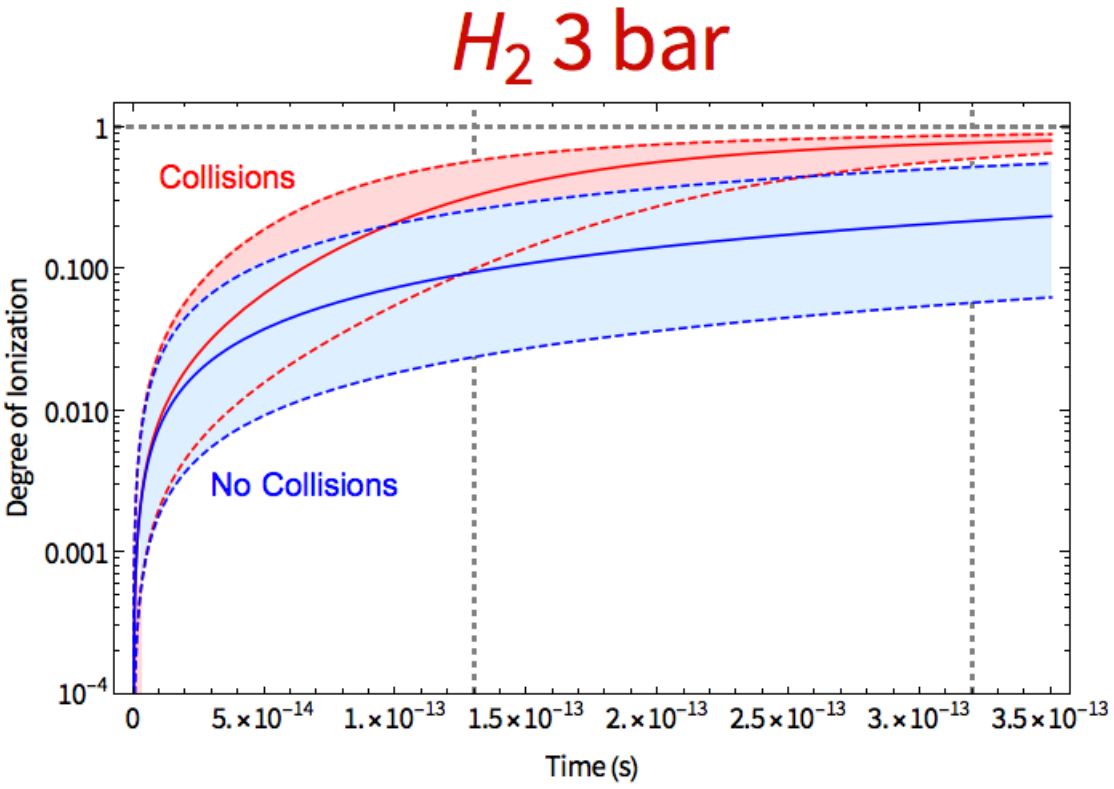

Figure 8.9: Degree of ionization vs time with and without collisions for 3 bar laser-breakdown experiment. Gridlines at 130fs and 320fs indicate the two pulse widths.

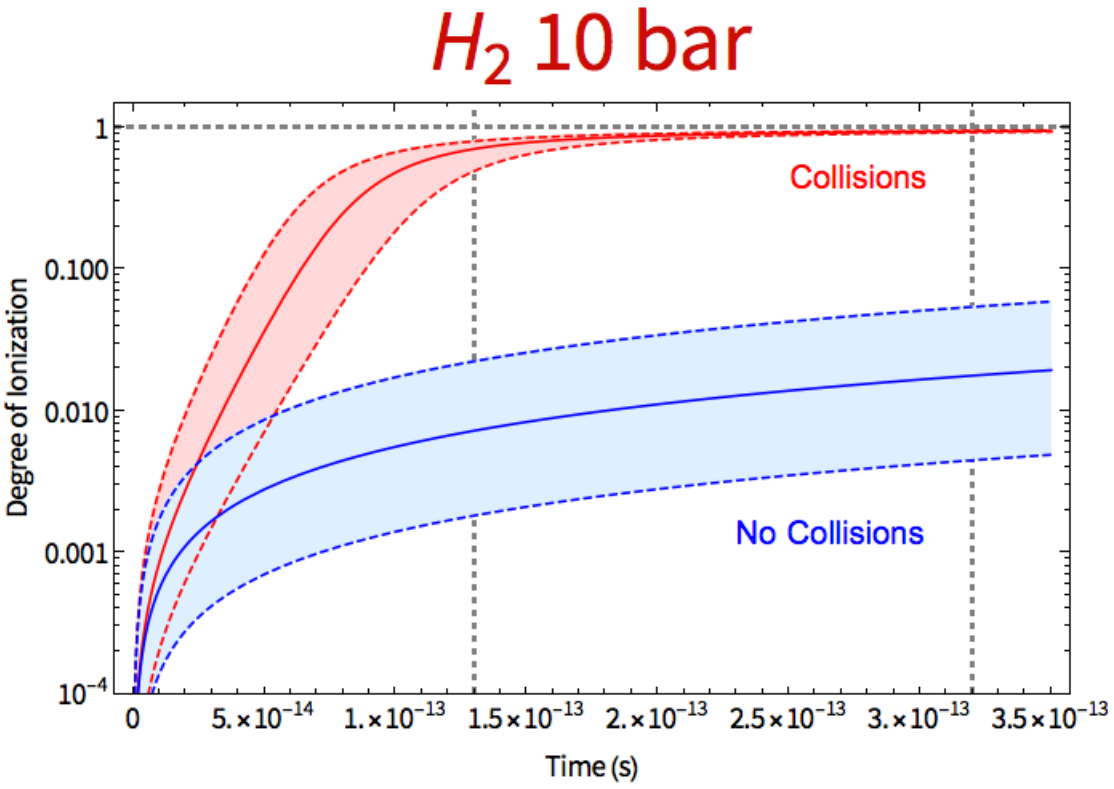

Figure 8.10: Degree of ionization vs time with and without collisions for 10 bar laser-breakdown experiment. Gridlines at 130fs and 320fs indicate the two pulse widths.

CHAPTER 9

Conclusions

The intuition from CCD and bandpass-filtered streak images in Chapter 7 (Fig. 7.2, 7.6, and 7.7) was supported by the analysis of Chapter 8. The plasma generated on longer timescales (320fs) exhibits structure due to the role of collisions in the ionization process. The plasma acquired on the shortest timescales (130fs) is essentially structureless. This fact makes the latter an ideal starting point for studies of dense and strongly coupled plasma hydrodynamics.

9.1 Role of Self-Focusing

At the highest pressure (10 bar) we expect the plasma generated via 130fs and 320fs to both have significant contributions from collisions. We measure the collision time to be ∼12fs. However, the 130fs plasma does not exhibit any of the gross structure we observe at 10 bar, 320fs. This discrepancy could be due to nonlinear pulse propagation at 130fs.

If you recall Table 8.3, we calculate the maximum ionization rate from the supercontinuum shift. At 1 bar the rates are nearly identical, but the 130fs rates overtake 320fs as the pressure is increased. This could be due to self-focusing of the laser at 130fs which leads to higher breakdown electric fields. The critical power for self focusing is given by [43]:

$$P_{cr} = \alpha \frac{\lambda^2}{4\pi n_0 n_2} \tag{9.1}$$

where α is a numerically derived constant which depends on the spatial profile of the beam. For Gaussian beams $\alpha \approx 1.8962$. The nonlinear index is measured by [44] for 1 bar hydrogen gas at 800nm to be $n_2 = 1.11 \times 10^{-23} m^2/W$. The linear index is $n_0 \approx 1$. This gives a

critical power of $P_{cr} = 9GW$. The 130fs laser pulse is at a power of $P_{130fs} \approx 6GW$ and the 320fs is pulse $P_{320fs} \approx 2.5GW$. Higher values of n_2 at 3 and 10 bar could push the 130fs above the threshold for self focusing. Because the tunneling rate is exponentially sensitive to the field while the cascade rate is essentially linear in the field, even a small amount of self focusing could significantly increase the role of tunneling at short pulse widths. This could explain the large spectral shifts we observe at high pressure for short pulses. The odd structure of 10 bar, 130fs seems to support the claim for self-focusing (see Fig. 8.7).

9.2 Non-ionizing Sources of Self-Phase Modulation

Recall the total change in the frequency or self-phase modulation of the laser:

$$\frac{\Delta\omega}{\omega_0} = -\frac{1}{c}\int_0^L \frac{\partial n(t,z)}{\partial t} dz \tag{9.2}$$

The index of refraction becomes nonlinear (as we derived in Chapter 3) in strong electric fields and can be written:

$$n(t,z) = n_0 + n_2 I(t,z) \tag{9.3}$$

where $I(t,z)$ is the intensity of the electric field. The nonlinear index n_2 has contributions from the both neutral gas (over the length of the gas L_g) and the electrons and ions in the plasma (over the length of the plasma L_p) as detailed by Woods et. al [20]. The nonlinear contribution to SPM broadening can be written:

$$\frac{\Delta\omega}{\omega_0} = -\frac{1}{c} n_2 \, L_{total} \, \frac{\partial I}{\partial t} = -\frac{1}{c}[n_2^{neutral} L_g + n_2^{plasma} L_p] \, \frac{\partial I}{\partial t} \tag{9.4}$$

Evidently this contribution is symmetric– as the leading edge and trailing edge of the intensity profile will red and then blue shift the spectrum, respectively. However, we observe only a blue shift. There are some effects such as self-steepening which would lead the shift to be antisymmetric, however a red shift would still be present. We can compare the relative contributions to the frequency shift at 1 bar. For the gas, the shift is on the order

$$(\frac{\Delta\omega}{\omega_0})_g \sim n_2^{neutral} \frac{I_{BD}}{\tau_p} L_g \tag{9.5}$$

and for the plasma the shift

$$(\frac{\Delta\omega}{\omega_0})_p \sim \frac{\rho_{n_0}}{\rho_{cr}\tau_p} L_p \tag{9.6}$$

the ratio of the effects is given by

$$\frac{\rho_{cr}}{\rho_{n_0}} n_2^{neutral} I_{BD} (\frac{L_g}{L_p}) \approx 10 \times 10^{-23} (\frac{m^2}{W})\, 10^{18} (\frac{W}{m^2}) 10^3 = 10^{-1} \tag{9.7}$$

so the effect due to the nonlinear index and neutral gas is about 10× less than that of plasma creation. We therefore conclude that the source of SPM observed is indeed ionization of the gas. Woods et. al also concluded this [20, 19] and they are in a similar experimental setup to this thesis.

9.3 Other Side of the Chirp

Recall in Chapter 4, the process of broadening the pulse width of the laser was discussed. This is called chirping the pulse and is done by delaying a portion of the light that makes up the short pulse. An ultra-short pulse must have a large bandwidth; for the Solstice Ace it is around 40nm. Fig. 9.1 shows the transmitted laser spectrum for a 360fs pulse after being focused through 10 bar hydrogen. The pulse is chirped to 360fs but in the opposite direction from the data shown in Chapter 8! This means that if in the previous chapter the laser pulse had the redder light leading the bluer light, this pulse now has the bluer light leading the redder light. We do not know the direction of the chirp.

Compare the spectral shift in Fig. 9.1 to the spectral shift seen for 10 bar in Fig. 8.3. In Fig. 8.3 it looks as though the plasma shifts the bluer part of the light, resulting in a shoulder appearing in the spectrum. Here in Fig. 9.1 the plasma must now be shifting the redder part of the spectrum. This is because the laser frequency is shifted at a certain time in the pulse– tunneling is argued to occur early on in the pulse while cascade occurs throughout– and so depending on the direction of the chirp, the shift will take place at a different λ_0. The light in Fig. 9.1 is blue shifted but does not result in a shoulder because it is still within the bandwidth of the pulse.

This story becomes clear looking at Fig. 9.2, which shows the emergence of the broad blue

shoulder we expect as the pulse width is shortened (same chirp as Fig. 9.1). If a measurement were conducted to determine the direction of the chirp, more information about the breakdown process (i.e., when it occurs during the pulse) could be learned. This might be a nice measurement for the next researcher. In the next section, additional future work building on this thesis is proposed.

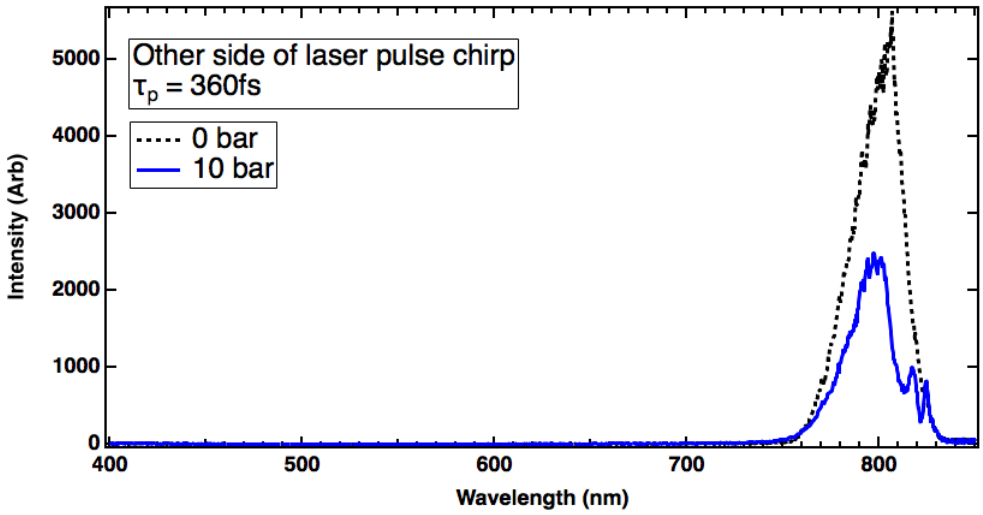

Figure 9.1: Transmitted laser spectra for 360fs pulse on the other side of the chirp.

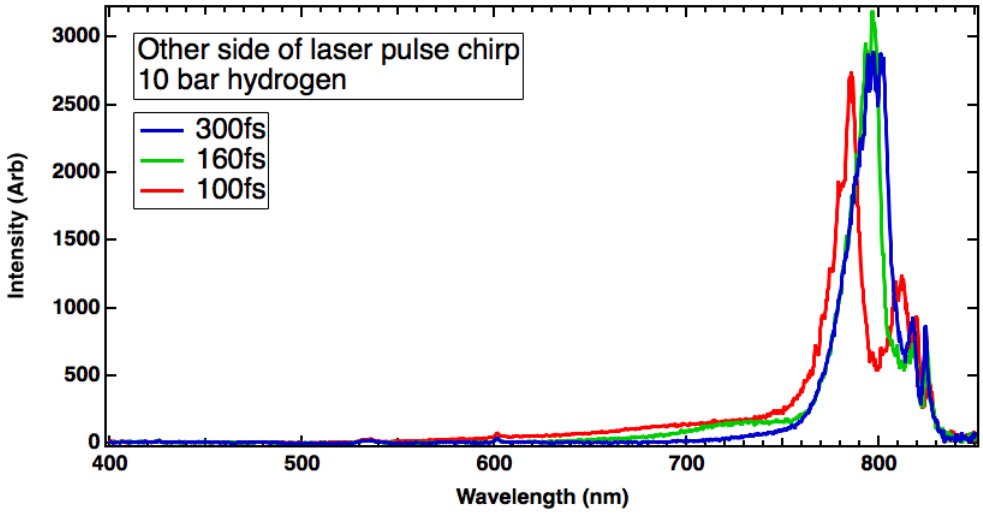

Figure 9.2: Transmitted laser spectrum as a function of pulse width on the other side of the chirp.

9.4 Future Work

9.4.1 Plasma-Induced Defocusing

The effect of plasma-induced defocusing was not taken into account in the model for the ionization rate. The electric field was assumed to be a step function turning on at t=0 and turning off at t=350fs to span the range of pulse widths in the experiment. In reality the effect of ionizing the gas modifies the index of refraction of the gas, and this not only contributes to SPM but can defocus the laser light. This leads to a modified electric field at the breakdown spot. The total index of refraction can be written:

$$n(t,z) \approx 1 + n_2 I(t,z) - \frac{\rho_e(t,z)}{2\rho_{cr}} \tag{9.8}$$

The next iteration of analysis for this experiment could couple the electron density as a function of time back to the electric field by developing a model for plasma-induced defocusing in our setup. There are researchers at UCLA who simulate high intensity light-matter interactions and would have experience in this. Additionally combined with the effect of self-focusing, which is included through the n_2 term in the index, one might reproduce the full range of plasma observed in this experiment. With this type of model developed and validated, one could use it to predict future experiments and help guide research.

9.4.2 Energy Transport in Dense Plasma

Bandpass streak images taken along the z-axis of the 3 bar, 320fs plasma are shown in Fig. 9.3. Lineouts are taken from the emission as a function of time, and these show the plasma emission either expanding or "melting." This difference could be due to the effect of cooling via adiabatic expansion (plasma expands) or conduction to the surrounding gas (plasma "melts"). Understanding how this energy transport works could help identify the equation of state for dense plasmas, namely: 1) how much does this differ from an ideal gas? and 2) how does this change as the plasma coupling parameter is modified?

New capabilities for studying femtosecond laser generated plasma in the Putterman Lab at

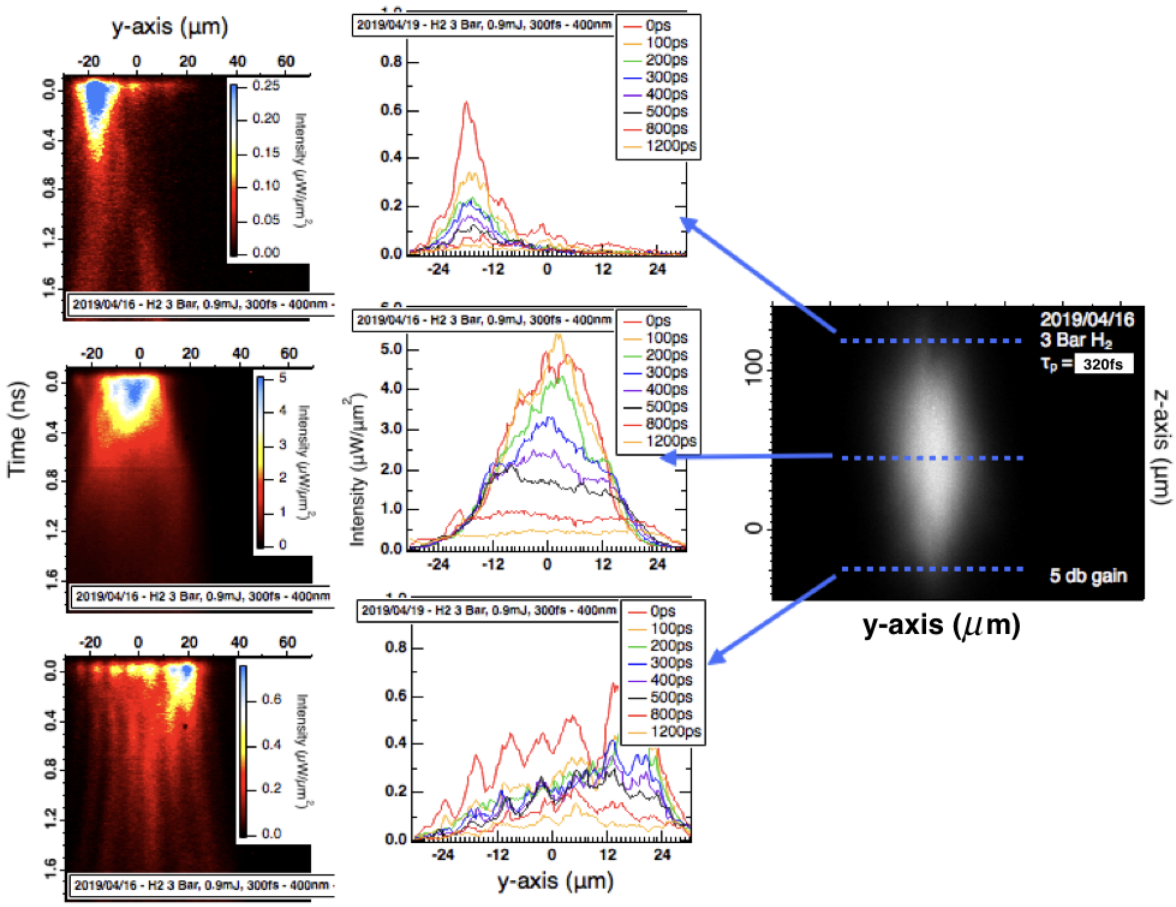

Figure 9.3: Streak images taken with the 400nm bandpass filter at the top, middle, and end of the 3 bar breakdown are on the left. Lineouts from these images from t=0 to t=1.2ns are displayed in the middle. A CCD image taken with the TCCD camera is shown on the right and indicates the approximate location of the streak images.

UCLA are shown in Fig. 9.4. First, there is a second and third harmonic generation crystal module by Spectra-Physics which can be integrated into the Solstice Ace setup. This can double the frequency of light to produce a wavelength of 400nm, or triple it to produce 200nm light! Additional pulse energy that is needed for this process could be gained by switching the dielectric beam splitter shown in Fig. 5.2. The optical mount for this piece is back loaded in anticipation of switching this component out. The silver mirrors in the optical setup might be good down to 400nm, however UV optimized mirrors would probably need to be used for the 200nm light.

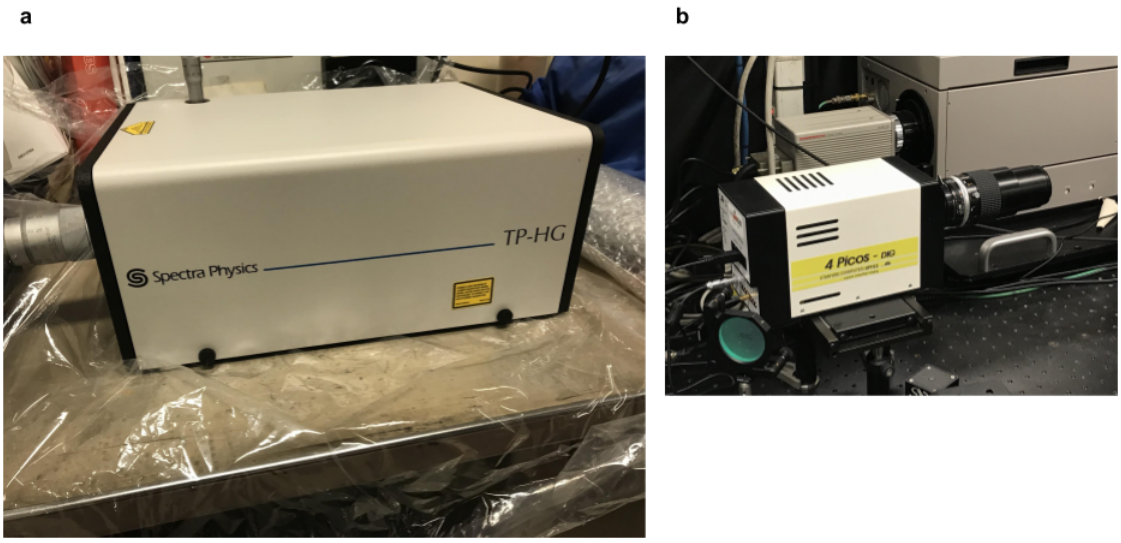

Figure 9.4: a) Second and third harmonic generation module by Spectra-Physics designed to work with the Solstice Ace laser. b) 200ps-gated ICCD camera by Stanford Computer Optics which has a large square array of pixels and can be used to image the entire plasma.

9.5 Future of Dense Plasma Hydrodynamics

The laser-breakdown process in a dense gas system has been explored as a function of pressure and laser pulse width. The experiment set up now at UCLA is well controlled and equipped to move forward. The goal of probing plasma hydrodynamics for a range of coupling strengths is possible. The neutral density can be spanned via gas pressure up to 70 bar in the current high pressure chamber. The energy input time – that being the laser pulse width – has been shown to influence the final electron temperature and density especially at high pressure. The big hope is to produce a system with long-lived cold ions that could develop strong correlations. A good candidate is high pressure xenon gas (∼50 bar). Xenon has many charge levels that can be ionized via laser-breakdown [6] and the high pressure of the neutral density may establish pre-order for the system of ions [10]. Doubling or even tripling the frequency of laser light could help in coupling the laser into

such a dense plasma. Multiphoton ionization may start to contribute significantly to ionization. The results of this thesis will help elucidate whatever breakdown behavior is observed in the next experiment. A symmetric and structureless plasma, such as 3 bar hydrogen breakdown generated with a 130fs pulse, provides a perfect baseline to compare with in the search for effects due to strong coupling.

Bibliography

[1] Brad M.S. Hansen and James Liebert. Cool white dwarfs. *Annual Review of Astronomy and Astrophysics*, 41(1):465–515, 2003.

[2] H. Thomas, G. E. Morfill, V. Demmel, J. Goree, B. Feuerbacher, and D. Möhlmann. Plasma crystal: Coulomb crystallization in a dusty plasma. *Phys. Rev. Lett.*, 73:652–655, Aug 1994.

[3] Thomas C. Killian. Ultracold neutral plasmas. *Science*, 316(5825):705–708, 2007.

[4] John D. Lindl, Peter Amendt, Richard L. Berger, S. Gail Glendinning, Siegfried H. Glenzer, Steven W. Haan, Robert L. Kauffman, Otto L. Landen, and Laurence J. Suter. The physics basis for ignition using indirect-drive targets on the national ignition facility. *Physics of Plasmas*, 11(2):339–491, 2004.

[5] A. Bataller, B. Kappus, C. Camara, and S. Putterman. Collision time measurements in a sonoluminescing microplasma with a large plasma parameter. *Phys. Rev. Lett.*, 113:024301, Jul 2014.

[6] A. Bataller, G. R. Plateau, B. Kappus, and S. Putterman. Blackbody emission from laser breakdown in high-pressure gases. *Phys. Rev. Lett.*, 113:075001, Aug 2014.

[7] Alexander Bataller, Alexandra Latshaw, John Koulakis, and Seth Putterman. Dynamics of strongly coupled two-component plasma via ultrafast spectroscopy. *Optics Letters*.

[8] A. Diaw and M. S. Murillo. Generalized hydrodynamics model for strongly coupled plasmas. *Phys. Rev. E*, 92:013107, Jul 2015.

[9] Nathaniel R. Shaffer, Sanat Kumar Tiwari, and Scott D. Baalrud. Pair correlation functions of strongly coupled two-temperature plasma. *Physics of Plasmas*, 24(9):092703, 2017.

[10] Gautham Dharuman, Liam G Stanton, and Michael S Murillo. Controllable non-ideal plasmas from photoionized compressed gases. *New Journal of Physics*, 20(10):103010, oct 2018.

[11] S. G. Brush, H. L. Sahlin, and E. Teller. Monte carlo study of a one-component plasma. i. *The Journal of Chemical Physics*, 45(6):2102–2118, 1966.

[12] G. E. Morfill, H. M. Thomas, U. Konopka, and M. Zuzic. The plasma condensation: Liquid and crystalline plasmas. *Physics of Plasmas*, 6(5):1769–1780, 1999.

[13] A. Bataller, J. Koulakis, S. Pree, and S. Putterman. Nanosecond high-power dense microplasma switch for visible light. *Applied Physics Letters*, 105(22):223501, 2014.

[14] R. G. Meyerand and A. F. Haught. Gas breakdown at optical frequencies. *Phys. Rev. Lett.*, 11:401–403, Nov 1963.

[15] D. Du, X. Liu, G. Korn, J. Squier, and G. Mourou. Laser-induced breakdown by impact ionization in sio2 with pulse widths from 7 ns to 150 fs. *Applied Physics Letters*, 64(23):3071–3073, 1994.

[16] X. Liu, D. Du, and G. Mourou. Laser ablation and micromachining with ultrashort laser pulses. *IEEE Journal of Quantum Electronics*, 33(10):1706–1716, Oct 1997.

[17] A. Vogel, J. Noack, K. Nahen, D. Theisen, R. Birngruber, D. X. Hammer, G. D. Noojin, and B. A. Rockwell. Laser-induced breakdown in the eye at pulse durations from 80 ns to 100 fs. 3255, 1998.

[18] P.P Pronko, S.K Dutta, J Squier, J.V Rudd, D Du, and G Mourou. Machining of sub-micron holes using a femtosecond laser at 800 nm. *Optics Communications*, 114(1):106 – 110, 1995.

[19] Wm. M. Wood, C. W. Siders, and M. C. Downer. Measurement of femtosecond ionization dynamics of atmospheric density gases by spectral blueshifting. *Phys. Rev. Lett.*, 67:3523–3526, Dec 1991.

[20] W. M. Wood, C. W. Siders, and M. C. Downer. Femtosecond growth dynamics of an underdense ionization front measured by spectral blueshifting. *IEEE Transactions on Plasma Science*, 21(1):20–33, Feb 1993.

[21] A. Braun, G. Korn, X. Liu, D. Du, J. Squier, and G. Mourou. Self-channeling of high-peak-power femtosecond laser pulses in air. *Opt. Lett.*, 20(1):73–75, Jan 1995.

[22] H. Yang, J. Zhang, W. Yu, Y. J. Li, and Z. Y. Wei. Long plasma channels generated by femtosecond laser pulses. *Phys. Rev. E*, 65:016406, Dec 2001.

[23] P. K. Kennedy. A first-order model for computation of laser-induced breakdown thresholds in ocular and aqueous media. i. theory. *IEEE Journal of Quantum Electronics*, 31(12):2241–2249, Dec 1995.

[24] L. V. Keldysh. Ionization in the field of a strong electromagnetic wave. *Sov. Phys. JETP*, 20(5):1307–1314, 5 1965.

[25] S. Augst, D. D. Meyerhofer, D. Strickland, and S. L. Chin. Laser ionization of noble gases by coulomb-barrier suppression. *J. Opt. Soc. Am. B*, 8(4):858–867, Apr 1991.

[26] M. Thiyagarajan and J. E. Scharer. Experimental investigation of 193-nm laser breakdown in air. *IEEE Transactions on Plasma Science*, 36(5):2512–2521, Oct 2008.

[27] Setsuo Ichimaru. *Basic Principles of Plasma Physics*. W. A. Benjamin, Inc., Reading, Massachusetts, 1973.

[28] Jianwei Miao. Physics 210 electromagnetism series lecture notes. 2012.

[29] John David Jackson. *Classical Electrodynamics*. John Wiley & Sons, Inc., 2 edition, 1975.

[30] T.P. Hughes. *Plasma and Laser Light*. John Wiley & Sons, Inc., 1975.

[31] Donna Strickland and Gerard Mourou. Compression of amplified chirped optical pulses. *Optics Communications*, 55(6):447 – 449, 1985.

[32] P. Maine, D. Strickland, P. Bado, M. Pessot, and G. Mourou. Generation of ultrahigh peak power pulses by chirped pulse amplification. *IEEE Journal of Quantum Electronics*, 24(2):398–403, Feb 1988.

[33] Anthony E. Siegman. *Lasers*. University Science Books, 1986.

[34] Spectra-Physics/Newport Corporation, 3635 Peterson Way Santa Clara, CA 95054. *Solstice Ace User's Manual*, March 2017.

[35] M Raghu Ramaiah, Avnish Sharma, Prasad Naik, P. Gupta, and Rashid Ganeev. A second-order autocorrelator for single-shot measurement of femtosecond laser pulse durations. *Sadhana*, 26:603–611, 12 2001.

[36] S.C. Rae. Ionization-induced defocusing of intense laser pulses in high-pressure gases. *Optics Communications*, 97(1):25 – 28, 1993.

[37] Alexander Bataller. Isotope experiment. 2015.

[38] Newport Corporation, Stratford, CT. *Report of Calibration of One Standard of Spectral Irradiance (250-2400nm)*, 9 2013.

[39] J. R. Oppenheimer. Three notes on the quantum theory of aperiodic effects. *Phys. Rev.*, 31:66–81, Jan 1928.

[40] Y. R. Shen. *The Principles of Nonlinear Optics*. John Wiley & Sons, Inc., 2003.

[41] A. G. Engelhardt and A. V. Phelps. Elastic and inelastic collision cross sections in hydrogen and deuterium from transport coefficients. *Phys. Rev.*, 131:2115–2128, Sep 1963.

[42] S. C. Rae and K. Burnett. Possible production of cold plasmas through optical-field-induced ionization. *Phys. Rev. A*, 46:2077–2083, Aug 1992.

[43] M. J. Soileau, William E. Williams, Nastaran Mansour, and Eric W. Van Stryland. Laser-Induced Damage And The Role Of Self-Focusing. *Optical Engineering*, 28(10):1133 – 1144, 1989.

[44] E. T. J. Nibbering, G. Grillon, M. A. Franco, B. S. Prade, and A. Mysyrowicz. Determination of the inertial contribution to the nonlinear refractive index of air, n2, and o2 by use of unfocused high-intensity femtosecond laser pulses. *J. Opt. Soc. Am. B*, 14(3):650–660, Mar 1997.